

UNIVERSITY OF ONTARIO INSTITUTE OF  
TECHNOLOGY

Effect of iron content on  
electrodeposited Fe-MnO<sub>x</sub>  
catalysts for water oxidation

by  
Elizabeth Selinger

A thesis submitted in partial fulfillment  
of the requirements for the degree of

Master of Science  
in  
Materials Science  
in the Faculty of Science

Supervisor: Dr. Isaac Tamblyn

April 2018

© Elizabeth Selinger 2018



# Abstract

Effect of iron content on electrodeposited Fe-MnO<sub>x</sub> catalysts for water oxidation

by Elizabeth Selinger

Faculty of Science (Materials Science)

University of Ontario Institute of Technology

2018

MnO<sub>x</sub> materials are earth-abundant and known to be efficient catalysts for the water oxidation reaction (WOR). I present the exploration of an optimal method of cathodically electrodepositing MnO<sub>x</sub> catalysts on an FTO substrate, allowing for quick synthesis and a homogeneous coverage of the substrate. I then study WOR activity of the MnO<sub>x</sub> catalyst with varying amounts of Fe in the structure. The catalyst structure was probed using XPS for elemental analysis, FESEM to study the morphology, and a Kelvin probe for exploration of the work function, and observations are discussed.

# Acknowledgements

First, I must present my profound thanks to my supervisor, Dr. Isaac Tamblyn. I am immensely grateful for your expertise and guidance throughout these last two years. Your advice, insight, and encouragement (especially of new opportunities) have been truly invaluable to me.

I am also exceedingly grateful to Dr. Marco Armandi, Dr. Barbara Bonelli, and Marco Etzi from Politecnico di Torino. I am incredibly thankful for the opportunity you gave me to do research at PdT, for your patience with my learning of the experimental process, and for your insightful collaboration on this project. Working with you was a tremendously rewarding experience.

Also, sincere thanks to Dr. Gregory Lopinski at the National Research Council. I really appreciate you taking the time to collaborate on this experiment, and for going beyond that to teach me to use the Kelvin probe and allowing me the use of your lab. As well, thanks to Dr. Brad Easton for your helpful discussion on these experiments, your guidance in electrochemistry concepts, and for the use of your lab and equipment.

Thank you to Dr. Su Ying Quek and Dr. Yifeng Chen at the National University of Singapore for welcoming my participation in your research group, and giving me expertise and guidance on electronic structure investigations.

I would also like to extend my gratitude to my supervisory committee, Dr. Andrew Vreugdenhil and Dr. Franco Gaspari. Thank you for your helpful observations and guidance over my thesis process. Thank you also to Dr. Olena Zenkina for agreeing to be the external examiner for this thesis.

My heartfelt thanks goes to the past and present members of CLEAN, especially Kyle Mills and Amber Maharaj. I truly appreciate having shared this experience together. Thank you to everyone in the lab for answering my technical questions, exploring topics with me, and staying in touch during my travels. Also, a special thanks to Kevin Ryczko for your collaboration on the computational aspect of the project.

Thank you to my parents, sisters, aunts, uncles, grandparents, and soon-to-be mother-, father-, and brothers-in-law. Your unwavering support has not gone unnoticed, and I am so grateful to be encircled by such encouragement in my life.

Finally I extend a unique and humble thanks to my fiancé Will. I am truly grateful for your tokens of support, large or small, symbolic or material. You have been an exceptional source of strength and motivation for me.

# Contents

<b>Certificate of approval</b>	ii
<b>Abstract</b>	iii
<b>Acknowledgements</b>	iv
<b>Contents</b>	vi
<b>Physical constants</b>	ix
<b>Abbreviations</b>	x
<b>Symbols</b>	xi
<b>1 Introduction</b>	1
1.1 Motivation	1
1.1.1 Renewable energy and water splitting	1
1.1.2 Electrocatalytic water splitting	4
1.1.3 Transition metal oxide catalysts	5
1.2 Literature review	6
1.3 Thesis outcomes	13
<b>2 Background</b>	14
2.1 Electrochemistry	14
2.1.1 Cyclic voltammetry	16
2.1.2 Chronoamperometry	18
2.1.3 Tafel plots	20
2.1.4 Electrodeposition	25
2.1.5 Water oxidation reaction	26

2.2 Electronic structure	28
2.2.1 Molecular orbital theory	30
2.2.2 Band structure	33
2.2.3 Work function	34
2.3 Instrumentation	35
2.3.1 Potentiostat	36
2.3.2 XPS	37
2.3.3 FESEM	39
2.3.4 Kelvin Probe	40
<b>3 Methods</b>	<b>44</b>
3.1 Sample synthesis	45
3.1.1 Glass cleaning & preparation	45
3.1.2 Electrodeposition of MnO <sub>x</sub>	46
3.1.3 Heat treatment	48
3.2 Activity testing	48
3.2.1 Electrochemical tests	48
3.2.2 Electrochemical analysis	49
3.3 Structural characterization	50
<b>4 Results and discussion</b>	<b>52</b>
4.1 Electrochemical results	52
4.1.1 Electrocatalyst synthesis protocol	53
4.1.1.1 Constant potential vs. constant current depositions	53
4.1.1.2 Deposition time	55
4.1.1.3 Concentration regimes	58
4.1.1.4 High concentration, long time depositions	61
4.1.1.5 Size of deposition area	62
4.1.1.6 Heat treatment	63
4.1.2 Adding metals to deposition solution	65
4.1.2.1 Calcium	66
4.1.2.2 Ruthenium	67
4.1.2.3 Iron	67
4.1.3 Discussion of electrochemical results	70
4.2 Structural/elemental characterization	73
4.2.1 FESEM	74
4.2.1.1 Feature analysis	77

4.2.2 XPS	80
4.2.3 Discussion of structural/characterization results	82
4.3 Work function results	84
4.3.1 Surface measurements	84
4.3.2 Average work function of the material	86
4.3.3 Discussion of work function results	87
<b>5 Conclusions and future perspectives</b>	<b>89</b>
<b>6 Appendix A</b>	<b>92</b>
6.1 Preliminary computational results	92
6.2 Density Functional Theory	92
6.3 DFT calculations	95
6.3.1 Computational calculation of work function	95
<b>7 Appendix B</b>	<b>97</b>
7.1 HR XPS scans of Fe	97
<b>8 Bibliography</b>	<b>98</b>

# Physical Constants

Faraday constant  $9.648\ 533\ 289 \times 10^4\ \text{C mol}^{-1}$

Ideal gas constant  $8.314\ 4598\ \text{J K}^{-1}\ \text{mol}^{-1}$

# Abbreviations

<b>CA</b>	chronoamperometry
<b>CC</b>	constant current
<b>CP</b>	constant potential
<b>CV</b>	cyclic voltammetry
<b>DFT</b>	density functional theory
<b>FESEM</b>	field emission scanning electron microscopy
<b>FTO</b>	fluroide-doped tin oxide
<b>HER</b>	hydrogen evolution reaction
<b>HRR</b>	hydrogen reduction reaction
<b>OER</b>	oxygen evolution reaction
<b>RDS</b>	rate determining step
<b>WOR</b>	water oxidation reaction
<b>XPS</b>	x-ray photoelectron spectroscopy

# Symbols

symbol		units
$E$	applied potential	V
$E_0$	standard reduction potential	V
$i$	current	A m <sup>-2</sup>
$i_0$	exchange current	A m <sup>-2</sup>
$j$	current density	A
$j_0$	exchange current density	A
$k$	reaction rate constant	mol <sup>1-(m+n)</sup> L <sup>(m+n)</sup> s <sup>-1</sup>
$n$	number of electrons	-
$T$	temperature	K
$\alpha$	charge transfer coefficient	-
$\eta$	overpotential	V



# 1 Introduction

## 1.1 Motivation

In this first section, I present the motivation for my thesis experiments. First I outline a broad motivation for renewable energy research and water splitting for renewable fuels. Next I present the method of electrolysis with a suitable catalyst for efficient water splitting. Finally I will motivate the use of transition metal oxides, and Mn oxides in particular, as promising catalyst materials for this reaction.

### 1.1.1 Renewable energy and water splitting

The modern world has large energy needs that are growing rapidly as more and more countries develop industrially. Our dependence on carbon-based energy sources is unideal; the earth is warming at an unprecedented rate in our knowledge of the history of

the planet.[1] This warming has alarming effects, such as extreme weather conditions of flooding and droughts in highly populated areas of the planet. Further warming will reach a critical point of threatening human existence on the planet in as soon as the next 100 years.[2]

Active fields of research exist to explore the mitigation of CO<sub>2</sub> going into the atmosphere, as in CO<sub>2</sub> sequestration.[3] However, even if capturing future CO<sub>2</sub> emissions becomes financially viable, the ideal situation is to draw energy from sustainable renewable sources that do not emit greenhouse gases. This is why renewable energy is a major area of research, from the mechanism of the processes necessary to gather and convert the energy, to the industrial implementation of wide-scale use of these renewables.

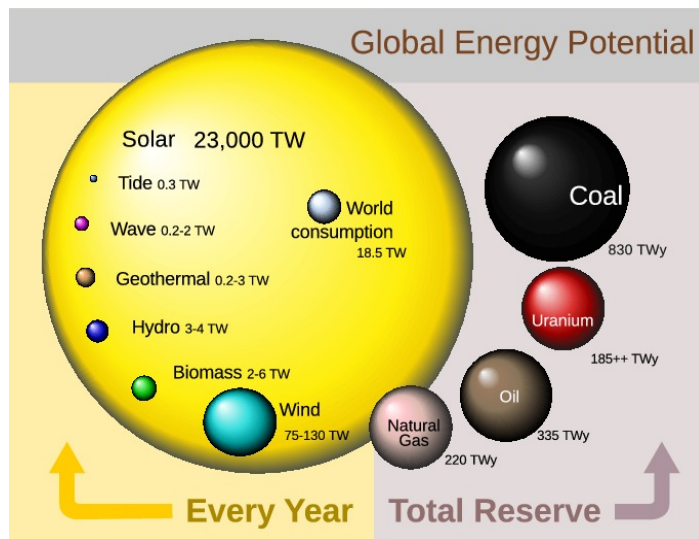


**Figure 1** Global energy potential from different resources (2015), showing per year contribution for renewables and total reserve for non-renewables.[4]

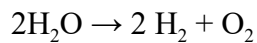
Attempting to use the sun as our main energy source is an intuitive option because it provides a gigantic amount of energy to the earth through infrared and visible light radiation. The sun is always providing the earth with energy, whether or not we harness it. In Fig. 1 it is clear that the global energy potential from solar energy is a colossal

resource (note that the representations are meant to be spheres, not circles, and therefore the relative values are on a volumetric scale).

Advancements in the field of photovoltaics and their steady implementation have made a much higher energy reliance on solar power possible. In the 2014 EPA Technology Roadmap on Solar Photovoltaic Energy[5] they found that photovoltaic systems prices have been reduced to one-third of their cost from six years previous. It is envisioned that 16% of electricity used globally would be provided by photovoltaics by 2050. Since we now have the means to power most of our technology through electricity, including transportation, we can look to photovoltaics as a viable option to replace fossil fuels in most of our energy needs.

However the intermittent nature of solar energy is still an issue that needs to be addressed. There is not always enough of the sun's radiation reaching a photovoltaic panel, and so electricity is only provided intermittently. It is difficult to integrate an arbitrarily intermittent power source such as this into a grid that requires stability for our energy needs in the home and in industry. An attractive solution is to store the sun's energy to be used during non-peak sunlight hours. There are many different methods of energy storage. Some examples are to convert the electricity from photovoltaics into heat to be stored as steam, or use it to do work to pump water to higher ground and then be released to run turbines.

One approach is the storage of energy in molecular bonds, thereby producing a fuel. This requires electricity to drive a reaction, causing atoms to bond and creating molecules with high energy density. This would be stored as a fuel to then be converted back to electricity or heat. Specifically, this can happen through water splitting or the separation of H<sub>2</sub>O into constituent H<sub>2</sub> and O<sub>2</sub>, as shown below in Eq. 1.



1

This process is a redox reaction, involving two half-reactions - one is the water oxidation reaction (WOR), also called the oxygen evolution reaction (OER), outlined in

Eq. 2. The other is the hydrogen evolution reaction (HER), also called the hydrogen reduction reaction (HRR), seen in Eq. 3

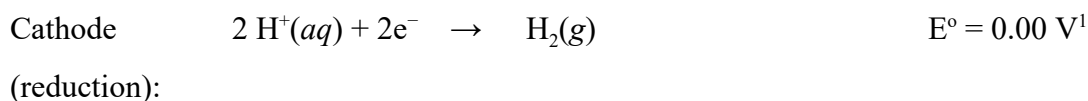
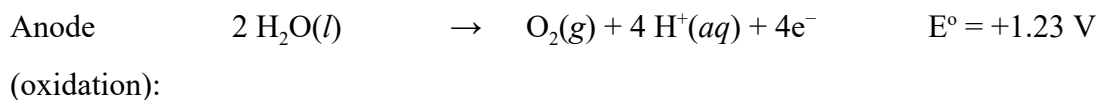


The idea of storing and transferring energy in H<sub>2</sub> dates back to calculations done by Lawaczek in the 1930s. J. O'M. Bockris was one of the first staunch advocates for a "Hydrogen Economy", writing about its advantages as a medium of energy and in elimination of pollution and greenhouse gas emissions[6]. Since Lawaczek's work, there has continuously been research surrounding the splitting of water.

Sea water being a practically unlimited resource, a search for an efficient means to produce H<sub>2</sub> through water is a promising avenue of exploration for renewable fuel storage.

### 1.1.2 Electrocatalytic water splitting

Since water splitting involves non-spontaneous redox reactions it can be achieved through electrolysis, where the half-reaction overpotentials can be seen below.




---

<sup>1</sup> These are the potential values performed at pH of 0, with a subtraction of -0.059 V from each reaction, per unit pH. The difference in potential between the two reactions remains the same.

The above reaction assumes completely reversible conditions and potentials are typically greater than these values due to various factors (overvoltages attributed to activation energy, diffusion, reorganization, for example). This oxidation reaction is termed the water oxidation reaction (WOR) while the reduction half of the reaction is called the hydrogen reduction reaction (HRR). WOR requires the movement of four electrons (coupled with protons) while HRR sees the transfer of two electrons in the reaction; thus the energy required to drive WOR is much higher than for HRR.

Because of the high applied potential needed for WOR to take place, water splitting is considered inefficient for wide-scale production of a hydrogen fuel. This makes WOR an ideal reaction to apply the study of electrocatalysts to reduce the overpotential, for an overall more energy-efficient water splitting process. WOR can be facilitated by a catalyst, such as a molecule or complex with a highly positive oxidation state, that readily transfers electrons from water to itself and then can easily transition back to an oxidized state, so electrons can move to complete the redox reaction.

### 1.1.3 Transition metal oxide catalysts

In this field, successful WOR electrocatalysts (henceforth referred to as WOR catalysts or just catalysts) have been discovered such as RuO<sub>2</sub> and IrO<sub>2</sub>, however in recent years focus has shifted to the study of earth-abundant materials to achieve cost-effective catalysis. Many aspects of a catalyst must be considered to assess its overall efficiency, including reproducibility, long-term stability, and cost associated with method of synthesis, abundance, and scalability.

Transition metals, classified by their incomplete d sub-shells, allow for many oxidation states. This is what makes them ideal for water oxidation catalysis, their availability of oxidation states allows for the transfer of electrons necessary, since WOR requires the transfer of 4 electrons to produce one oxygen molecule.

Transition metal oxides are also interesting because of their surface properties. The crystal structures of transition metal oxides have been studied and are well known, but the surfaces are not as well understood. This is because when the bulk transition metal oxides are cut, the surface created will not retain its structure; it will undergo reconstruction to form the most thermodynamically stable configuration at the surface (minimizing the Gibbs energy). Thus, interesting configurations are formed at which reactions can take place.

Some metal oxides have been shown to highly catalyze WOR, such as IrO<sub>2</sub> and RuO<sub>2</sub>. However, these noble metals are not earth-abundant and therefore expensive, as well as often being classified as toxic. It is necessary to point out that this description of toxicity is more subtle than is usually presented, and to be accurately applied many factors must be considered, such as oxidation states in the material, morphology and structure, and properties of the environment. A more in-depth discussion of toxicity of catalysts is found in the literature review.

Binary compounds of manganese and oxygen are defined as manganese oxides. These can be found in many different forms because of the many stable oxidation states associated with transition metals such as manganese; manganese has the most stable oxidation states of any transition metal, making it abundant in more oxide forms than other transition metals. Manganese oxides are generally robust and earth-abundant, especially in the natural form of MnO<sub>2</sub> (pyrolusite).

In nature, the part of the plant that performs water oxidation during photosynthesis is a manganese complex. This is a motivation for research of a WOR catalyst that is in part manganese. Manganese oxides are promising because of their cheap cost and ease of synthesis.

## 1.2 Literature review

In 2017, Suen et al. reported on the mechanisms of electrocatalysis for WOR[7]. They reviewed studies of oxide and non-oxide catalysts to learn about the electronic state and structural influences on WOR activity. Overall, they conclude that high electroconductivity is key for the transfer of charge-carriers from metal electrode to adsorbed intermediates for the reaction catalysis. Metal oxides suffer low electroconductivity but they are worth pursuing because of the high number of options for improving electroconductivity[8], including nanostructuring of the material surface and doping with conductive foreign elements.

In several comprehensive reviews[7], [9]–[12], it is agreed that Ru and Ir oxides are the highest standard for metal-oxide based WOR catalysts with excellent performance for WOR, thus Ru and Ir oxides are used as the benchmark across studies of electrocatalysts for WOR. Studies of Ru oxide catalysts show the lowest overpotentials for WOR[9], [12], however the material also shows low stability. Ir-based catalysts have adequate stability, as their dissolution is much less over use and time compared to Ru-based catalysts[9]. Computational studies have shown that IrO<sub>2</sub> have superior stability to RuO<sub>2</sub> because of the stable formation of WOR reaction intermediates[13]. Although Ru and Ir-based electrocatalysts are the state-of-the-art, they are expensive noble metals, so research efforts involving these materials focus on improving their electrocatalytic properties to make them more practical for commercial use[14]. The activity of Ru and Ir-based catalysts can be improved by maximizing the number of metal atoms participating in the reaction, so nanoparticles and supports with large surface area are an active area of research in terms of noble metal catalysts for WOR.

One oft-discussed disadvantage of the use of Ru and Ir-based catalysts is the toxicity of these materials. Recently[15], Egorova and Ananikov showed that as the field of toxicology has progressed, the description of metal catalysts as toxic or non-toxic has become inaccurate in many cases, with many myths propagating these descriptions. In fact, just the measurement of toxicity of these materials can be complex, involving exposure time, concentration, nature of the environment, and more. Furthermore, toxicity must be categorized as acute (toxic within relatively short exposure) or chronic (toxic

only after prolonged exposure), a distinction not often pointed out. The values to characterize toxicity (e.g. median lethal dose or LD<sub>50</sub>) are not usually reported with WOR catalysts, with instead a presumption of toxicity based on the metal element(s) involved. However, as shown in the Egorova et al. paper[15], this basis for toxicity is unacceptable and should be instead based upon the metal *compound* (in this case metal oxides). In terms of metal oxides, the LD<sub>50</sub> value for Ru oxides and Mn oxides fall into a very similar range of 500-5000 mg kg<sup>-1</sup> (LD<sub>50</sub> of Ir oxides are unreported). Therefore I do not report on low toxicity as an advantage of Mn oxides to Ru or Ir oxide catalysts.

One point of inspiration for a less expensive catalyst is to look at water oxidation in nature. The Photosystem II complex found in plants uses a water-oxidizing catalyst in the form of a Mn<sub>4</sub>CaO<sub>x</sub> cluster[16]. It can be theorized that a synthesized electrocatalyst oxide involving Earth-abundant Mn and/or Ca could perform catalysis of WOR under a moderate pH. Transition metal oxides such as Mn oxides are favourable for the multi-electron transfer involved in WOR, because of the multiple valences available to form intermediate active sites[14]. The low cost and corrosion-resistant characteristics of transition metal oxides make them practical for commercial use. However, the morphological architecture of the material surface is extremely influential in the resulting level of activity for transition metal-based electrocatalysts[8],[17]–[19].

Eftekhari's 2017 paper[14] on tuning electrocatalysts for WOR goes into the improvements of catalyst structure and surface for increased electrocatalytic activity. Since WOR is a reaction that happens within an ultrathin film of material, tuning the surface morphology to the reaction mechanism is important, but because it is a multi-electron transfer tuning for this mechanism is complicated. Favourable morphology for WOR electrocatalysts share the characteristic of a high number of active sites; this can be seen in a non-uniform charge distribution at the surface (more localized active sites), presence of defects, and an amorphous material surface. An amorphous surface is particularly beneficial because the water oxidation reaction itself causes some rearranging and change in the crystallinity of the surface. If the surface is amorphous, its amorphism tends to be increased or preserved during the electrochemical reaction cycle.

In the study by Gorlin and Jaramillo[20], the water oxidation complex in nature inspired the synthesis of an Mn oxide based catalyst for both WOR and the hydrogen reduction reaction (HRR) that reports one of the highest WOR catalyst activities by MnO<sub>x</sub> across the literature. The catalyst was synthesized using voltage cycling from a sodium sulfate and manganous acetate solution (anodic deposition), following a modified procedure from Tench et al.[21]. They used a 0.1M KOH (pH = 13.00) solution for electrochemical testing of the Mn oxide catalyst, also testing commercial carbon-supported Pt, Ir, and Ru-based nanoparticles for benchmarking. The Mn oxide catalyst showed activity of only ~130 mV lower than Pt for HRR, and better activity than Ru and Ir oxide particles for this reaction. For WOR the activity of the Mn oxide catalyst approached the values of Ru and Ir oxide activity, and overall this transition metal-based catalyst has similar potential to the Ir and Ru oxide catalysts as a bifunctional catalyst (meaning it functions as a catalyst in both halves of the water splitting reaction). Gorlin et al. studied their Mn oxide structure with x-ray diffraction (XRD), showing weak crystallinity typical of an alpha-Mn<sub>2</sub>O<sub>3</sub>(222) structure. However, they note that the catalyst behaviour is unusual for this structure, and through SEM explain that the highly nanostructured surface is unusual for alpha-Mn<sub>2</sub>O<sub>3</sub>. X-ray photoelectron spectroscopy (XPS) was used to probe the oxidation state at the surface, showing a relative position of 2p<sub>1/2</sub> and magnitude of multiplet splitting of 3s that are characteristic of Mn<sup>3+</sup> in Mn<sub>2</sub>O<sub>3</sub>. This is the most common oxidation state in the Mn<sub>4</sub>CaO<sub>x</sub> cluster in nature[22].

The Mn<sup>3+</sup> oxidation state has been found to be a critical indicator of Mn-based catalyst activity for WOR[23]–[25]. Robinson et al. studied a variety of common crystal structures of manganese oxides[17] to determine the structural influence in their activity as catalysts for WOR. The authors found that heightened WOR activity typically involved crystal structures with Mn<sup>3+</sup> edge-sharing octahedra with longer Mn-O-Mn bonds, as found in the Mn<sub>2</sub>O<sub>3</sub> and Mn<sub>3</sub>O<sub>4</sub> forms. They propose that since the longer bonds are weaker, they result in more flexibility for the movement of electrons in the WOR reaction. Across the literature, several studies on MnO<sub>x</sub> electrocatalysts have concluded

that a weakened crystal lattice is promising for higher WOR activity results[8], [17], [26], [27]. This is especially evident in poor crystallinity of birnessite-type structures[24], [28], [29], which are representative of repeating sheets of MnO<sub>x</sub> molecules with water found between. Most evidence points to promising MnO<sub>x</sub>-based electrocatalysts being those with an amorphous surface that are nanostructured, as shown in Gorlin et al. and Zaharieva et al.'s methods[18], [19], achieved by electrodeposition of the catalyst material onto an electrode.

Like the Gorlin et al. work, there are many studies where an Mn oxide catalyst for WOR is synthesized from a Mn(II) precursor [20], [23], [30]–[33]. However, these typically require more complex procedures for synthesis, like voltage cycling[20], [30], and the electrochemical activity of these MnO<sub>x</sub> catalysts is usually only considerable in highly alkaline solution. As pointed out in recent reviews of electrocatalysts of WOR, noble metal oxides perform with outstanding activity in acidic conditions, but low-cost transition metal oxides show better activity in very alkaline solution[7], [10], [34]. However, Zaharieva reports a material deposited from Mn(II) on ITO electrode that seems to be active at neutral pH[30] (although the successful deposition protocol still involves voltage cycling). A low-cost and widespread WOR electrocatalysts is ideally active in non-extreme pH. A neutral pH environment is much less degrading to catalyst materials, provides longer term stability, lower cost conditions, and the advantages of a simpler experimental method.

Zhou et al.[32] reports the improvement of activity for WOR by heat treating the MnO<sub>x</sub> material. Their MnO<sub>x</sub> catalysts were electrodeposited from 1M ethylammonium nitrate (EAN) or 1M NaNO<sub>3</sub> with 10mM Mn(CH<sub>3</sub>COO)<sub>2</sub> onto FTO supports and then heat treated at 50, 70, 90, and 120°C for 30 min in air. Electrochemical measurements were performed in 1M NaOH (pH = 14). All synthesis and measurements were performed in a three-electrode system using Ti foil as a counter electrode and saturated calomel electrode (SCE) reference. Although the 50°C treated sample showed a similar Tafel slope to the as-deposited sample, the overpotential was significantly lower than the as-deposited sample, as was the overpotential for all heat treated samples. The results

showed a clear decrease in Tafel slope as the temperature of the heat treatment increased, with 90°C showing the best catalytic activity and lowest Tafel slope. Stability of the 90°C heat treated sample was lower than that of the as-deposited sample, with the 90°C sample showing a decrease in performance until the 8h point in testing for WOR, where the performance stabilized. The current density produced for WOR of the 90°C sample was still higher than the as-deposited film after 8h up to 15h (when stability testing ended).

Interestingly, in the Zhou et al. study[32], XRD patterns, energy-dispersive x-ray (EDX) analysis of atomic ratio, and Raman spectroscopy all show no distinct differences before or after heat treatment of the MnO<sub>x</sub> material. Further analysis using fourier transform infrared (FTIR) spectroscopy showed a decrease in absorption regions of water (specifically 3330-3340 and 1620-1630 cm<sup>-1</sup>) of the heat-treated samples compared to the as-deposited samples. This is indicative of dehydration of the sample, which has been shown for heat treated birnessite-like MnO<sub>x</sub> in previous experiments[35]–[37]. When heat-treated samples are put back into water and then FTIR spectra is examined, they saw a slight increase in intensity of the aforementioned bands, however even after samples are in water for three days, the intensity of the peaks is still smaller than the peaks of the as-grown film. Zhou's research group postulates that heat treatment could cause a permanent removal of structurally incorporated water or hydroxyl groups, however the morphology and bulk composition of the material does not change with heat treatment under 150°C.

For heat treatments higher than 150°C, reports by Ramirez et al.[38] and Chang[38], [39] show that a heat treatment of 300°C or higher on electrodeposited MnO<sub>x</sub> show a reorganization of the material surface. This seems to be because of a reduction of the oxide. A treatment of 400°C or higher is shown by Augustin et al. to cause the MnO<sub>x</sub> to reorganize to higher crystallinity[40].

As reported by the Eftekhari review[8], doping or the addition of foreign elements has shown improvement of many catalysts for WOR because it can improve conductivity as well as affect uniformity of charge distribution (similar to the benefit of defects or weakened crystal structure, as noted previously). Iron addition has been seen previously

in many Ni-based catalysts for WOR[41]–[45]. In particular, a study by Fominykh et al. reports a particularly active iron-doped nickel oxide for WOR[42]. They present a protocol for synthesizing Fe-doped NiO nanoparticles with iron content up to 20 mol% as well as results of their testing for electrocatalyst of WOR. This catalyst is not electrodeposited but rather formed through a solvothermal reaction in tert-butanol, forming crystalline nanoparticles from Ni(acac)<sub>1</sub> and Fe(acac)<sub>3</sub>, and then deposited on a masked quartz crystal microbalance (QCM) electrode. Testing occurred in a three-electrode cell using 0.5 M KOH solution (pH = 13.7) with Pt mesh as a counter electrode and Ag/AgCl/KCl reference electrode. The particles showed the highest activity at 10% Fe(III) content. XRD patterns for all amounts of iron in the material only show broadening indicative of Fe<sub>x</sub>Ni<sub>1-x</sub>O, so Fe atoms are seemingly completely incorporated into the NiO lattice structure.

Improving the support architecture for the electrocatalyst is also important for considerations of surface area and electroconductivity. However, it is more complex because typical catalyst supports like carbon nanomaterials are not automatically an advantage to electrocatalysis[14]. This is because the reaction is not completed at the surface but electron transfer to the electrode is key, so the activity is dependant on the structural proximity of the mesopores with the solid electrode. As well, micropores that would provide an even higher active surface area are not large enough for diffusion of electroactive species in electrochemistry. We did not pursue study of the catalyst support because of these complicating factors.

The fair comparison of electrocatalyst performance for WOR is acknowledged to be difficult to achieve due to the lack of standard measurement conditions applied across the field of research[7], [9]–[11], [14]. In their 2013 paper, McCrory et al.[11] propose a flow chart of measurement techniques to provide a results that would allow for reliable evaluation of catalysts. This proposal includes standard properties to be measured (elemental composition, surface area, catalytic activity, and stability), standard reaction environments (pH), and a standard current density at which to measure the overpotential.

## 1.3 Thesis outcomes

In this thesis I present a simple electrodeposition protocol for the synthesis of an MnO<sub>x</sub> material on FTO glass from a permanganate (Mn(VII)) precursor, unlike most MnO<sub>x</sub> electrocatalysts for WOR which are deposited from Mn(II) precursor. The doping of this material with iron is also explored at different concentrations of iron in solution. All electrocatalysts are tested in a neutral buffer, presenting another advantage to these materials that are Earth-abundant and robust, as well as non-toxic.

This thesis will examine the effect of the iron content on current density in WOR testing, and the effect of iron in the structure of the Fe-MnO<sub>x</sub> material. Finally, I present the possible effect of iron concentration on electronic structure of the Fe-MnO<sub>x</sub> material.

## 2 Background

### 2.1 Electrochemistry

Electrochemistry is the study of the relationship between the electrical and chemical sciences. The majority of this field studies either the electric current produced by a spontaneous chemical reaction (such as in Galvanic cells) or the use of an electric current to drive non-spontaneous chemical reactions that require electron transfer (such as in electrolytic cells). In an electrochemical cell there is an anode, from which electrons leave, and a cathode, where electrons flow into. Anode and cathode are connected to a power source and measuring device, and placed in solution.

In a Galvanic cell the solution is often different on the anode side compared to the cathode, with a salt bridge connecting the two, to provide ions in each half of the cell. This maintains neutrality, otherwise the build-up of positive and negative charge on each electrode would halt the flow of electricity. In an electrolytic cell, anode and cathode can

be in the same electrolyte solution, sometimes separated by a salt bridge to slow the movement of electrons.

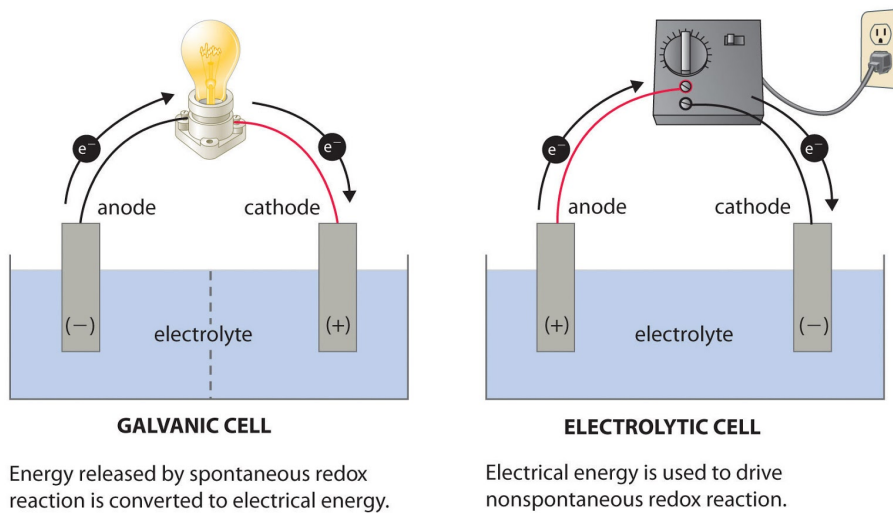
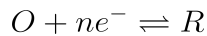


**Figure 2** Basic galvanic and electrolytic cells, showing the difference in the source of energy driving the current in the cell. Figure retrieved from [46]

In usual electrochemical experiments, the reaction is controlled through the voltage difference between two electrodes. The working electrode is where the potential is controlled and where the current is measured. The reaction is typically studied through the measurement of the current. Since electrical characteristics and measurable, these are the quantities studied in electrochemistry, considering electricity and chemical change to be directly related. For example, current can be measured and related to the rate of charge transfer (i.e. movement of electrons) in a reaction. The current can also be the control in an experiment while potential is then measured.

The transfer of electrons in a reaction happens during a redox reaction as described simply in Eq. 4. In this process an oxidized form of the analyte *O* will gain *n* electrons to undergo a reduction and become the reduced form of the analyte *R*. The reaction also proceeds the opposite way.



4

The concentration of the oxidized form ( $C_O$ ) and reduced form ( $C_R$ ) of the redox couple<sup>2</sup> can be related to the electrode potential  $E$  in the Nernst equation, as follows

$$E = E^\circ + \frac{2.3RT}{nF} \log \frac{C_O}{C_R} \quad \underline{\underline{5}}$$

where  $E^\circ$  is the standard redox potential for the reaction,  $R$  is the universal gas constant, and  $T$  is temperature,  $n$  is number of electrons transferred in the reaction, and  $F$  is Faraday's constant.

The study of electrochemical reactions is concerned with the movement of electrons, so the rate of the reaction is an important consideration. This rate is determined by the slowest step in the reaction pathway, which can be put into one of two categories: mass transfer factors in the cell or charge transfer occurring in the reaction. When the reaction is controlled by mass transport, this means that the rate of the reaction is solely determined by the rate at which ions can reach the electrode surface, and this process is reversible. When the reaction is controlled by electron transfer or charge transfer, this means the mass transport is very fast in comparison to the rate at which an electron moves in the redox process, so the rate of reaction is determined by this electron transfer. In this case, the process is considered irreversible.

### 2.1.1 Cyclic voltammetry

The technique of cyclic voltammetry (CV) uses a potentiostat to control the potential between the working and counter electrode (for a diagram of setup, see section 2.3.1 *Potentiostat*, Fig. 11), sweeping the potential up and down between specified voltages. This is done for a specified number of cycles, and the current in the cell is studied as the applied voltage is increased and decreased.

---

<sup>2</sup> Note that this can relate the concentrations of the oxidized and reduced forms of the analyte in the bulk of the solution, or both of those forms at the surface of the electrode.

The applied potential produces a signal as in Fig. 3. As the potential scans into the negative (a to d) the voltammogram shows the produced current (Fig. 4), which reaches a peak at point c when all of the species has been reduced at the cathode surface. At the peak of the *signal* (Fig. 3), point d, the voltage switches, scanning into the positive potential range. As the potential scans into the positive (d to go), the reverse reaction happens and the species at the anode surface are all oxidized at point f.

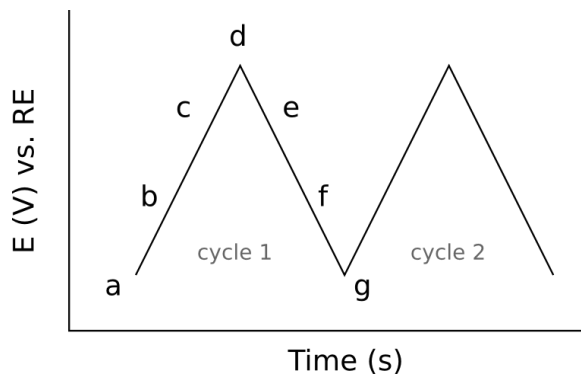


**Figure 3** The input signal in cyclic voltammetry, adapted from [47]

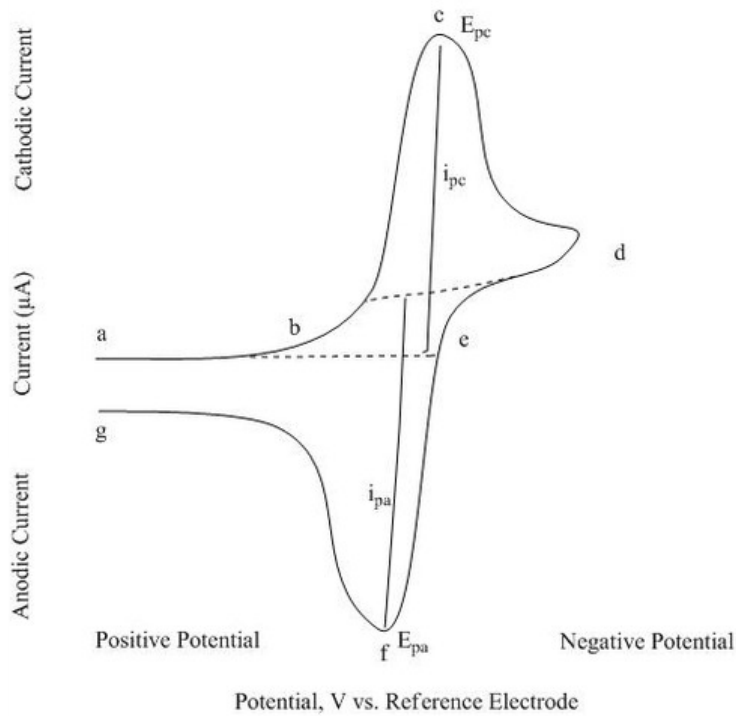


**Figure 4** Resulting voltammogram of a reversible single electron redox process from [47]

The shape of the CV is caused by the diffusion layer forming at the electrode surface. Current increases to a peak as the species at the surface of the cathode is reduced, but once all of the species at the electrode surface are reduced, the reaction becomes diffusion controlled (unreduced species can only get to the cathode by diffusion). Therefore the current drops (c to d) with a dependence of  $t^{1/2}$ , regardless of applied potential. The same happens in the reverse reaction.

The rate of the potential sweep is shown by the slope of the input signal (Fig. 3). Sweep rate is specified for each experiment, and set appropriately to be able to observe all relevant behaviour of the reaction (too slow or too fast may not give clear peaks). However, other techniques are better suited to studying the current of the cell at a held potential (see 2.1.3 *Chronoamperometry*).

Cyclic voltammetry is used to gain information about reactions, such as their reversibility and the steps and intermediates involved in the reaction. The peaks show the redox potential of the species in question. This technique can be used to measure characteristics of a process, such as finding the unknown concentration of a solution that undergoes a reversible reaction, since concentration and current are proportional in this case. CV can also provide a sense of the consistency of a material's performance, in comparing each cycle with the cycle(s) previous as the measurement proceeds.

## 2.1.2 Chronoamperometry

Chronoamperometry (CA) is another electrochemical method of gaining measurements, such as testing a material's water oxidation activity. In this technique the potential is stepped up and held for a certain amount of time, providing a measurement of current at that specific potential. Since the measurement is held for  $t > 50\text{ms}$ , the effect of any residual current is negligible. Residual current appears in the form of charging current (movement of ions due to the initial charge on the electrode causing a double layer to

form) or reduction/oxidation of trace impurities. Since the potential is being applied steadily for a longer time, CA measurements are more indicative of true activity of a reaction at a given potential.

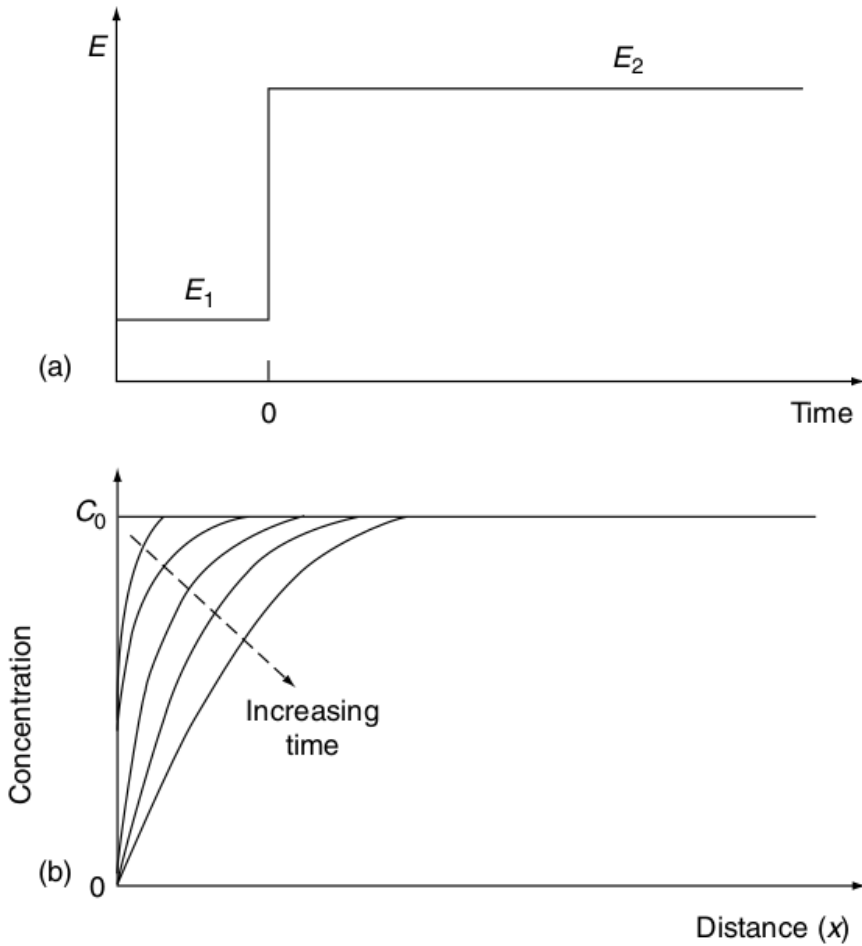


**Figure 5** The input signal in chronoamperometry (a) and resulting concentration profile at different times (b), retrieved from [48]

As in Fig. 5(a), the input signal in CA is simply a step from one potential to another. In a CA experiment it is common to hold the potential for a specified amount of time, and then move to the next potential step (up or back down). At the beginning of the experiment, the step is from a current where the reaction is not occurring (no current produced) to a potential where there is no more reactant at the surface of the electrode

(i.e. reaction is complete to a certain distance away from the electrode). This can be seen in Fig. 5(b) where over time, the concentration of the reactant  $C_O$  near the electrode decreases. This behaviour is seen because the mass transport in the experiment is entirely due to diffusion. This gives a current-time dependence that can be described by the Cottrell equation (Eq. 6).

$$i(t) = \frac{nFACD^{1/2}}{\pi^{1/2}t^{1/2}} = kt^{-1/2} \quad \underline{6}$$

Where  $n$  is the number of electrons,  $F$  is Faraday's constant,  $A$  is the surface area of the electrode,  $C$  is the concentration of ions, and  $D$  is the diffusion coefficient. Describing the experiment in this way allows us to measure the diffusion coefficient or active surface area in a reaction. This also probes the reaction mechanism at the electrode by measuring the current response at different potentials.

### 2.1.3 Tafel plots

When reactions are controlled by the rate of electron transport, and not the rate of mass-transport, then the rate of the reduction reaction  $V_R$  is Eq. 7 and the rate of the oxidation reaction  $V_O$  is Eq. 8.

$$V_R = k_R C_O(t) \quad \underline{7}$$

$$V_O = k_O C_R(t) \quad \underline{8}$$

where  $k_R$  and  $k_O$  are heterogeneous rate constants as in Eq. 9 and Eq. 10, respectively.  $C_O$  and  $C_R$  are the concentrations of the oxidized and reduced forms of the redox couple at the anode and cathode, respectively.

$$k_R = k^\circ \exp[-\alpha nF(E - E^\circ)/RT] \quad \underline{9}$$

$$k_O = k^\circ \exp[(1 - \alpha)nF(E - E^\circ)/RT] \quad \underline{10}$$

$k^\circ$  is the standard heterogeneous rate constant and  $\alpha$  is the transfer coefficient.  $\alpha$  is a value representing the symmetry of the free-energy curve of the system, a fraction from 0 to 1 representing the energy in the system that is used to lower the activation energy.

The current produced by oxidation and reduction in the system are proportional to the oxidation and reduction rates, respectively.

$$i_R = nFAV_R \quad \underline{11}$$

$$i_O = nFAV_O \quad \underline{12}$$

Combining these relationships with Eq. 7 and Eq. 8, we can obtain the overall current in the reaction due to the difference in oxidation and reduction currents (Eq. 13).

$$i_{net} = i_R - i_O = nFA[k_R C_O(t) - k_O C_R(t)] \quad \underline{13}$$

This becomes the Butler-Volmer equation[49] through use of the full expressions for  $k_R$  and  $k_O$

$$i_{net} = nFAk^\circ \{C_O(t) \exp \left[ \frac{\alpha nF(E - E^\circ)}{RT} \right] - C_R(t) \exp \left[ \frac{(1 - \alpha)nF(E - E^\circ)}{RT} \right]\} \quad \underline{14}$$

When the cell potential reaches the standard redox potential for the reaction (i.e.  $E = E^\circ$ ), then  $i_{net} = 0$ . However, charge is still moving within the reaction, but the anodic and cathodic currents are equal. The exchange current  $i_0$  is the absolute magnitude of the anodic and cathodic components of the net current, as shown in Eq. 15.

$$\begin{aligned}
 i_0 &= i_a = nFAk^\circ C_O^* \exp\left[-\frac{\alpha nF}{RT}(E - E^\circ)\right] \\
 &= i_c = nFAk^\circ C_R^* \exp\left[-\frac{(1-\alpha)nF}{RT}(E - E^\circ)\right]
 \end{aligned} \tag{15}$$

Where  $C_O^*$  and  $C_R^*$  are the bulk concentrations of the oxidized and reduced forms of the redox couple, respectively. Since these concentrations are related by the Nernst equation (Eq. 5) at equilibrium, we can express the exchange current density  $j_o$  as follows

$$j_o = nFk^\circ(C_O^*)^{1-\alpha}(C_R^*)^\alpha \tag{16}$$

The current density ( $j$ ) and applied overpotential ( $\eta$ ) can then be related using the form of the Butler-Volmer equation as seen in Eq. 18, remembering that  $j_o$  is the absolute magnitude of the cathodic and anodic currents when they are equal to each other. The overpotential  $\eta$  can be described as the applied potential ( $E$ ) minus the equilibrium potential ( $E_{eq}$ ), as seen in Eq. 17.

$$\eta = E - E_{eq} \tag{17}$$

$$j = j_o \left[ -\frac{C_O}{C_O^*} \exp\left(-\frac{\alpha_c F \eta}{RT}\right) + \frac{C_R}{C_R^*} \exp\left(-\frac{\alpha_a F \eta}{RT}\right) \right] \tag{18}$$

where  $\alpha_c$  and  $\alpha_a$  are just the transfer coefficient at the cathode and anode, respectively.

When we consider the case where the concentrations of the species at the electrode surfaces and in bulk are not substantially different (i.e. the reaction is charge-transport driven instead of mass-transport driven, meaning charge transfer is the limiting mechanism) then we gain a form of the Butler-Volmer equation in Eq. 20.

$$C_O - C_O^* \approx 0 \quad C_R - C_R^* \approx 0 \quad \underline{\underline{19}}$$

$$j = j_0 \left[ \exp \left( \frac{\alpha_a n F \eta}{RT} \right) + \exp \frac{\alpha_c n F \eta}{RT} \right] \quad \underline{\underline{20}}$$

In this charge-transfer-limiting case, a large overpotential is typically needed to drive the reaction. The Tafel equation comes from the Butler-Volmer equation (Eq. 20) under high anodic or cathodic overpotentials, which is relevant because WOR occurs at high overpotentials at the anode. In such a case, the overall current is mainly attributed to the anode with a negligible cathodic current, therefore giving us the equation in Eq. 21. This is the Tafel equation[50] and it can provide information about the mechanisms of the reaction in question.

$$j \approx j_0 \exp \frac{\alpha_a n F \eta}{RT} \quad \underline{\underline{21}}$$

The Tafel equation is most useful when translated to logarithmic form as in the anodic Tafel equation (Eq. 22).

$$\log(j) = \log(j_0) + \frac{\eta}{b} \quad \underline{\underline{22}}$$

where

$$b = \frac{2.303 RT}{\alpha_a n F} \quad \underline{\underline{23}}$$

and is also useful as stated in Eq. 24, where the relationship between the overpotential and the slope can be clearly seen. The Tafel slope  $b$  is an important indicator of how fast the current density  $j$  increases in relation to the overpotential  $\eta$ .

$$\eta = b \cdot \log \left( \frac{j}{j_0} \right)$$

24

If the Tafel slope is small, this indicates a significant increase in current density with smaller change in overpotential. If  $b$  is large, a relatively high increase in potential must be applied to see significant changes in the current density. The Tafel slope mostly depends on the transfer coefficient  $\alpha_a$  (Eq. 23) so a small slope implies a higher transfer coefficient, and therefore tells us something about the electrode kinetics.[51]

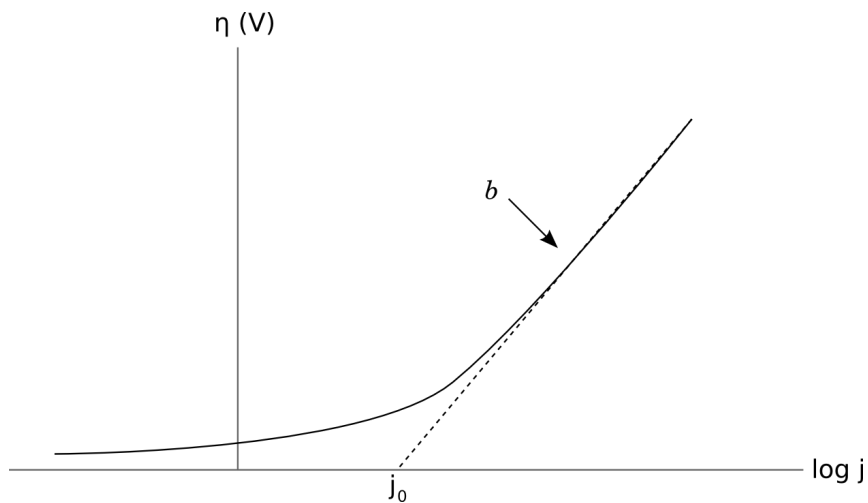


**Figure 6** Example of a Tafel plot, with slope  $b$  indicated in the Tafel region, and exchange current  $j_0$ .

The charge transfer coefficient  $\alpha_a$  gives information about the rate-determining step (RDS) in a multiple-electron reaction. In a reaction being studied there are typically multiple steps that occur consecutively and consist of charge-transfer or chemical steps. These relate to the transfer coefficient through [49], where  $n_t$  is the number of electrons that leave the electrode before the RDS,  $\nu$  is the number of RDS that happen in the

written electrode reaction,  $n_r$  is the number of electrons that take part in the RDS, and  $\beta$  is the symmetry coefficient<sup>3</sup>.[52]

$$\alpha_a = \frac{n_t}{\nu} + n_r \beta \quad \underline{25}$$

If we have a four-electron transfer system where the RDS is the third electron transfer step, then  $n_t = 2$  (two electron transfer steps occur before the RDS),  $\nu = 1$ ,  $n_r = 1$ ,  $\beta = 0.5$  so we get  $\alpha_a = 2.5$ . Looking to Eq. 23, this gives us a Tafel slope  $b$  of 24 mV dec<sup>-1</sup>. In general, a smaller Tafel slope indicates an RDS toward the end of a multi-electron transfer reaction[51]. This is another reason for a small Tafel slope's indication of a promising electrocatalyst.

## 2.1.4 Electrodeposition

Electrodeposition uses reactions that require a transfer of electrons to cause the formation of a film or deposit a material. In this process, a cell is set up wherein typically the cathode is the material to be deposited on (electrons will be supplied to the cathode i.e. forming the material) and the electrodes are placed in a solution containing the desired material ions. A power supply then provides the electrons needed for the reaction to proceed. Electrons moving to the cathode react with the compounds in solution, producing a solid on the surface of the cathode. The reaction at the cathode concerning the reduction of metal ions depositing metal  $M$  is as follows




---

<sup>3</sup> The symmetry coefficient  $\beta$  is often assumed to be around 0.5 because  $\beta = \frac{1}{2} + \eta / \lambda$  and the overpotential  $\eta$  is typically much smaller than the reorganization energy  $\lambda$ .

The anode reaction is either a dissolution providing metal ions, or (as is the case in our experiments, see 3.1.2 *Electrodeposition of MnO<sub>x</sub>*) is a material that will drive water oxidation as in Eq. 27.



Among the many methods of depositing a material on a support, the technique of electrodeposition is very useful in the formation of metals and conducting materials for electrochemical experiments. This is because it allows for precise control over the nanostructure of the film. The film thickness is controlled by length of deposition time, and the morphology is controlled by the morphology of the target substrate. The other advantage electrodeposition presents is its simplicity and ease of use, since this method does not require complicated environments involving high temperatures or vacuum.

However, there is some non-uniformity in the current distribution on an electrode, since any edges or corners of the substrate surface area will have a slightly increased current density (the ion density at these edges is higher). Therefore, there is some non-uniformity in the thickness of the electrodeposited material at the edges as well. This makes electrodeposition a less ideal technique for substrate surfaces with many features, edges, and corners.

## 2.1.5 Water oxidation reaction

In an electrochemical cell for testing water oxidation, a buffer electrolyte solution is used to provide H<sub>2</sub>O for water splitting and also remove any excess ions that are produced in the reaction to maintain a constant pH in the cell. The working electrode in WOR testing is the electrode at which the reaction will take place. The counter electrode is a material that reduces hydrogen efficiently to complete the redox cycle, commonly a Pt wire.

The activity on the surface of the catalyst is highly dependent on the specific pH in solution, since ions are produced as the reaction proceeds. The most quoted overpotential for the WOR half-reaction of water splitting is  $E = 1.23$  V, at a pH of 0. As pH rises, per unit, there is a decrease in potential of 0.59V. However, this decrease occurs at both electrodes meaning the difference in overpotential for the overall reaction remains consistent. The two common reaction mechanisms in acidic and alkaline conditions are as follows:

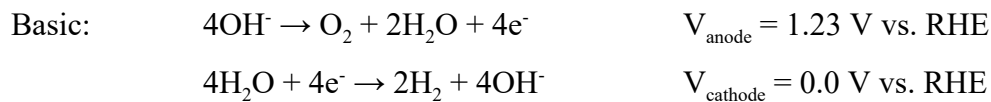
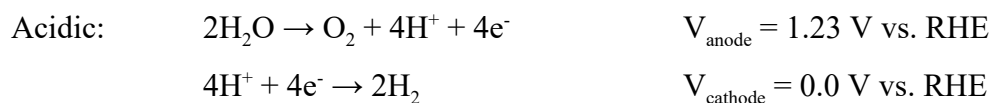


**Figure 7** Reaction mechanisms for WOR under different pH conditions.[53]

Since the pH of the solution determines what half-reactions will be taking place, the material of the electrodes and pH of the solution must be considered together. Typically, noble metal oxides such as RuO<sub>2</sub> and IrO<sub>2</sub> perform best in acidic solution, whereas transition metal oxides are known for their higher activity under basic conditions. Only a few materials have been shown to effectively catalyze this reaction in a neutral pH environment, MnO<sub>x</sub> being one of them (see 1.2 *Literature review* for details on studies of specific materials).

WOR is complex because it is a multistep reaction that requires movement of four electrons. Many different pathways have been suggested for this reaction but all involve oxygen or oxygen-containing species being adsorbed to the electrode surface (metal or metal oxide) in the first step.[54] This adsorption is proposed to continue on the parts of the surface that are already oxidized as well.

Because of the variety of chemical pathways proposed for WOR, analysis of the reaction is difficult. Comparison of studies across the literature is a complex undertaking (see 1.2 *Literature review*) because the experimental data has so many variable contributing factors to consider, such as temporal changes in the reaction surface, impurities in the solution, and pretreatment of the catalyst in electrochemical testing processes.

## 2.2 Electronic structure

Electrons play an important role in the properties of materials, and an especially important role for a catalyst for a redox reaction such as WOR. The property and behaviour of the material in reaction can be explored through various descriptions of electron behaviour. Here I outline a few of these electronic concepts that are relevant to my experiments and discussion.

We start with the time independent Schrödinger equation

$$\hat{H}|\psi\rangle = \epsilon|\psi\rangle \quad \underline{\text{28}}$$

where the Hamiltonian is of the form

$$\hat{H} = \hat{T} + \hat{V} \quad \underline{\text{29}}$$

with  $\hat{T}$  being kinetic energy, and  $\hat{V}$  being the potential.

The Schrödinger equation in a 1D infinite potential well is as follows

$$\frac{-\hbar^2}{2m} \frac{\partial^2}{\partial x^2} \Psi_n = \epsilon_n \Psi_n \quad \underline{\text{30}}$$

where the first term is  $\hat{T}$  acting on  $\Psi_n$  and  $\hat{V} = 0$  at all points inside the potential well. The solutions of this equation are of the form

$$\Psi_n = A \sin\left(\frac{2\pi}{\lambda_n}\right); \quad \frac{1}{2}n\lambda_n = L \quad \text{where } n = 1, 2, 3, \dots \quad \underline{\text{31}}$$

corresponding to the energies

$$\epsilon_n = \frac{\hbar^2}{2m} \left(\frac{n\pi}{L}\right)^2 \quad \underline{\text{32}}$$

For a system of N non-interacting electrons in this system, the Fermi energy  $\epsilon_F$  is

$$\epsilon_F = \frac{\hbar^2}{2m} \left(\frac{N\pi}{2L}\right)^2 \quad \underline{\text{33}}$$

since  $N/2$  is the  $n$  level (because 2 electrons may sit at each level, the topmost filled level will be  $N/2$ ). Understanding the concept of the Fermi energy (or Fermi level) is important. It is the hypothetical energy level of an electron where at thermodynamic equilibrium, the energy level has an exactly 50% probability of being occupied. This can also be defined as the energy level of the chemical potential  $\mu$  at T = 0K, which for metals is the highest occupied energy level. At the Fermi level at T = 0K,  $f(E) = 1/2$ .

The Fermi-Dirac distribution (Eq. 34) describes the occupied energy levels of a system at finite temperatures, with  $\mu$  being the chemical potential of the system.  $\mu$  is always at  $f(E) = 1/2$ .

$$f(E) = \frac{1}{e^{(E-\mu)/k_B T} + 1} \quad \underline{\text{34}}$$

Moving toward a more realistic system, a free electron gas (non-interacting electrons) in three dimensions, the Schrödinger equation is

$$-\frac{\hbar^2}{2m} \left( \frac{\partial^2}{\partial x^2} + \frac{\partial^2}{\partial y^2} + \frac{\partial^2}{\partial z^2} \right) \Psi_k(\vec{r}) = \epsilon_k \Psi_k(\vec{r}) \quad \underline{35}$$

with the assumption that  $\hat{V} = 0$  everywhere. The solutions are

$$\Psi_k(\vec{r}) = \exp(i\vec{k} \cdot \vec{r}) \quad \underline{36}$$

where

$$k_x = 0, \pm \frac{2\pi}{L}, \pm \frac{4\pi}{L}, \dots, \pm \frac{2n\pi}{L} \quad \underline{37}$$

and similarly for  $k_y$  and  $k_z$ , where  $\vec{k}$  is a wavevector, which represents wavelength and direction of the wave (i.e. small  $\vec{k}$  represents a large wavelength with low energy, large  $\vec{k}$  represents a small wavelength with high energy).

The density of states (DOS) is a histogram of these solution energy states for a system. Plotting the DOS gives  $\epsilon_n$  (the energy states) for all  $n$  against the number of states at each energy level.

## 2.2.1 Molecular orbital theory

Molecular orbital theory can follow from the representation of systems of electrons, atoms, and molecules as eigenvectors (eigenstates) and their measurable quantities as eigenvalues (e.g. energy). Any complete basis set can be chosen to represent the system, and eigenstates can then be projected onto this basis.

For example, if we use very generalized  $|s\rangle$ ,  $|p\rangle$ , and  $|d\rangle$  as a basis for a system of one atom, where  $|s\rangle$ ,  $|p\rangle$ , and  $|d\rangle$  are the eigenstates of the system, so the Hermitian matrix is already diagonalized.

$$\begin{bmatrix} \langle s|\hat{H}|s\rangle & \langle s|\hat{H}|p\rangle & \langle s|\hat{H}|d\rangle \\ \langle p|\hat{H}|s\rangle & \langle p|\hat{H}|p\rangle & \langle p|\hat{H}|d\rangle \\ \langle d|\hat{H}|s\rangle & \langle d|\hat{H}|p\rangle & \langle d|\hat{H}|d\rangle \end{bmatrix} \quad \underline{\text{38}}$$

Since  $|s\rangle$ ,  $|p\rangle$ , and  $|d\rangle$  are orthogonal, all values of the matrix are 0 except  $\langle s|\hat{H}|s\rangle$ ,  $\langle p|\hat{H}|p\rangle$ , and  $\langle d|\hat{H}|d\rangle$ . These eigenvalues will be  $\epsilon_s$ ,  $\epsilon_p$ ,  $\epsilon_d$  respectively. These values are found by solving

$$\langle s|\hat{H}|s\rangle = \int_{-\infty}^{\infty} s^*(x) \left[ -\frac{\hbar^2}{2m} \left( \frac{\partial^2}{\partial x^2} + \frac{\partial^2}{\partial y^2} + \frac{\partial^2}{\partial z^2} \right) + V(x) \right] s(x) dx \quad \underline{\text{39}}$$

This is solved similarly for  $\langle p|\hat{H}|p\rangle$  and  $\langle d|\hat{H}|d\rangle$ ). In the case of one atom, the potential is

$$V(x) = -\frac{e^2}{r} \quad \underline{\text{40}}$$

With this in mind, a two-atom system has a potential

$$V(x) = \frac{-e^2}{r} + \frac{q_1 q_2}{r_1 r_2} \quad \underline{\text{41}}$$

which gives the more difficult Hamiltonian

$$\hat{H} = -\frac{\hbar^2}{2m} \left( \frac{\partial^2}{\partial x^2} + \frac{\partial^2}{\partial y^2} + \frac{\partial^2}{\partial z^2} \right) + \frac{-e^2}{r} + \frac{q_1 q_2}{r_1 r_2} \quad \underline{\text{42}}$$

This is much harder to integrate when solving for the values of the Hermitian matrix.

$$\begin{bmatrix} \langle s_1 | \hat{H} | s_1 \rangle & \cdot & \cdot & \cdot & \cdot & \langle s_1 | \hat{H} | d_2 \rangle \\ \cdot & \langle p_1 | \hat{H} | p_1 \rangle & \cdot & \cdot & \cdot & \cdot \\ \cdot & \cdot & \langle d_1 | \hat{H} | d_1 \rangle & \cdot & \cdot & \cdot \\ \cdot & \cdot & \cdot & \langle s_2 | \hat{H} | s_2 \rangle & \cdot & \cdot \\ \cdot & \cdot & \cdot & \cdot & \langle p_2 | \hat{H} | p_2 \rangle & \cdot \\ \langle d_2 | \hat{H} | s_1 \rangle & \cdot & \cdot & \cdot & \cdot & \langle d_2 | \hat{H} | d_2 \rangle \end{bmatrix} \quad \underline{\text{43}}$$

This matrix is also more difficult to diagonalize. This is because in the one-atom matrix (Eq. 38) all off-diagonal elements produced 0 due to the orthogonal basis set, so for example  $\langle s | p \rangle = 0$ . In this case those basis states involving the same atom are still orthogonal, so  $\langle s_1 | p_1 \rangle = 0$ . However,  $\langle s_1 | p_2 \rangle \neq 0$  and this means the matrix will have non-zero off-diagonal values. The physical explanation for this is due to the electrostatic interaction between the two atoms. If the atoms were very far apart, then all off-diagonal elements would be effectively zero.

The diagonalization of this matrix requires an overlap matrix  $\hat{S}$  which represents the strength of the electrostatic interaction between any two elements. The resulting eigenvalues represent energy level splitting, and the eigenvectors represent antibonding and bonding states. Eigenvectors of the form

$$\begin{aligned} |s_1\rangle - |s_2\rangle &\quad \text{antibonding state} \\ |s_1\rangle + |s_2\rangle &\quad \text{bonding state} \end{aligned} \quad \underline{\text{44}}$$

This is analogous to the traditional molecular orbital diagrams, as in Fig. 8

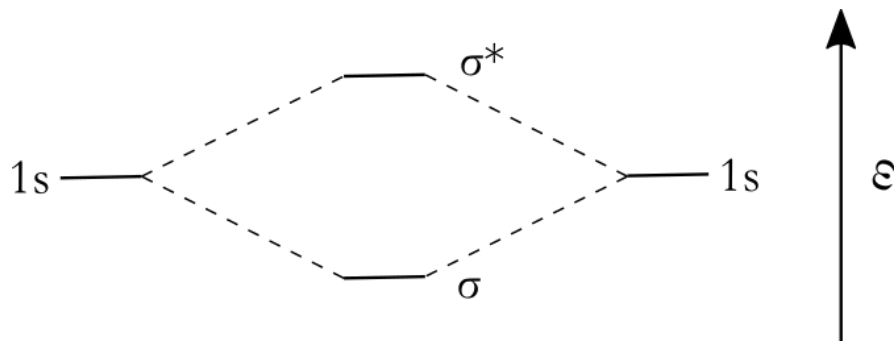


**Figure 8** A simple MO diagram representing two atoms with one 1s electron each splitting to create  $\sigma$  and  $\sigma^*$  bonding and antibonding orbitals.

## 2.2.2 Band structure

As more atoms are added to the system, these orbitals continue to split until the energy levels available become so many that we model them as a continuum, represented as a band.

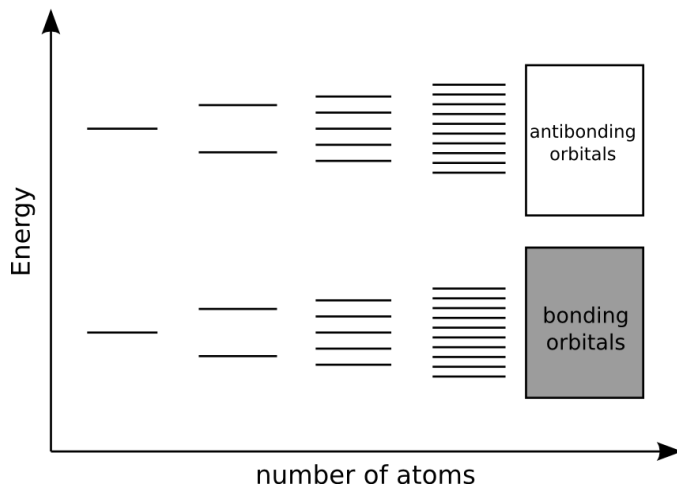


**Figure 9** A simplified representation of the theory of localized molecular orbitals splitting as the system size grows, until the energy levels become a continuum represented as bands. Adapted from [55]

The band structure of a material comes about through this description of electrons in a large periodic lattice of atoms/molecules. Two electrons in an atom will occupy one atomic orbital at one energy level (with opposite spins), however when this atom is joined by another, the atomic orbitals will overlap and since electrons are fermions, they must obey the Pauli Exclusion principle. This means that two electrons cannot occupy the same quantum state, and in this scenario they split into two orbitals of different energies. Eventually, as a large number of atoms join to form a solid material, the overlap of atomic orbitals becomes so significant that the space in energy between all of these levels becomes very small, forming a continuum of energy levels called an energy band.

One description of a solid material is through the electronic band structure model, looking at the energy levels that electrons may occupy as a continuum of energy bands. A material can be described through its band structure to gain some insight related to the characteristics of the material. Band structure theory has some limitations; it assumes a homogeneous, bulk system of atoms that dictates intrinsic band structure of a material of non-interacting electrons. However it is still a useful starting point for explanation of electron behaviour in a material.

### 2.2.3 Work function

The work function is defined as the amount of energy needed to move an electron from a solid material to a point in vacuum. It is defined as in Eq. 45.

$$\Phi = -eV_E - E_F \quad \underline{45}$$

where  $V_E$  is the electrostatic potential and  $E_F$  is the Fermi level. The first term represents the energy of an electron in nearby vacuum, so this can be rewritten as

$$\Phi = E_0 - E_F \quad \underline{46}$$

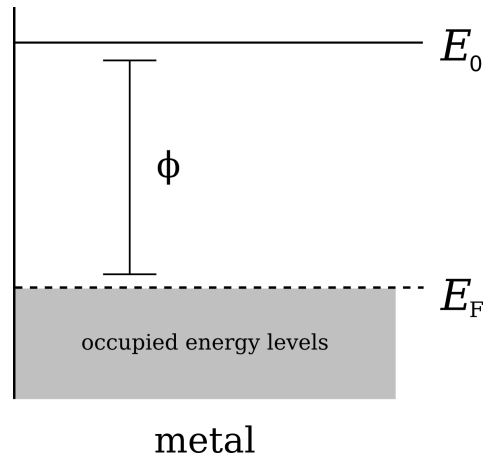


**Figure 10** A simplified representation of the work function for a metal where  $E_F$  is the Fermi level,  $E_0$  is the vacuum level, and  $\phi$  the work function of the material.

The work function that is found for a material does not only result from the average electrostatic potential of the material, but involves surface states and crystal structure too. Each crystal facet or “cut” of a material has a different work function because the layout of these atoms informs the atomic-scale double layer that is formed at the interface (see 2.1.2 *Chronoamperometry* for a more complete description of the double layer). This double layer can be affected by the presence of other elements on the surface, but even on a clean surface, an electric dipole is created between the material and vacuum. This causes a spike in the electrostatic potential at this surface, which in turn affects the work function of the material.

## 2.3 Instrumentation

Next I have included an overview of the instrumentation used in the experiments described. This includes explanation of the theory behind the operation of the instruments

and measurements taken, as well as diagrams to explain the principle concepts relating to the instruments.

### 2.3.1 Potentiostat

A potentiostat controls a three-electrode cell consisting of a working electrode (WE), counter electrode (CE, sometimes called auxiliary electrode or AE), and reference electrode (RE), in which experiments to analyze a reaction happen at the WE. The potential at the WE is maintained constant relative to the RE, and the current between the WE and CE is measured.

To make a measurement of potential, at least two electrodes are needed, and this is why the RE is required. Since the reaction being studied is happening at the WE, the electrode that the potential is being measured relative to needs to be very stable over time so we can be sure observed changes in potential are due to the activity at the WE. The RE consists of a half-cell reaction isolated in its own chamber, which has a defined constant potential with respect to the standard hydrogen electrode.

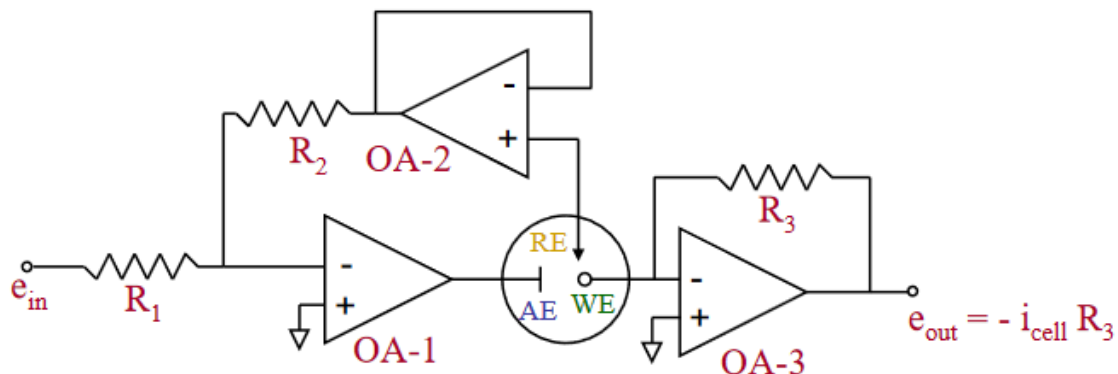


**Figure 11** Diagram of the circuit configuration of a simplified potentiostat from [56]

The CE acts as the counter to the working electrode to ensure a flow of electrons (current) in the cell. The reactions being studied are redox reactions, meaning for electrons to move, oxidation and reduction must both be happening in the cell, so one will happen at the WE while the other occurs at the CE.

As can be seen in Fig. 11, to control and measure the potential and current in the cell, a voltage source ( $e_{in}$ ) drives a circuit with multiple operational amplifiers (OAs), two of which act in feedback loops (OA-2 and OA-3) at controlling the RE and WE. The voltage from  $e_{in}$  control the applied potential at WE where the reaction of interest is typically taking place. In operational amplifiers, the polarity of the incoming signal is inverted (-) in one input, and the other input is non-inverted (+). In a configuration such as these feedback loops, the operational amplifier will adjust the output value to maintain a zero difference between the input signals.

At OA-2, the potential difference between the RE and WE is measured. As Fig shows, there is very high input impedance to OA-2, resulting in no current passing to the RE, so the reference potential is stable. The output of OA-2 feeds a signal to OA-1 where changes cause a varying input at the inverted (-) input signal to OA-1. This causes OA-1 to balance the inputs by forcing current into the cell at the AE (current between AE and WE). The result is a voltage drop after OA-3 since  $e_{out} = -i_{cell}R_3$ , and this allows for a measurement of the current in the cell.

Various forms of input signal for the voltage at  $e_{in}$ . These include stepped potentials as in chronoamperometry, and linearly increasing and decreasing signals such as in cyclic voltammetry.

### 2.3.2 XPS

In x-ray photoelectron spectroscopy (XPS), an area on a sample's surface is irradiated with a beam of x-rays. The kinetic energy and number of electrons escaping at the surface (between 0-10nm) are measured. This gives a plot of the number of electrons as a

function of the binding energy, which gives information about the elements present on the surface of the sample. Using the energy of the x-ray's particular wavelength, electron binding energy is found using Eq. 47, where  $\Phi$  is a term that is adjustable based on the instrument, accounting for the kinetic energy absorbed by the detector.

$$E_{\text{binding}} = E_{\text{photon}} - (E_{\text{kinetic}} + \Phi)$$

**47**

A theoretical schematic of XPS in progress is depicted in Fig. 12. An incoming x-ray (denoted by  $h\nu$ ) with a specific energy hits the material, releasing photoelectrons at a certain energy level (in this schematic those in the 1s energy band).

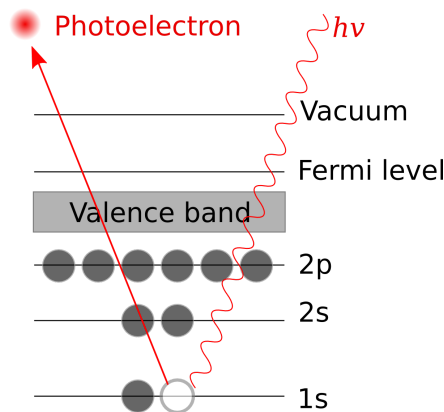


**Figure 12** Diagram of the principle behind XPS measurements, adapted from [57].

XPS measurements are performed in high or ultra-high vacuum. They typically measure the parts per thousand of an element which can be used to find the empirical formula of the material in the sample. This technique also provides information about the chemical and electronic state of the surface of the sample.

To find a quantitative analysis of the elements in a sample containing different elements, XPS data requires application of relative sensitivity factors (RSFs).[58] This is due to overlap of lines from different species, meaning only a portion of the core level measurement should be used to quantify a particular species. The RSFs reflect the likelihood of a photoelectron being produced from a particular orbital and element, e.g.

the result is the fraction of a line that should be used to quantify each element within the overlap.

### 2.3.3 FESEM

A field emission scanning electron microscope (FESEM) uses an electron beam to produce highly magnified images of a sample's surface at nanometer length scales. A schematic of a simplified FESEM system is shown in Fig. 13. The electron beam is created by a field emission gun, which is an emitter with tip that is sharply pointed to a radius in the hundred nm range. The emitter is held at a very highly negative potential (kV range) that produces a surface potential gradient high enough for emission of electrons to occur. The electrons move from the tip to the sample, directed by electromagnetic lenses. The primary electrons interact with the specimen, causing the emission of secondary electrons. These secondary electrons are collected by a detector and processed through a scanning circuit and photo multiplier to produce a signal for viewing or photography.

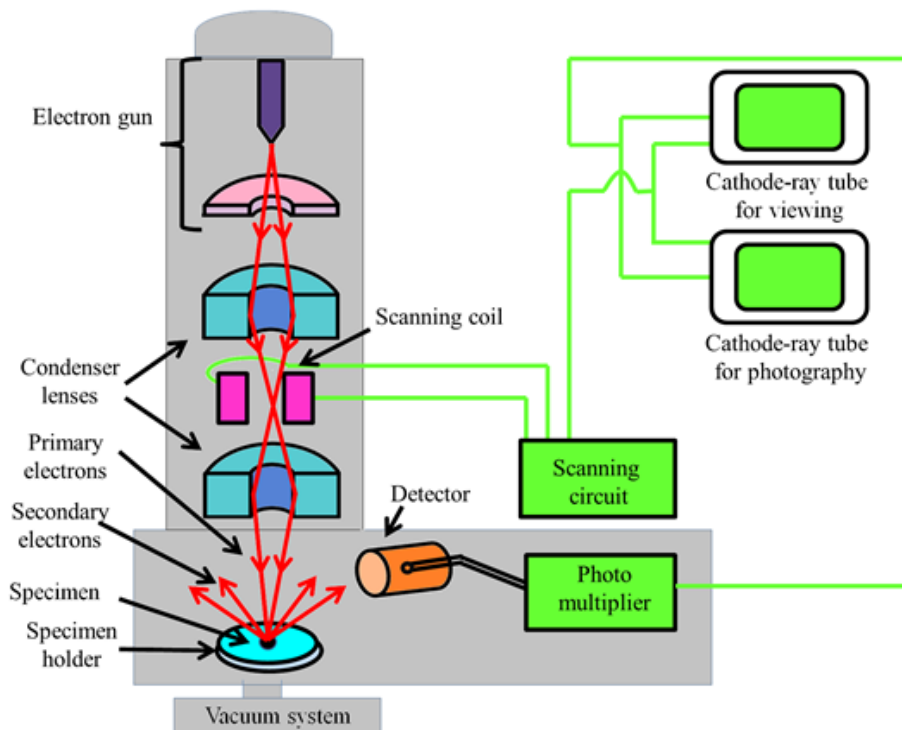


**Figure 13** Simplified diagram of the FESEM instrument, retrieved from NPTEL[59]

When the primary electron beam hits the sample, the electrons lose energy to a certain interaction volume of the sample. This loss of energy in the form of inelastic scattering causes excitement of electrons in the atoms near the surface of the material. If the electrons gain sufficient energy, they escape the sample surface as secondary electrons. These secondary electrons are attracted to a detector, which they hit at a certain position, angle and velocity that is translated to a digital image. Some of the primary electrons reflect off of the surface and deeper levels of the sample. These backscattering electrons hit a second detector which gives more depth to the information translated to the image. FESEM has the advantage over SEM (scanning electron microscopy) that it uses electrical potential, and not heat, to produce electrons. Therefore it can produce higher energy electrons with no thermal drift to account for, resulting in brighter images.

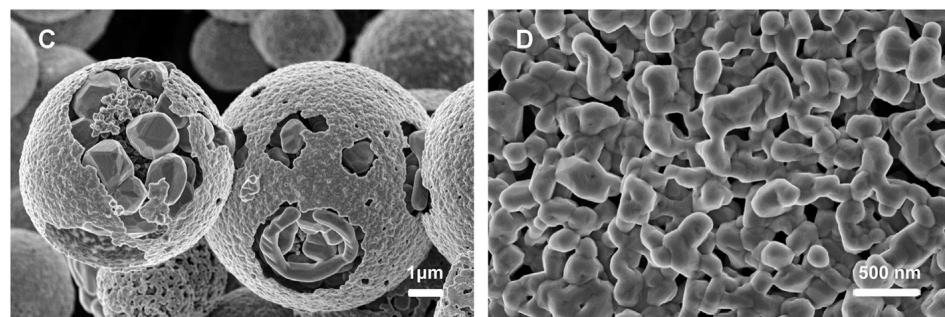


**Figure 14** Example of the clarity of an FESEM image at a 1 μm and 500 nm scale. Nanostructured colloidal manganese oxide particles from [60].

The electron beam scans across the sample, moving around a defined area. The result is a grayscale image with a brightness value per pixel, showing a 3D structure of the surface of the sample, as in Fig. 14.

### 2.3.4 Kelvin Probe

A Kelvin Probe measures the work function of a material using the principle that electrons in a material with a lower work function will flow to a material with higher work function.

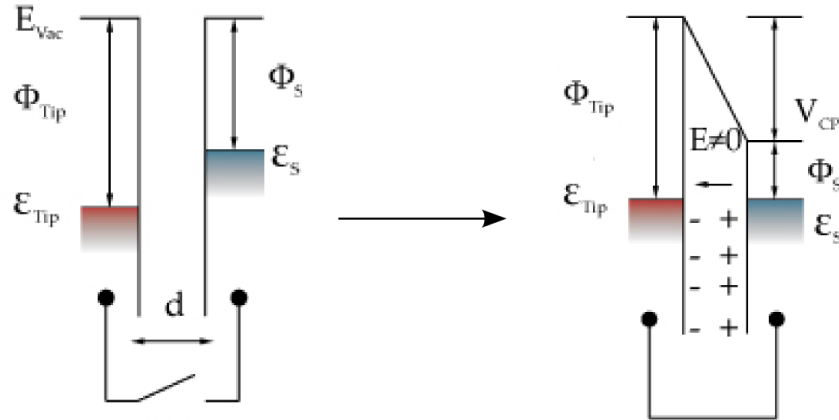


**Figure 15** Theory behind the calculation of the work function in a Kelvin probe measurement, adapted from [61].  $\Phi_{\text{Tip}}$  &  $\epsilon_{\text{Tip}}$  and  $\Phi_s$  &  $\epsilon_s$  are equal to the work function & Fermi level of the tip and surface respectively. When two materials with different Fermi levels are put into contact, these levels align resulting in an energy difference  $V_{\text{CP}}$ .

A contact potential ( $V_{\text{CP}}$ ) is produced between the surfaces of two conductors that are in contact, and this potential depends on their work function. In a Kelvin Probe, a sample and probe are brought into electrical contact, and made into parallel plate capacitors, where the voltage held by the capacitor is  $V_{\text{CP}}$ . To measure  $V_{\text{CP}}$ , an external backing potential is applied ( $V_b$ ). When the charge is 0 on the “plates”, then  $V_b = -V_{\text{CP}}$  so the contact potential is determined, as shown in Fig. 16. The Kelvin Probe has a relative resolution of 1 - 3 mV.[62]

The Kelvin probe works as follows: the probe tip vibrates, producing a varying capacitance shown in Eq. 48, where  $C$  is the capacitance,  $Q$  is the charge,  $V$  is the potential,  $\epsilon$  is the permittivity of the dielectric,  $A$  is the surface area of the capacitor, and  $d$  is the separation between plates.

$$C = \frac{Q}{V} = \frac{\epsilon A}{d} \quad \underline{\text{48}}$$

As the probe oscillates,  $d$  varies. Since the charge  $Q$  is constant,  $V$  then changes with  $d$ , and this change is recorded. From this measurement a peak-to-peak voltage  $V_{ptp}$  is given by Eq. 49. Here  $\Delta V$  is the potential between the sample and tip of the probe,  $R$  is the  $I/V$  converter feedback resistance,  $C_0$  is the mean capacitance,  $\omega$  the angular frequency,  $\theta$  is the phase angle, and  $h$  is the modulation index. This modulation index is equal to  $d_1 / d_0$ , where  $d_0$  is the average distance between sample and probe tip, and  $d_1$  is the amplitude of the probe's oscillation.

$$V_{ptp} = (\Delta V - V_b)R_f C_0 \omega h \sin(\omega t + \theta) \quad \underline{\text{49}}$$

In a measurement,  $V_b$  is set to a range of potentials so that  $V_{ptp}$  vs.  $V_b$  can be plotted and extrapolated from. An example is shown in Fig. 16, where  $V_{ptp} = 0$  is the point at which we have  $V_b = -V_{CP}$ .

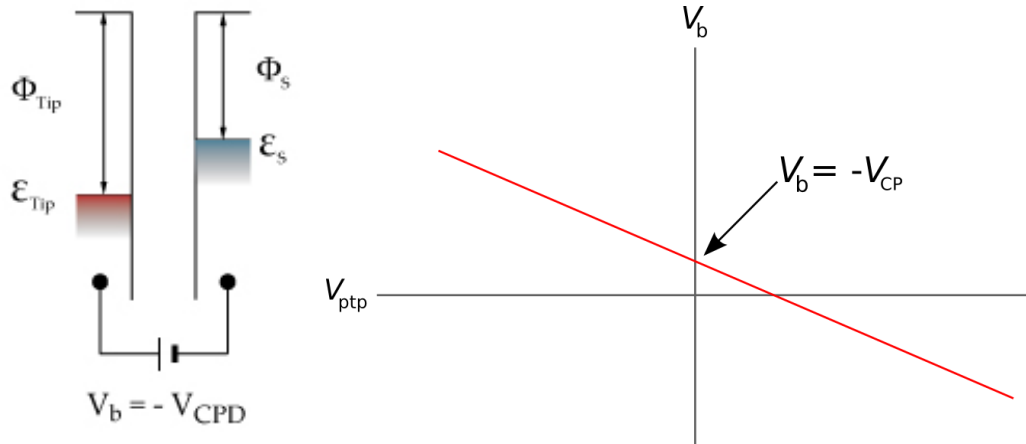


**Figure 16** Kelvin Probe result of  $V_{ptp}$  vs.  $V_b$  measurement, figure adapted from [61]

The probe can move across an area of a sample, measuring  $V_{ptp}$  for a range of  $V_b$  as it oscillates. This results in a scan of the surface and change in work function across the area.

The main advantage of the Kelvin probe is that it is a relatively low-cost instrument, with which taking scans of the surface work function are simple and straightforward. This is in contrast to XPS or ultraviolet photoelectron spectroscopy (UPS) which can also obtain the work function, but the instruments are expensive (typically meaning they are more difficult to obtain time to use the instrument) and complicated to operate (often a technical operator will perform XPS measurements of a sample, instead of the principal researcher).

## 3 Methods

The experimental process I followed is outlined in the next sections. This can be separated into three parts: synthesis of the sample, testing for WOR activity, and study of the structure.

The sample synthesis includes our deposition procedure as well as any measures taken pre-electrodeposition and post-electrodeposition for preparation of the finally tested catalyst material. Measures taken pre-deposition included the cleaning of FTO glass, designating deposition area, and preparation of the electrochemical cell; post-deposition procedure included drying sample, heat treatment, and storage.

Next I outline the parameters of our electrochemical tests of the catalyst materials, i.e. CV and CA, and the methods we used to study the measurements produced in these tests. Finally I will outline the methods I employed to study the physical and electronic structure of the catalyst, including the use of XPS, FESEM, and a Kelvin probe.

## 3.1 Sample synthesis

### 3.1.1 Glass cleaning & preparation

Before electrodeposition, glass coated with fluorine-doped tin oxide (FTO) glass (15 Ω/sq) was cut and cleaned. The glass was obtained from Solaronix with dimensions of 30x30cm and 2.2mm thickness. The glass was cut to smaller sizes of 3x2cm or 3x1cm. As a starting point, 3x2cm glass samples were used (with a surface deposition area of 4cm<sup>2</sup>), however commonly a smaller deposition area is used. Our own experiments confirmed an increase in activity using smaller deposition area so we proceeded to use 3x1 cm glass samples after these tests.

The cut FTO glass was then placed in a 100mL beaker filled with acetone. This beaker was sonicated for 2 minutes before the pieces were extracted, rinsed with Milli-Q water, and dried.

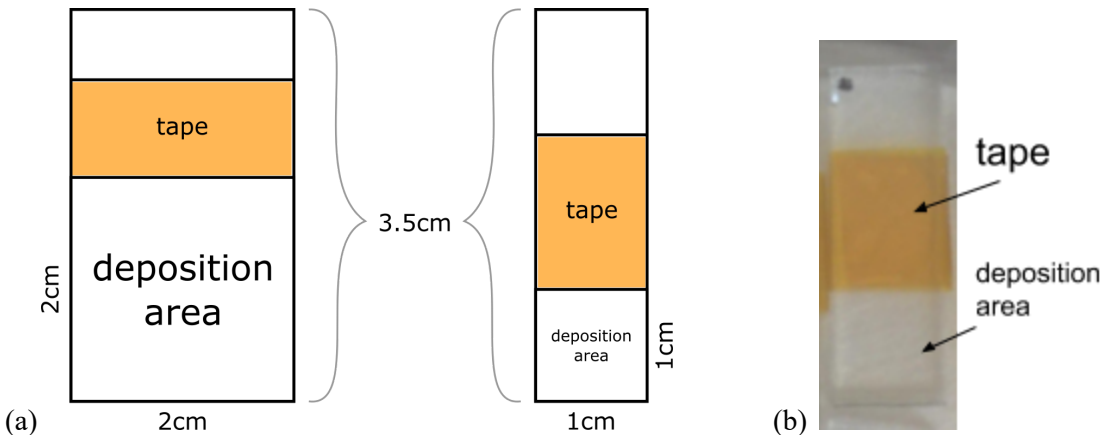


**Figure 17** (a) Representation of the two different deposition areas tested on FTO glass samples. (b) The 3x1cm cleaned FTO glass, with coated side marked at the top of the sample (black dot on left means coated side is up) and tape (yellow) designating a 1cm<sup>2</sup> area at the bottom.

Next, a multimeter was used to determine the coated (i.e. conductive) side of the glass. The conductive side of each piece was marked with a permanent marker. Then, an area of 4cm<sup>2</sup> and 1cm<sup>2</sup> was measured and taped onto the 3x2cm and 3x1cm glass respectively, on the coated side of the glass. A diagram representation of the deposition area on the glass is shown in Fig. 17(a). The final prepared FTO glass electrodes looked as in Fig. 17(b).

### 3.1.2 Electrodeposition of MnO<sub>x</sub>

For deposition of MnO<sub>x</sub> from Mn(VII), the following electrodeposition protocol was followed. I mixed a solution of 1.5 mM KMnO<sub>4</sub>, and for each set of depositions an amount of Fe(NO<sub>3</sub>)<sub>3</sub> was added, corresponding to the desired concentration, from 0.0mM to 1.00mM. The proposed reaction for the deposition of Mn(VII) to MnO<sub>x</sub> occurring at the FTO electrode surface is shown in Eq. 50.

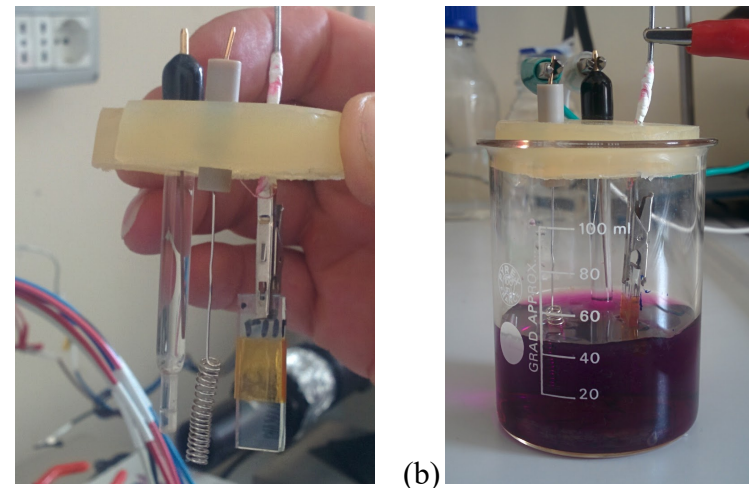
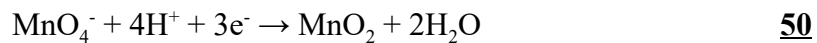


**Figure 18** (a) The reference electrode (Ag/AgCl), Pt counter electrode, and FTO glass working electrode attached to the cap. (b) Cell set-up in electrodeposition solution

The working electrode was prepared FTO glass, the counter electrode was a spiral Pt wire, and the reference electrode was an Ag/AgCl electrode. These electrodes were attached to a cap, as seen in Fig. 18(a). The cap was used to hold the electrodes in the beaker at a consistent depth, and with a consistent distance between electrodes. The cap was then put on a 100mL beaker containing deposition solution, as shown in Fig. 18(b).

The electrodes were attached to a potentiostat which was set to produce a constant current density of -0.250 mA/cm<sup>2</sup>. The potential range was set to -2.5V to 2.5V, and the potentiostat recorded the potential of the cell every 1s. A typical deposition curve is shown in Fig. 19.

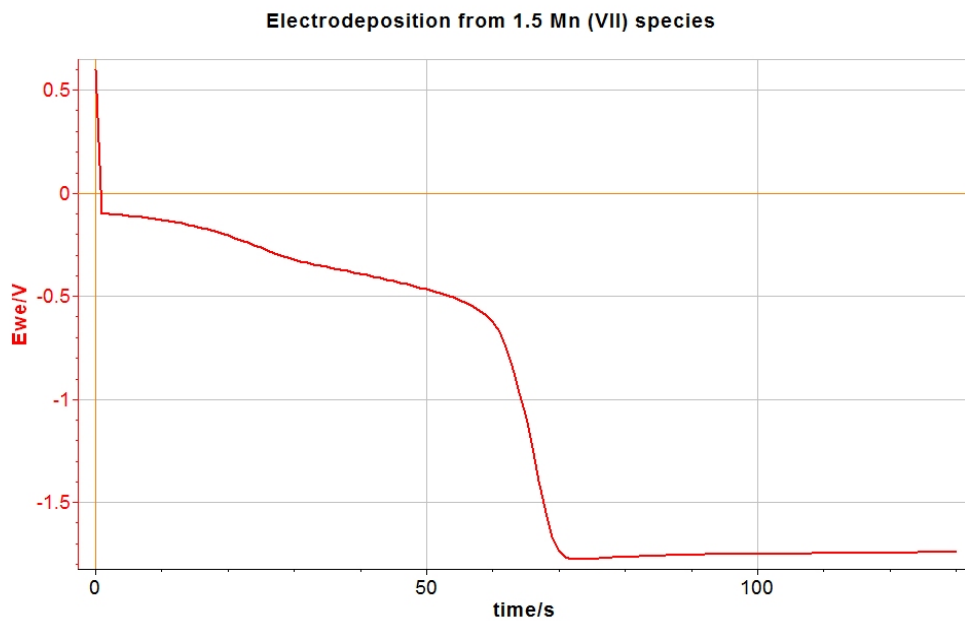


**Figure 19** Example of an electrodeposition curve. This deposition was performed on a 1cm<sup>2</sup> area in 1.5 mM KMnO<sub>4</sub> solution.

Electrodeposition was usually stopped within 10s after the drop in potential was observed, seen around 65s in the example in Fig. 19. This was done because if the deposition was run for longer times, the samples produced could be seen to have varying darkness of colour in different regions on the deposition area of the glass. This demonstrated that the material being produced was less homogenous compared to an evenly-coloured sample, as was produced when stopping the deposition just after the

drop in potential. When the electrodeposition ran for much longer than the time of the drop in potential, the samples produced also were more fragile, with material blowing off when dried by blowing with compressed air.

All electrodepositions and electrochemical testing was run at 298 K using a multichannel VSP potentiostat/galvanostat (BioLogic) with EC-Lab v. 10.44 software.

After deposition was stopped, the sample was removed from the cell and washed with bidistilled water. It was then dried by blowing compressed nitrogen gas onto the surface. Samples were then placed in a standard sample holder to be stored until WOR testing, or taken to be heat treated before storage. After each electrodeposition, the solution in the beaker was changed.

### 3.1.3 Heat treatment

For the samples to be heat treated, tape was removed from the samples after deposition and drying (tape from designation of deposition area, see 3.1.1 *Glass cleaning & preparation*). Samples were then put in an oven with regular airflow and placed inside at 100°C. After 3 hours they were removed and left to cool in a sample dish, and then stored until testing.

## 3.2 Activity testing

### 3.2.1 Electrochemical tests

The solution used for testing each sample was a 0.1M NaPi buffer, mixed using Na<sub>2</sub>HPO<sub>4</sub> and NaH<sub>2</sub>PO<sub>4</sub>. The buffer was checked for a pH of 7 with a standard pH probe. The same

beaker and electrode set up of the cell (see Fig. 18) was used for testing as in electrodeposition, with the buffer solution being used in place of the deposition solution. One complete test included cyclic voltammetry (CV) and multi-step chronoamperometry (CA) protocols outlined below. The same buffer solution was used for two complete tests before the solution was changed.

For each cycle in the CV, potential range was 0.800V to 1.300V, changing at a rate of 20mV/s. Five cycles were performed in each test, and the current was recorded for every 0.1s. In the CA, potential was stepped from 1.00V to 1.25V in 0.025V increments. Potential was held constant for 120s for each step from 1.00V to 1.125V. For steps from 1.150 to 1.225, the duration of each step was 180s. At 1.25V, potential was held constant for 240s. For all steps the current was recorded at 100 ms resolution and averaged over every 0.1s.

### 3.2.2 Electrochemical analysis

For comparison of the WOR activity across many samples, we used the peak current density from the final step of the CA test ( $J_{1.25V}$ ). See Fig. 20 for an example of how the value from CA translates to the concentration vs current density plot.

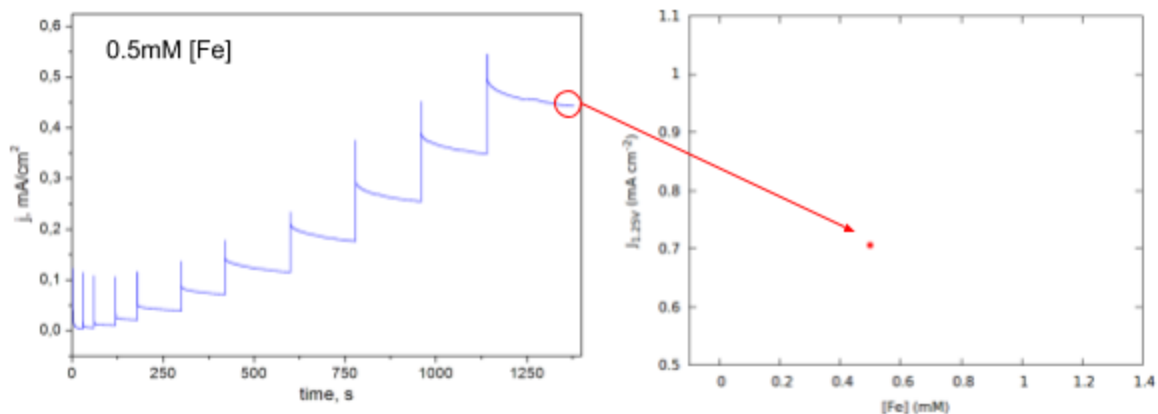


**Figure 20** Example of taking the  $J_{1.25V}$  from CA to compare against other values for different concentrations of Fe(III) (denoted here as [Fe]).

Standard error of mean for the results of  $J$  vs. [Fe] are shown in the respective plots. In some cases, standard deviation is shown and this is denoted in the figure caption. Standard error reports an estimate of how precise the sample mean is with regards to the true mean, while standard deviation of the sample is a measure of the degree to which points in the sample will differ from the mean. The standard deviation describes the degree of variation in the results, while the standard error provides a description of the accuracy of measurements provided by the sample size.

Tafel plots shown in the Results chapter were taken from the last points of each step of the CA test of each sample. These points were plotted against  $\log(J)$ . Where the plots are linear, there is no mass transfer limitation in that potential/current region, and this is what is referred to as a Tafel slope.

### 3.3 Structural characterization

Fe [mM]	0	0.10	0.25	0.35	0.50	1.00	blank FTO
FESEM	✓		✓			✓	✓
XPS	✓(2)		✓(2)	✓(2)		✓(2)	✓
HR O1s / Mn2p <sub>3/2</sub>	✓	✓	✓	✓			
HR C1s	✓	✓	✓	✓			✓
Kelvin probe	✓(3)	✓(4)	✓(4)	✓(3)	✓	✓(2)	✓

**Table 1** Types of measurements taken by each method. Numbers in parentheses are number of different samples at that concentration (at least one measurement of each sample using that respective method). No number in parenthesis means one sample was used.

Samples from each different deposition solution were characterized using XPS for elemental analysis, FESEM for structural/morphological analysis, and Kelvin probe for work function analysis. Samples from the following deposition solutions where tested using each method:

**XPS details:** XPS elemental analysis surveys (pass energy: 187.85 eV) were performed on one heat treated and one non-heat treated sample from deposition solutions as listed in Table 1. High resolution (HR, pass energy: 23.5 eV) O1s, Mn2p{3/2}, and C1s spectra were measured for samples from depositions solutions with 0 - 0.35 mM Fe(NO<sub>3</sub>)<sub>3</sub>. HR C1s spectra was obtained for the blank FTO sample as well. Measurements were done using a beam size of 100 μm with a PHI 5000 Veraprobe Scanning X-ray Photoelectron Spectrometer (monochromatic Al Kα x-ray source with 1486.6 eV energy). Multipak 9.6 software was used for fitting procedure and deconvolution analyses with core level peak energy reference to C1 peak at 284.5 eV (C-C/C-H sp<sub>2</sub> bonds).

**FESEM details:** FESEM images were obtained for one non-heat treated sample each. Images were taken at one point in the middle and at one point on the edge of each sample, at magnifications of 50.00 kx and 350.00 kx. The instrument used was a Zeiss Merlin microscope equipped with a Gemini II column. Due to the thinness of the films being measured, a low acceleration voltage of 3 kV was used to limit the depth of the investigation region.

# 4 Results and discussion

In this chapter I will present the results of my experiments and discuss them in the context of their implications on the catalytic activity for WOR. To do this I have divided the results into those gathered from electrochemical experiments, results from physically probing the structure, and computational results.

In some cases, the results reported are preliminary experiments that were performed to determine whether prospective techniques or adjustments were promising avenues to explore. Some of these attempts resulted in materials with very low current density during WOR testing, or with no material being deposited at all, however I am reporting them here for completeness.

## 4.1 Electrochemical results

First I report on results involving the optimization of the electrodeposition procedure, and electrochemical testing of the produced Fe-MnO<sub>x</sub> catalyst material.

## 4.1.1 Electrocatalyst synthesis protocol

The following section reports on my exploration of the protocol for electrodeposition and preparation of the catalyst in question. I studied various aspects of the electrodeposition including potentiostat settings, deposition time, and concentration levels of the deposition solution. I also studied the effect of heat treatment as part of the preparation for the material testing.

### 4.1.1.1 Constant potential vs. constant current depositions

Typically, electrodeposition is performed with a constant current. In Fig. 21(a) we show a deposition curve of potential vs. time for a constant current (CC) deposition and a constant potential (CP) deposition for comparison. In Fig. 21(b) is the same deposition showing the curve of current vs. time. Both depositions were done in solutions of 1.5 mM KMnO<sub>4</sub> + 0.5 mM Fe(NO<sub>3</sub>)<sub>3</sub>.

The constant current deposition was set to achieve a -0.25mA/cm<sup>2</sup> current density, e.g. the current is set to -1.0 mA to achieve a -0.25 mA/cm<sup>2</sup> current density on an electrode with a 4.0 cm<sup>2</sup> deposition area.<sup>4</sup>

The constant potential was set to -1.6 V. This value was chosen because in our constant current depositions, the normal behaviour was to see the potential reach a certain plateau value, and this plateau potential was around -1.6 V.

---

<sup>4</sup> This parameter we set this way for all deposition experiments unless otherwise specified.

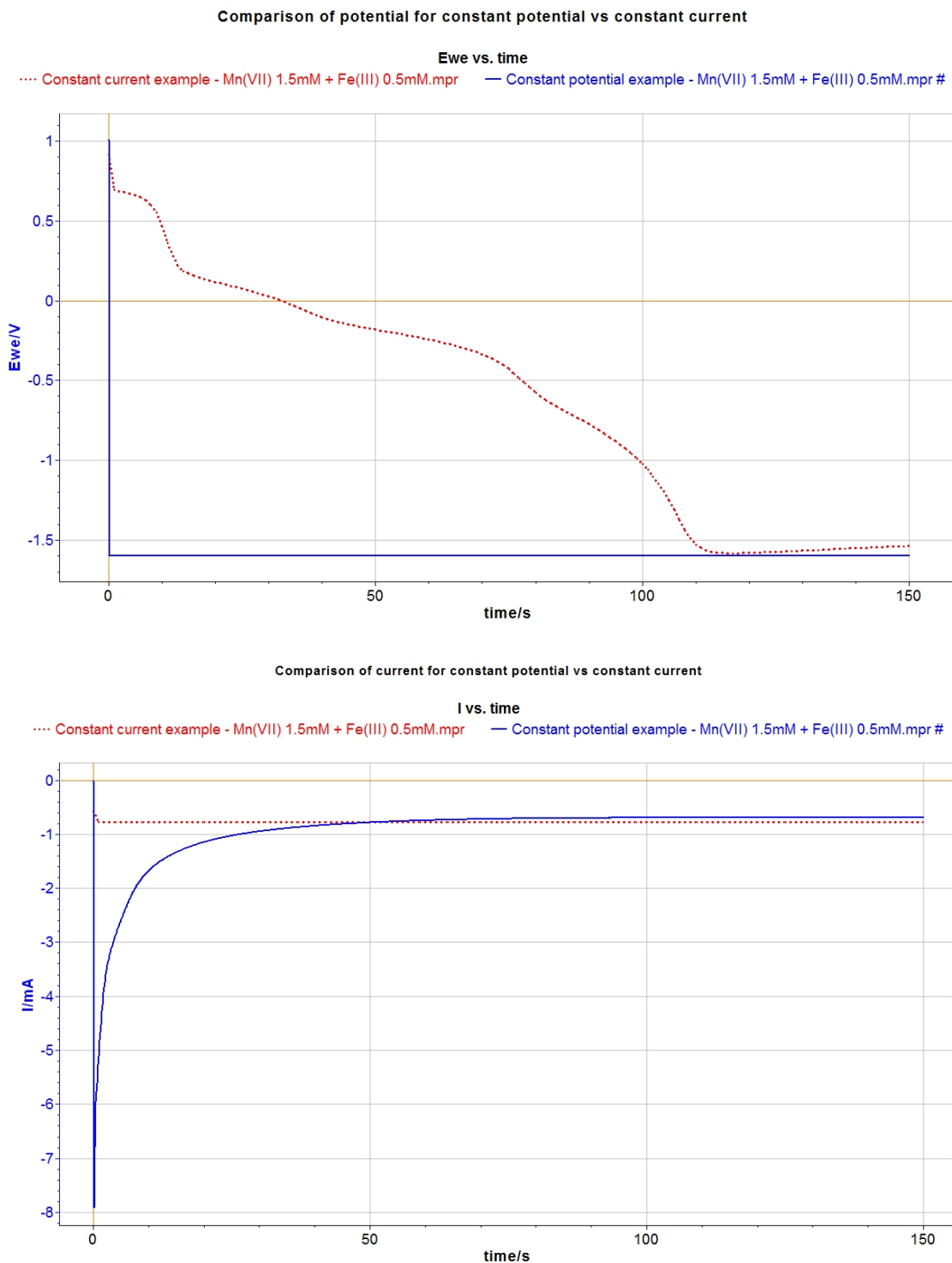


**Figure 21** Depositing at a constant potential (solid) compared to a typical constant current deposition (dotted). (a) The potential in the CC deposition reaches a similar plateau value to the constant set potential for the CP deposition. (b) The current in the CP deposition reaches a similar plateau value to the constant set current for the CC deposition,

In the CP deposition (solid), we saw the current rapidly reaching the value of the current we see in a typical constant current deposition (dotted). As expected, in the CA deposition we saw the potential reach a plateau value around the same value we set for the constant in the CP deposition.

The Tafel from testing WOR is shown in Fig. 22. The results show a lower peak current density  $J_{1.25V}$  for the sample deposited with constant potential (squares). The star and triangle data points of samples from typical constant current depositions, give a higher current at all potentials above 1.10 V.

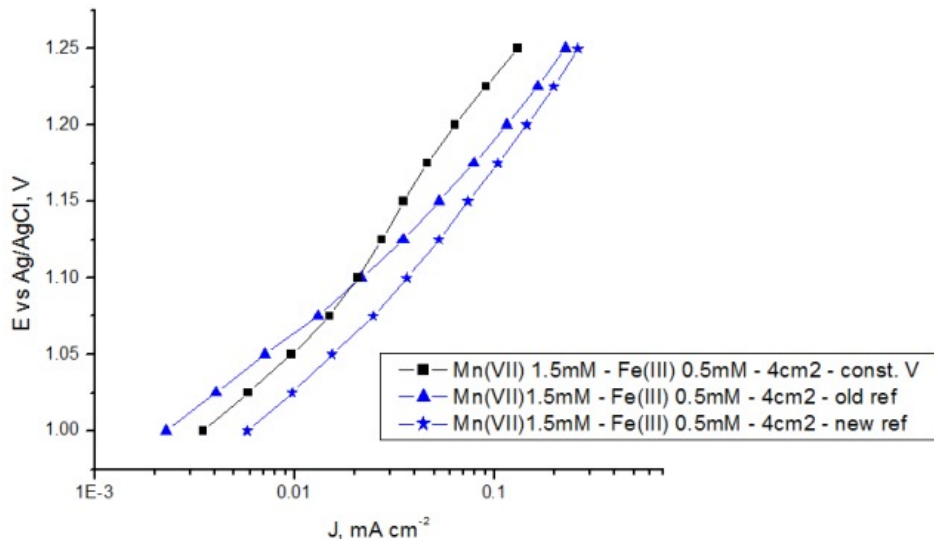


**Figure 22** Tafel plots of the testing from samples of CP and CC depositions. The samples from CC depositions (triangles, stars) show higher current density than the material deposited in CP (squares).

#### 4.1.1.2 Deposition time

In Fig. 23 we see the curves of three different samples being deposited from the same solution batch (solutions were typically prepared in 250mL volumes, with  $\sim$ 60mL

being used for each deposition). The first deposition (black curve) was performed until after a large drop was seen in the measured potential. The second deposition (blue curve) was stopped just before the drop point, and the third deposition (red curve) was stopped midway between the beginning and the predicted drop in potential.

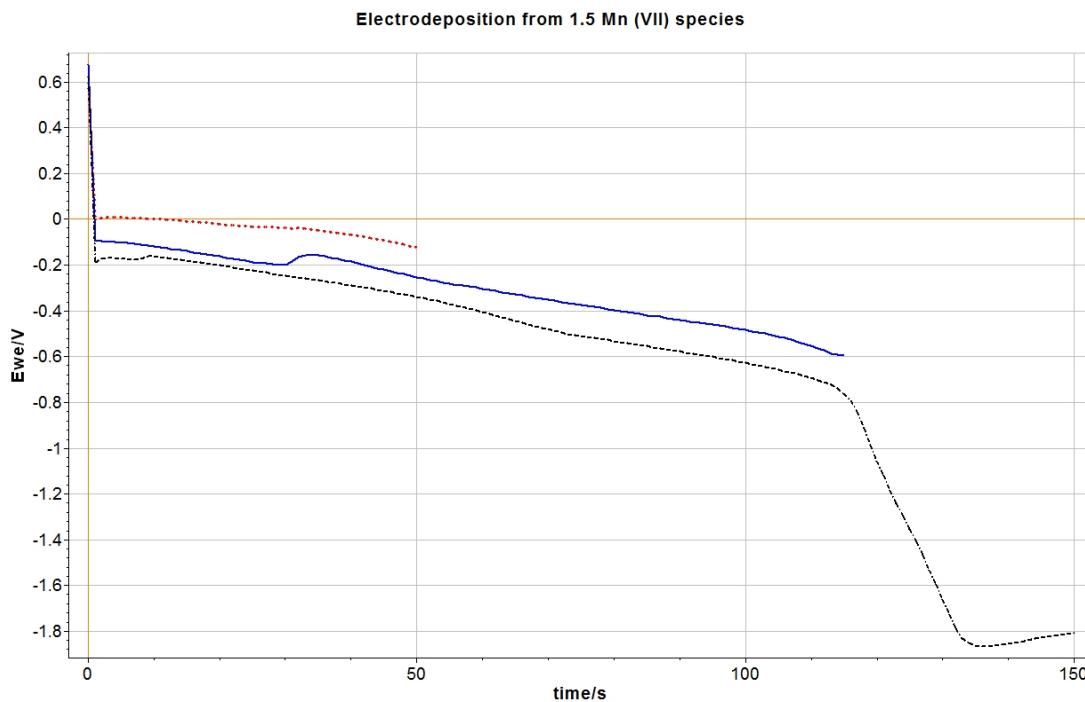


**Figure 23** Deposition curves stopping at different times.

In Fig. 24 we can see that when the deposition was stopped *at or before* the large potential drop (top two curves, blue and red), a lower current was produced overall in the CA tests compared to the sample stopped *after* the drop in potential (bottom curve, black). The sample that was stopped well before the drop shows a significantly lower current than the other two, at the peak potential step in the CA test this sample produces a current that is 0.15mA lower than the sample which was stopped after the potential drop in deposition.

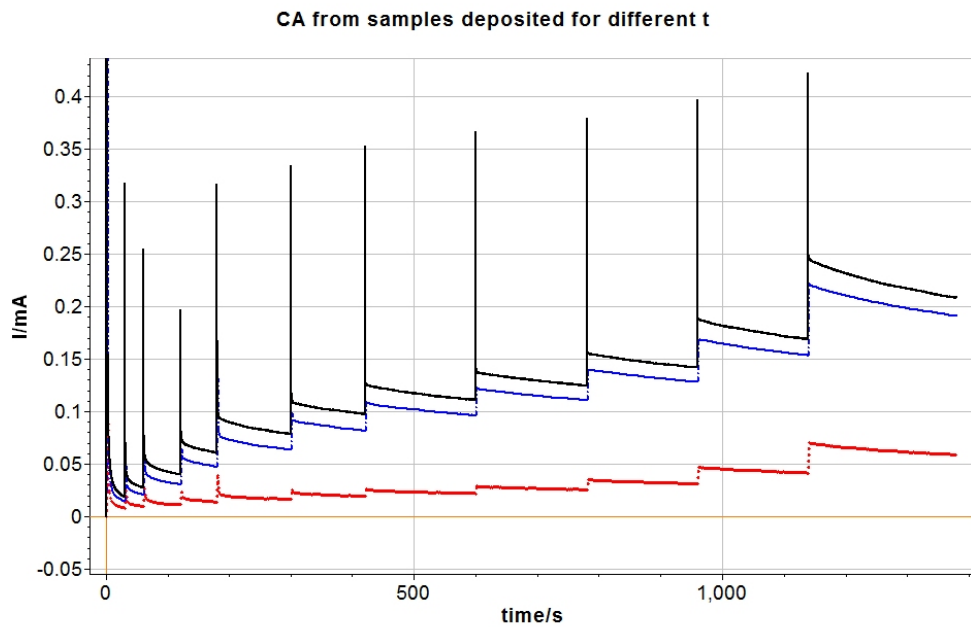


**Figure 24** CA results for samples with deposition stopped at different times. Colours are representative of the deposition curve in Fig. 23.

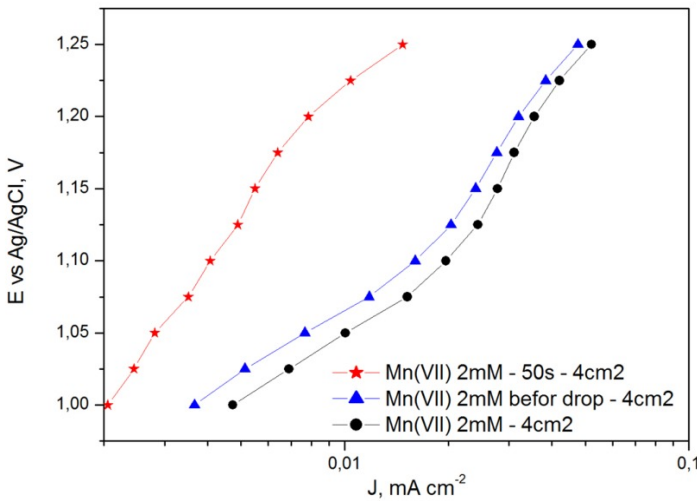


**Figure 25** Tafel plots from samples stopped at different times, deposited in same solution

This result is explored in the Tafel plots in Fig. 25, showing a different curve behaviour in the red curve compared to the blue and black. Since the slope is lower in the

straight portion (Tafel slope) of the blue and black curves, this indicates better activity of the reaction.

#### 4.1.1.3 Concentration regimes

Samples were made in two different concentration regimes and tested. The low concentration regime included solutions of 1.5 mM KMnO<sub>4</sub> and 0.5, 1.0, and 1.5 mM Fe(NO<sub>3</sub>)<sub>3</sub>. The high concentration regime consisted of 30 mM KMnO<sub>4</sub> and 10, 20, and 30 mM Fe(NO<sub>3</sub>)<sub>3</sub>. The depositions of all 6 is shown in Fig. 26, where the three plateau curves at the top of the figure (solid lines) are depositions from the high concentration regime solutions, and the three curves showing a much larger change in potential are deposited from solutions in the low concentration regime (dotted lines).

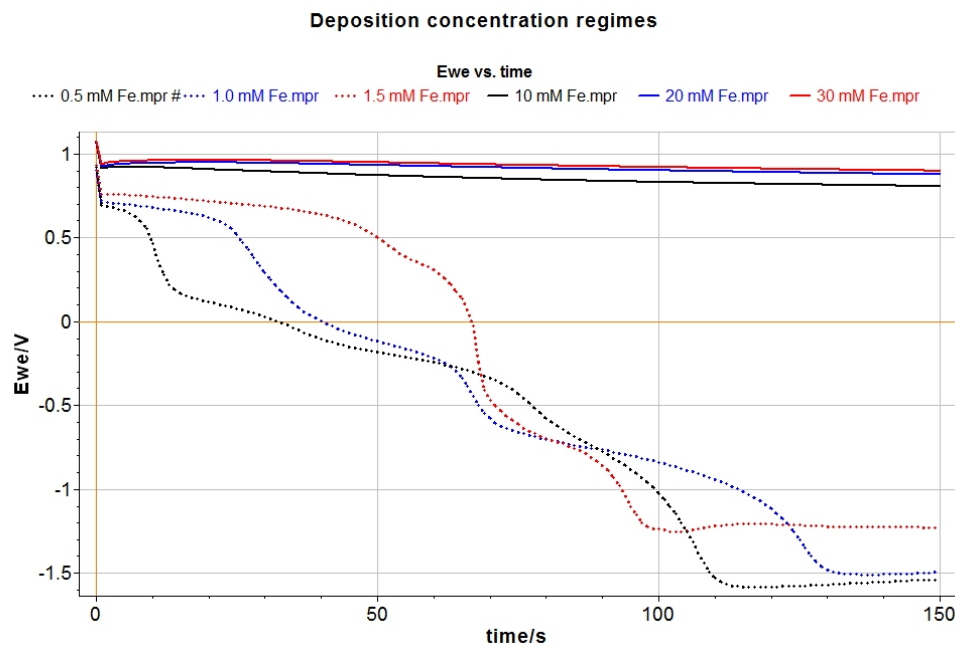


**Figure 26** Depositions of samples made in different concentration regimes of KMnO<sub>4</sub> and Fe(NO<sub>3</sub>)<sub>3</sub> solutions. Solid curves at the top of the figure showing plateau behaviour are in the high concentration regime, dotted curves are depositions from the low concentration regime.

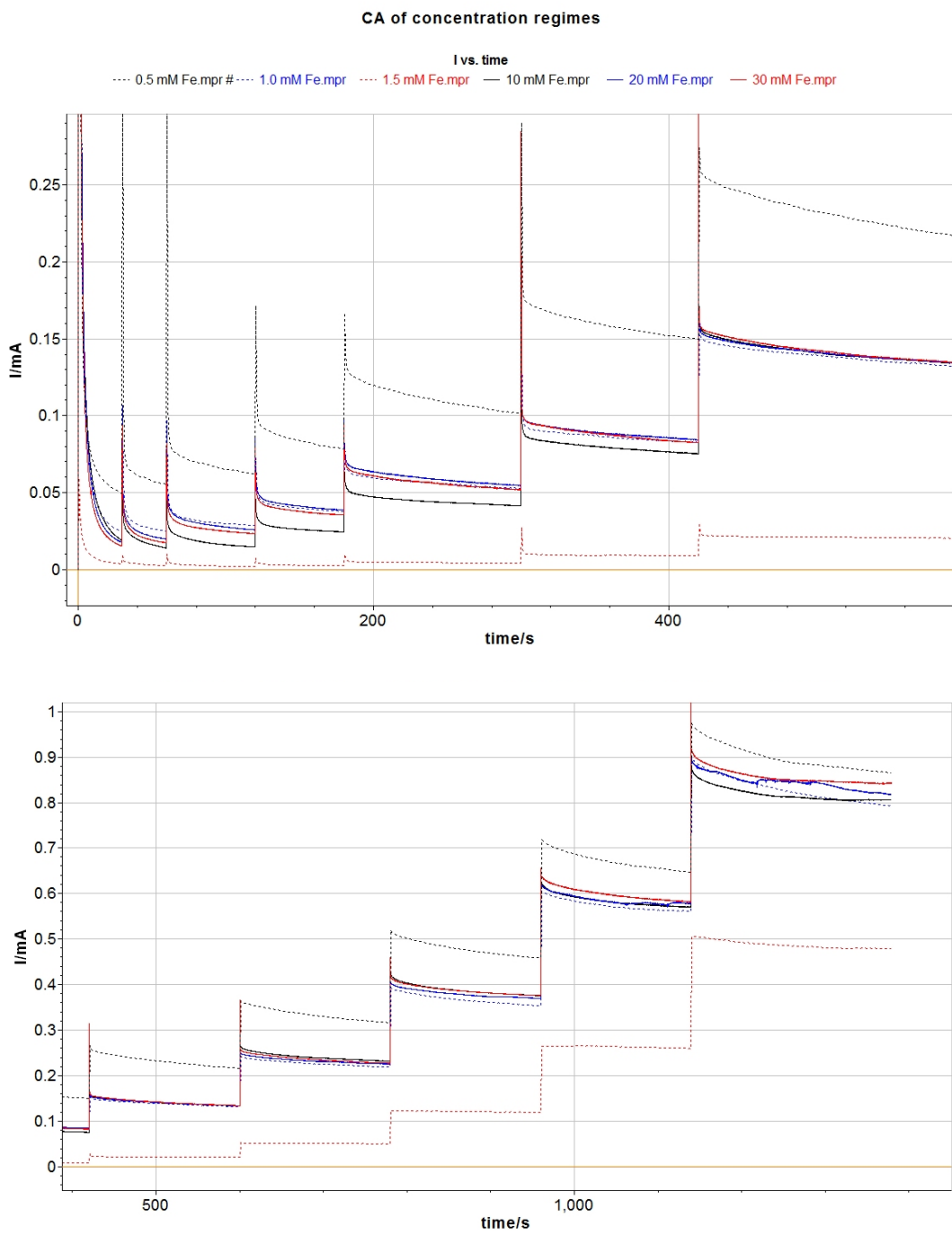


**Figure 27** CA of samples made in the two different concentration regimes of KMnO<sub>4</sub> and Fe(NO<sub>3</sub>)<sub>3</sub> solutions. The top shows the results at the beginning of CA testing until ~600s, and the bottom shows the remaining steps from 500s to the end of the experiment. Each step represents 0.025V, starting from 1.00V and finishing at 1.25V.

CA done for these two concentration regimes is shown in Fig. 27. At every potential step, the low regime gives higher current than the samples deposited from the equivalent ratio high regime solutions, except for the case where the KMnO<sub>4</sub> and Fe(NO<sub>3</sub>)<sub>3</sub> concentrations in solution are the same. The sample from the 1.5 mM KMnO<sub>4</sub> and 1.5 mM Fe(NO<sub>3</sub>)<sub>3</sub> deposition solution has a much lower current than all other samples. The highest current at every step is given from the sample deposited in 1.5 mM KMnO<sub>4</sub> and 0.5 mM Fe(NO<sub>3</sub>)<sub>3</sub>. The sample from the high regime with the equivalent ratio is 30 mM KMnO<sub>4</sub> and 10 mM Fe(NO<sub>3</sub>)<sub>3</sub>, which shows currents around 0.1mA lower than the sample with the highest current.

Tafel plots for the low regime are shown in Fig. 28(a) and for the high regime in Fig. 28(b). The Tafel plots for high regime samples show very similar characteristics and current, especially after the 1.10V step. In the low regime (Fig. 28(a)) the Tafel plots are much less similar to one another. However, in both figures the curves for the samples with equivalent concentrations of KMnO<sub>4</sub> and Fe(NO<sub>3</sub>)<sub>3</sub> (i.e. 1.5 mM KMnO<sub>4</sub> with 1.5 mM Fe(NO<sub>3</sub>)<sub>3</sub>, and 30 mM KMnO<sub>4</sub> with 30 mM Fe(NO<sub>3</sub>)<sub>3</sub>) have similar behaviour at the low potential steps, giving higher current for the first step at 1.00V than at 1.025 and 1.05V.

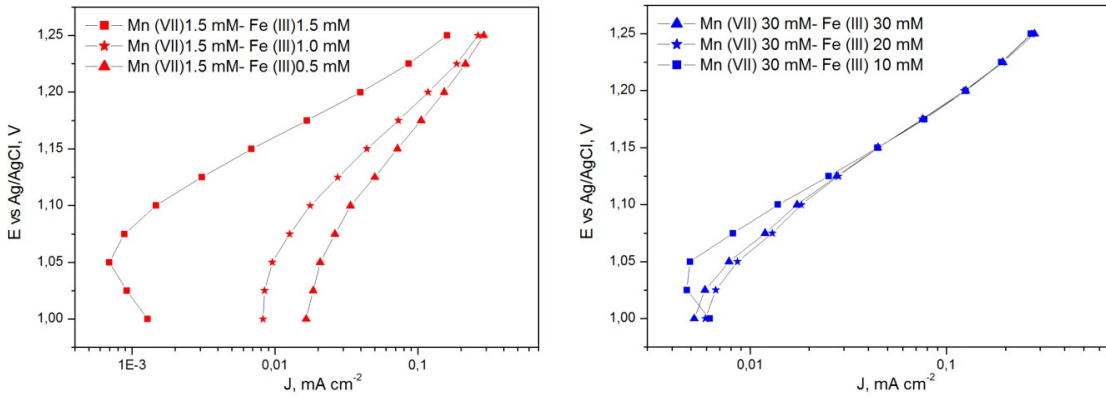


**Figure 28** (left) Tafel slopes of samples made in the low regime solutions and (right) results of samples made in the high regime solutions.

#### 4.1.1.4 High concentration, long time depositions

Depositions were also performed in the high concentration regime without being stopped until long after the large drop in potential. These curves can be seen in Fig. 29, with deposition times of 150s (2.5min, black, dashed line), 600s (10min, red, dotted line), and 1800s (30min, blue, solid line).

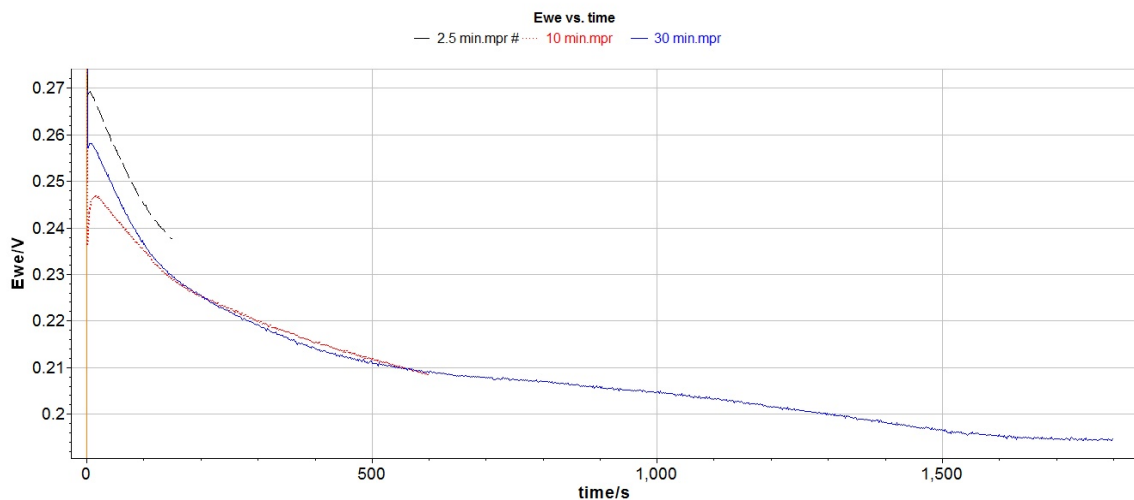


**Figure 29** Depositions at long times compared to the typical deposition timescale of 2 - 2.5 min

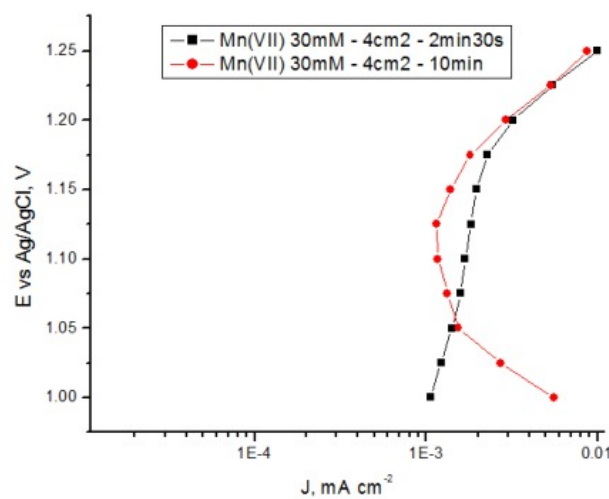


**Figure 30** Tafel plot from sample deposited at long time vs. typical deposition time

The results testing the samples with high concentration and long time depositions can be seen in Fig. 30, showing Tafel plots for the 2.5 min and 10 min deposition samples. The 10min deposition sample (red) is not as active as the 2.5min sample (red), and both produce current densities less than a typical low concentration regime sample. The 30min deposition sample is not shown because the layers produced were so fragile that the material was blown off of the FTO glass when drying with compressed air.

#### 4.1.1.5 Size of deposition area

A small size deposition area (surface area < 1cm<sup>2</sup>) is commonly used across the literature for electrodeposited catalyst materials for WOR. I began performing experiments using a 4cm<sup>2</sup> deposition area on 3x2cm FTO glass, however since this is quite a large electrode surface area compared to what is typical in the literature, we decided to compare with 1cm<sup>2</sup> deposition area on 3x1cm FTO glass, as demonstrated in the Experimental Methods chapter, Fig. 17. Deposition curves showing an example of reproducibility of 1cm<sup>2</sup> deposition area samples are in Fig. 31(a). The reproducibility of CA testing for these samples is shown in the Tafel plots of Fig. 31(b).

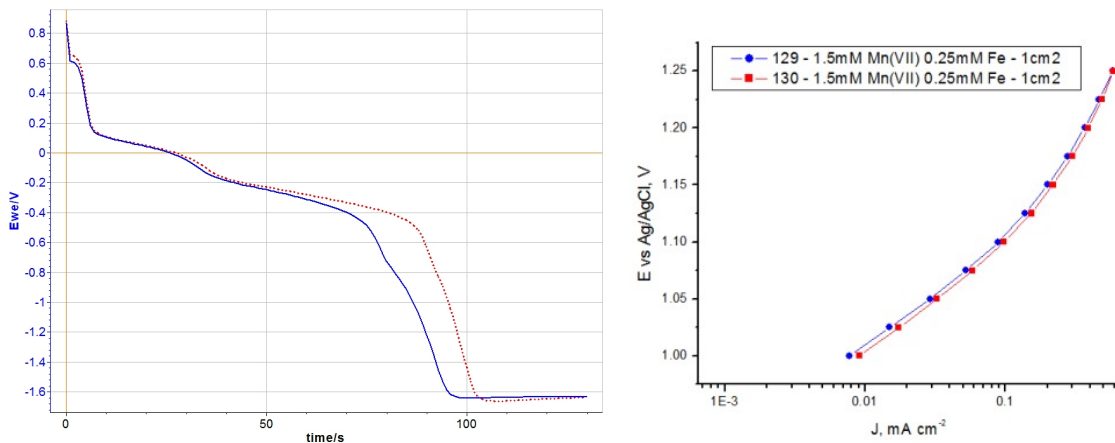


**Figure 31** Deposition of two small area samples from same solution batch. In (a) we are

demonstrating the reproducibility of the deposition curve, and in (b) the reproducibility of the Tafel slope gained from CA testing.

Tafel plots comparing samples with the different deposition areas are shown in Fig. 32. The samples with a 1cm<sup>2</sup> deposition area (blue) show similar Tafel slopes and have the same peak current density, which is an order of magnitude higher than the current density of the samples deposited on a 4cm<sup>2</sup> area (black).

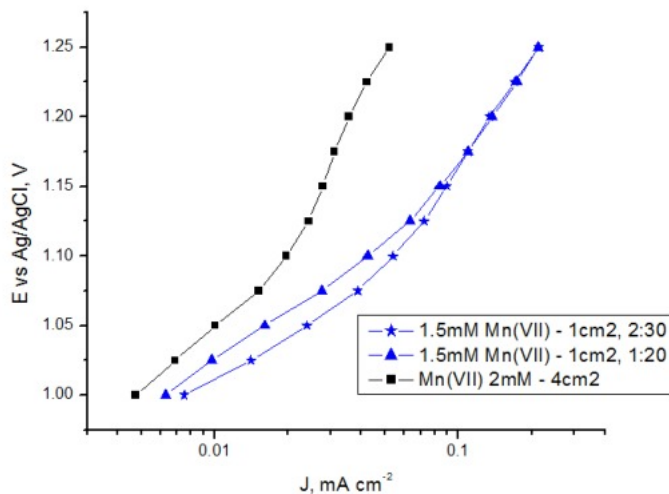


**Figure 32** Testing results from samples deposited on different areas.

#### 4.1.1.6 Heat treatment<sup>5</sup>

After deposition, a selection of samples were heat treated before testing with CV and CA. These samples were compared to the tests of the non-heat treated samples. Fig. 33 shows the Tafel plots from testing a set of non-heat treated samples. The sample with no Fe in the deposition solution (red curve) has the lowest current density of all samples at 1.15 to 1.25V. However, the curves have similar slopes at lower potentials from 1.00 to 1.05V.

<sup>5</sup> All results referenced from this section onward used 1cm<sup>2</sup> deposition areas.

The Tafel curves do not show consistent slope behaviour.

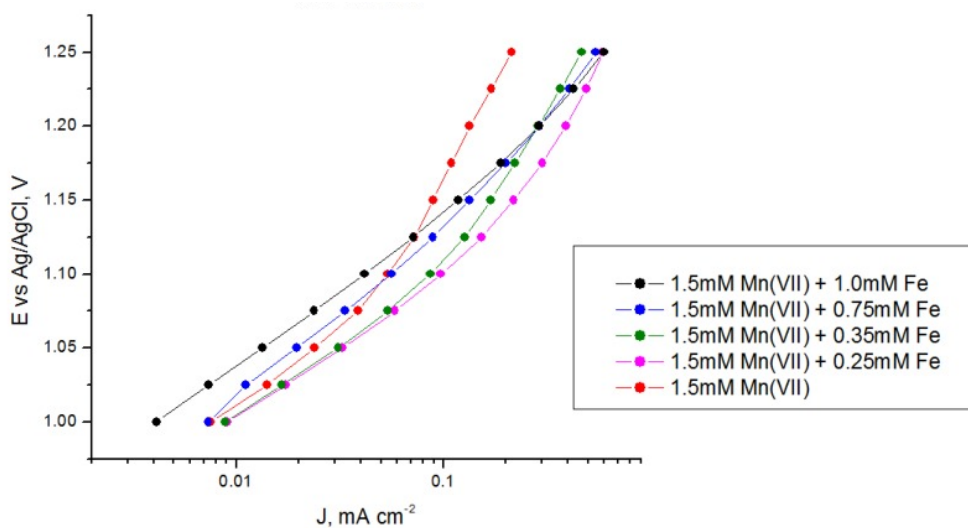


**Figure 33** Tafel plot of results from non-heat treated samples at every concentration

In Fig. 34 we see the Tafel plots of a set of heat treated samples with varying concentrations of Fe in the deposition solution. The curves here are much more consistent in slope, e.g. the green curve (1.5 mM Mn + 0.35 mM Fe) shows a consistently higher current density than the fuschia curve (1.5 mM Mn + 0.25 mM Fe) and consistently lower current density than the red curve (1.5 mM Mn). The Tafel curves in Fig. 34 have similar slopes for samples with 0 - 0.35 mM Fe, but those with larger amounts of Fe in the deposition solution show lower current densities and different characteristic curves.

In Fig. 35 we compare the current densities of heat treated vs. non-heat treated samples deposited from different concentrations of Fe(NO<sub>3</sub>)<sub>3</sub> in solution. The points in the plot are averages over all samples deposited with that specific Fe(NO<sub>3</sub>)<sub>3</sub> concentration. The heat treated samples show a consistently higher current density than the non-heat treated samples at every concentration, except for the highest 1.25 mM Fe concentration.

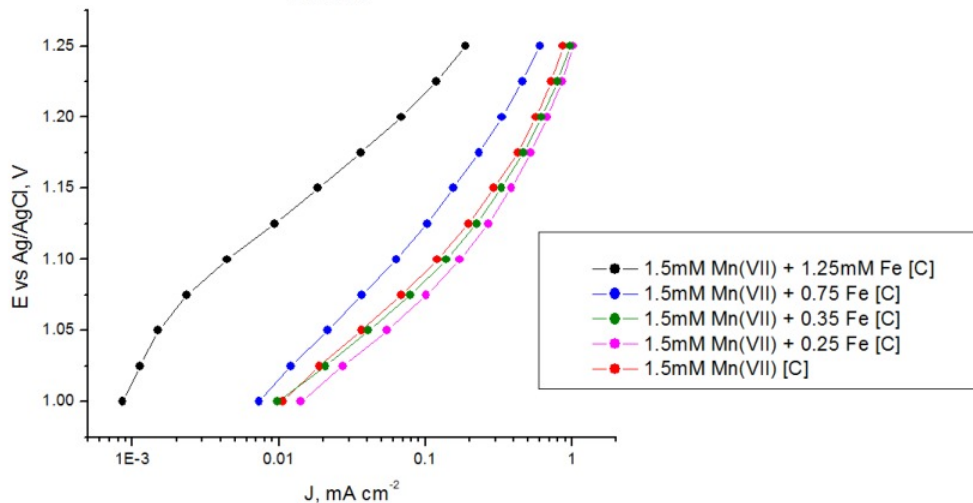


**Figure 34** Tafel plot of results from heat treated samples at every concentration.

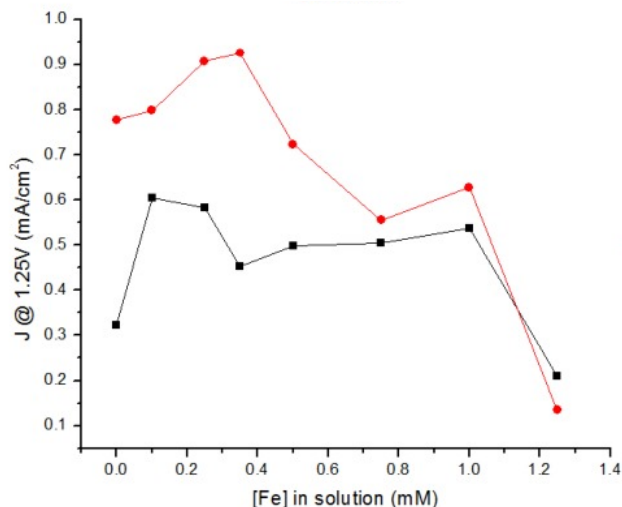


**Figure 35** Comparison of the activity of heat treated and non heat treated samples. In red (circles) is the peak CA value of heat-treated samples at each concentration of Fe(III) in solution with SD = 0.305 and SE = 0.064. In black (squares) are samples deposited from the same concentrations in solution, but non-heat treated, with SD = 0.312 and SE = 0.058 .

#### 4.1.2 Adding metals to deposition solution

We decided to explore doping the MnO<sub>x</sub> material with other metals to see if the would increase the performance. This has been seen in literature in the improvement of electroconductivity of catalysts and increase in active sites when the dopant disrupts the ordered structure of the catalyst material. We chose Ca, Ru, and Fe to explore because of Ca's role in the photocatalyst complex for WOR in nature, Ru because of its well-known enhancement of the performance of this reaction, and Fe because of promising studies showing its doping of Ni and Co-based electrocatalyst for WOR.

#### 4.1.2.1 Calcium

Depositions were performed Ca(NO<sub>3</sub>)<sub>2</sub> and CaCl<sub>2</sub> salts instead of Fe(NO<sub>3</sub>)<sub>3</sub>. The resulting current density at 1.25V can be seen in Fig. 36 for samples from the different Ca(II)-containing solutions, as well as compared to a sample deposited from only KMnO<sub>4</sub>.

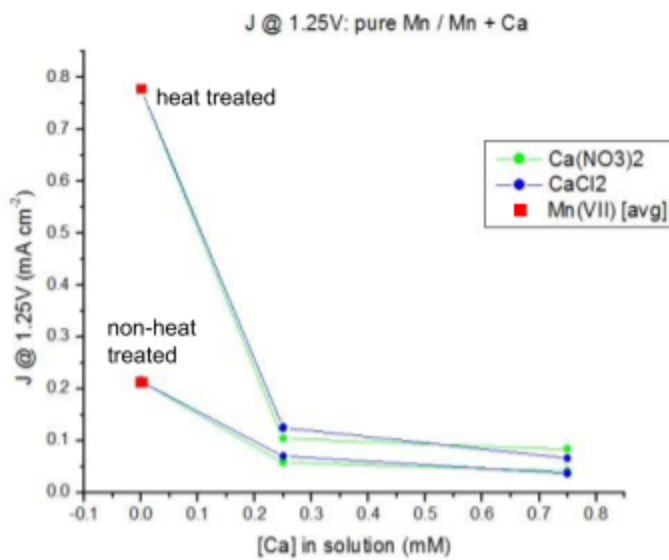


**Figure 36** Tests of samples deposited from KMnO<sub>4</sub> with Ca(NO<sub>3</sub>)<sub>2</sub> and CaCl<sub>2</sub>.

#### 4.1.2.2 Ruthenium

Since RuO<sub>2</sub> is widely considered the standard for WOR electrocatalysts, we decided to try to incorporate a small amount of ruthenium to the MnO<sub>x</sub> electrodeposited catalyst. While electrodepositions were attempted using a solution of 1.5mM KMnO<sub>4</sub> and varying concentrations of RuCl<sub>2</sub> (0.25, 0.5, and 1.0mM), the solution was ultimately found to form a precipitate which did not allow for electrodeposition of any material on the FTO.

#### 4.1.2.3 Iron

The Tafel plot behaviour in Fig. 37 shows the results for a sample each of the different Fe(NO<sub>3</sub>)<sub>3</sub> concentrations that were studied, from 0.00 mM to 1.00 mM. All samples were heat treated. Concentrations from 0.25 mM to 0.75 mM show similar Tafel slopes, while the the 0.00 mM and 1.00 mM samples have a different slope behaviour. The sample from a deposition concentration of 0.00 mM Fe(NO<sub>3</sub>)<sub>3</sub> shows a steep Tafel slope, which is characteristic of a subpar catalyst.

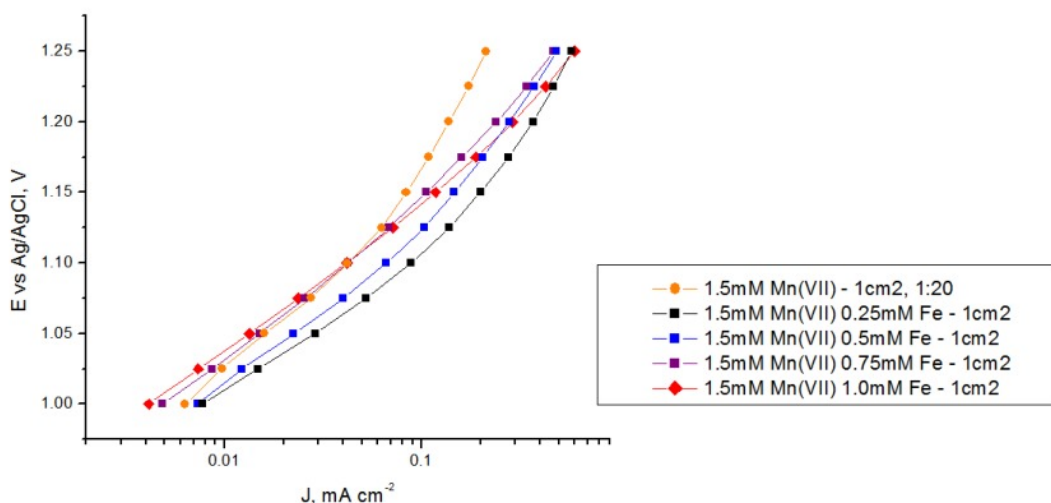


**Figure 37** Tafel plot comparison for samples where different concentrations of Fe(NO<sub>3</sub>)<sub>3</sub> were used in deposition

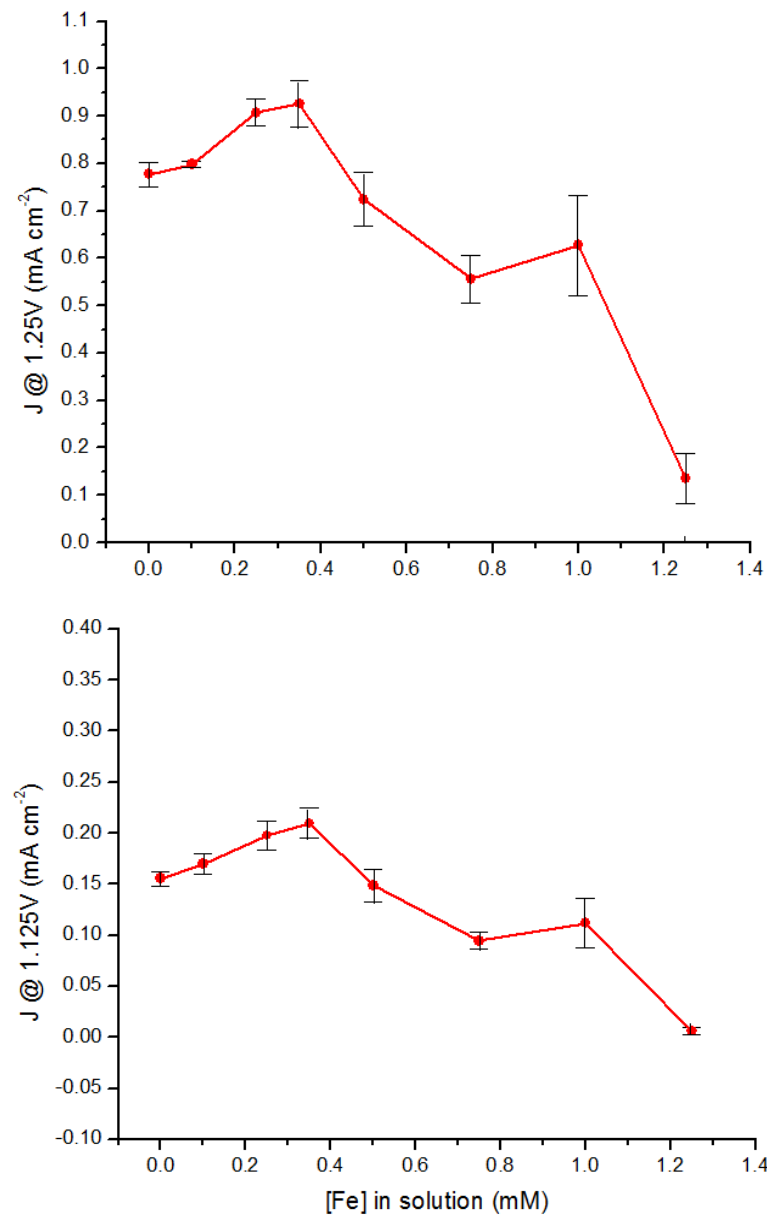


**Figure 38** CA measurement of sample at 1.25V step (top) and 1.125V step (bottom) showing a similar trend across samples of different Fe(III) species in deposition solution. Error bars show variance since the number of samples represented here is small.

As I began testing of many concentrations of Fe(III) species in solution, the decision was made to monitor the trend at the peak CA step of 1.25V. In Fig. 38 I show some preliminary results between the 1.125V and 1.25V steps across different Fe(NO<sub>3</sub>)<sub>3</sub> concentration in the deposition solution. The trend is similar between these steps, but more pronounced in the case of the 1.25V step.

In Fig. 39 we report the final activity results of all heat treated samples with different Fe(NO<sub>3</sub>)<sub>3</sub> concentrations. The red plot shows the average current density at 1.25V across all samples at each concentration, with the highest and lowest reported current density displayed by the grey bars.

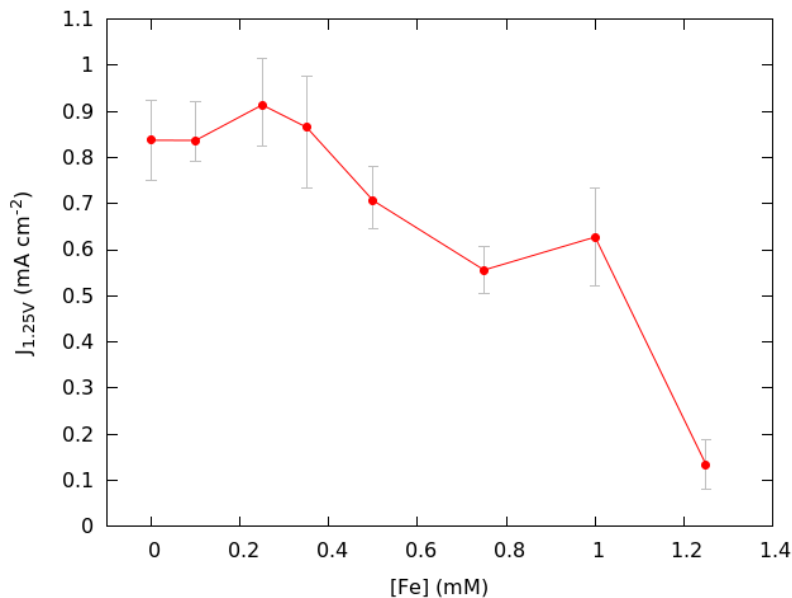


**Figure 39** Results of all heat treated samples deposited from every concentration of Fe(NO<sub>3</sub>)<sub>3</sub>.

The bars represent the variance in values.

The peak in activity is at 0.25 mM Fe(NO<sub>3</sub>)<sub>3</sub>, with an average  $J_{1.25V}$  (current density at 1.25V) of 1.015 mA/cm<sup>2</sup>. This is 0.040 mA/cm<sup>2</sup> higher than the average  $J_{1.25V}$  of the 0.35mM sample. Adding a small amount of Fe(NO<sub>3</sub>)<sub>3</sub> (0.10 mM to 0.35 mM) to the solution results in a highly more active sample than using larger concentrations of Fe(NO<sub>3</sub>)<sub>3</sub> (0.5mM and above). When samples are deposited from a solution with 1.25mM

Fe(NO<sub>3</sub>)<sub>3</sub>, the J<sub>1.25V</sub> is very low; on average 0.188 mA/cm<sup>2</sup>, which is much lower than samples from a deposition solution with only KMnO<sub>4</sub> (no Fe(NO<sub>3</sub>)<sub>3</sub>) present.

#### 4.1.3 Discussion of electrochemical results

The results we found related to establishing our methodology are supported in various areas of literature as well as testing we performed ourselves. A constant current (CC) electrodeposition was found to give a material with better activity for WOR (as compared to constant potential (CP) electrodeposition), and is the standard protocol for electrodeposition of materials. This could be because the potential at the beginning of a CC electrodeposition starts higher and tapers toward a plateau, so as the deposition goes on the potential gets slightly lower as the electrodeposited material aids in lowering the energy barrier for molecules to adsorb to the electrode from solution. In CP electrodeposition we see the current rapidly reach the same current value as that set in constant current electrodeposition. As we know from many studies [8], [17], [24], [26]–[29], in general a more amorphous material displaying long-range disorder is a better WOR catalysis, so we postulate that an electrodeposition at constant potential may drive deposition of a more highly structured material, since the reaction has access to a high (negative) potential throughout the deposition. In constant current deposition, the material may be depositing in a more disordered manner, e.g. depositing on top of already formed oxides.

We believe the deposition time correlates to the complete coverage of the FTO surface, before deposition of more material on top of (Fe-)MnO<sub>x</sub> already deposited. This is because of the significant negative increase in potential shown after an approach to plateau in each deposition, which we theorize is the potential needed to deposit material on the electrode already covered. This can also be supported by FESEM images taken by a collaborator, where an image taken of material where electrodeposition was stopped immediately after the potential drop (Fig. 40(a)) can be compared with an image taken

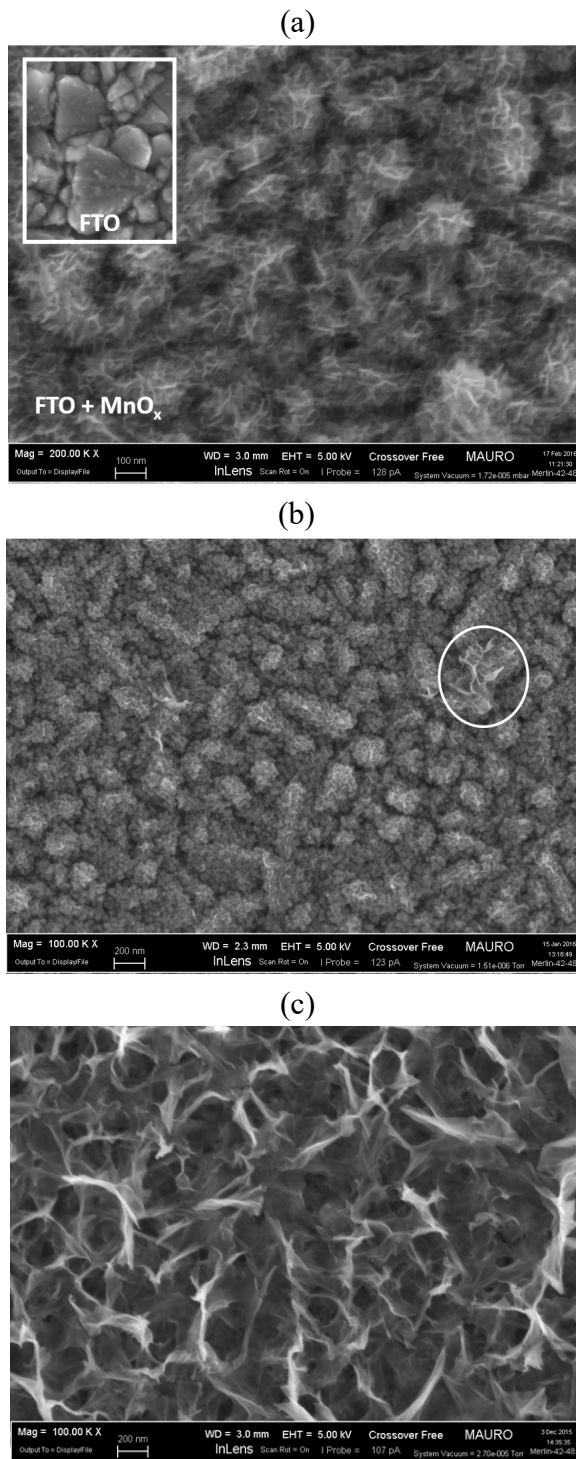


**Figure 40** FESEM images of MnO<sub>x</sub> material deposited on FTO for (a) 2.5 min, (b) 5 min, and (c) 10 min.[63] While in (a) and (b) FTO grains can be seen distinctly (inset (a) for reference), the structures in (c) completely obscure the form of FTO grains with flake-like morphology. This morphology can also be seen beginning to form in (b) where circled.

where the electrodeposition had happened for 5 min (Fig. 40(b)) and a deposition for 10 min (Fig. 40(c)). The former has a very similar morphology to FTO grains (grains can be seen distinctly, see inset of Fig. 40(a)) while the material from 5 min deposition shows the beginning of flakes growing (circled in Fig. 40(b)). Finally Fig. 40(c) shows material grown into large flakes that obscure these grains of FTO.

Those samples deposited with smaller deposition area show more consistent and higher catalytic activity per unit area in WOR testing. A small deposition area (< 1cm<sup>2</sup>) is standard across the literature and considered to be because of a more homogeneous material created. Larger areas of electrodeposition in our experiments produced larger regions of material with more thickness (larger particles obscuring FTO grains) at the edges.

Though heat treatment of the material shows no change in FESEM images, it is postulated that the material is being dehydrated. This was shown by Zhou et al. in their paper on heat treatment of MnO<sub>x</sub> materials, that at low temperatures there is a decrease in the FTIR absorption region of water but no change or reorganization of the structure.[32] This dehydration may cause an improvement in consistency of performance. We theorize that removing water from the structure makes active sites for catalysis more consistently available, explaining the improved consistency in WOR activity among heat treated samples. Heat treated samples also show overall higher activity for WOR catalysis. This is difficult to explain because the peak current in CA testing theoretically would not be affected by initial active site availability, since the potential is slowly stepped up. In the literature however heat treatment is shown to improved catalytic activity[32], [39]. My results in Fig. 35 show that for almost every concentration of Fe(III) in solution, the resulting Fe-MnO<sub>x</sub> samples have a higher activity when heat treated.

Since we are proposing a birnessite-type structure of the MnO<sub>x</sub> material (see 4.2.3 *Discussion of structural/characterization results*), we would presume there are sheets of water molecules found between sheets of the MnO<sub>x</sub> structure. The material could be undergoing a loss of this structurally-incorporated water during our mild heat treatment, which might reduce the crystallinity of the birnessite structure. In the literature, poorly

crystalline birnessite is correlated to a higher catalytic activity for water oxidation.[28], [29]

In many places in the literature, adding electroconductive foreign elements to a catalyst for WOR is an oft-used technique for improving activity. Since Ca is part of the water oxidizing molecule in nature, we tried adding a Ca compound to our electrodeposition solution. However, the potentially Ca-containing material quickly showed to be unpromising for WOR catalysis, compared to MnO<sub>x</sub> deposited material. We tried a Ruthenium compound in the electrodeposition solution too, but we observed that the Ru formed a precipitate with KMnO<sub>4</sub> and did not electrodeposit onto the electrode surface, prohibiting formation of MnO<sub>x</sub> catalyst in the electrode as well.

The main discussion of my thesis centers around the addition of iron to the MnO<sub>x</sub> electrocatalyst. I explored the addition of an Fe(III) species to the deposition solution, which showed promise so we decided to make our focus on the introduction of iron to the structure. This lead to the honing in of the optimal concentration of Fe(NO<sub>3</sub>)<sub>3</sub> in the deposition solution. After many samples were produced and tested, I found that the result was that, on average, smaller concentrations produced catalysts with higher activities (Fig. 39) with a peak activity of the resultant materials from solutions with 0.35 mM Fe(III). However, to study why this addition of iron causes an increase in catalytic activity, we had to gain more information about the material structure using methods besides electrochemical WOR testing. These are outlined in the following sections.

## 4.2 Structural/elemental characterization

The trend in activity based on Fe(NO<sub>3</sub>)<sub>3</sub> in deposition solution prompted us to study how Fe is changing the surface and to learn more about the composition of the material. We decided to take field emission scanning electron microscopy (FESEM) images of

representative samples to look for a change in morphology on the surface. XPS was also obtained to determine the amounts of different elements identifiable in the material.

#### 4.2.1 FESEM

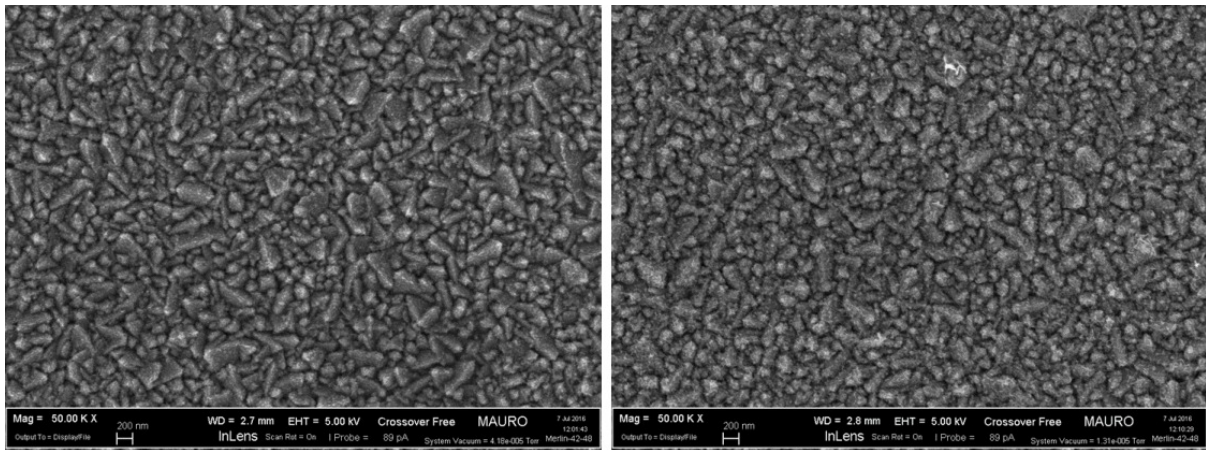


**Figure 41** FESEM images of samples of 1.5 mM KMnO<sub>4</sub> (left) and 1.5 mM KMnO<sub>4</sub> + 0.25 mM Fe(NO<sub>3</sub>)<sub>3</sub> (right) taken in the middle of the sample

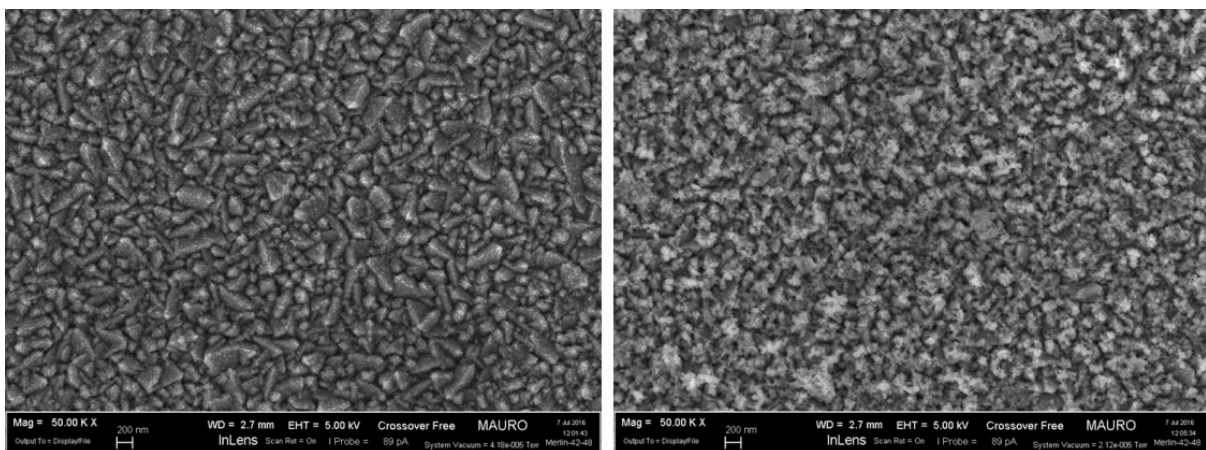


**Figure 42** FESEM images of samples of 1.5 mM KMnO<sub>4</sub> (left) and 1.5 mM KMnO<sub>4</sub> + 1.00 mM Fe(NO<sub>3</sub>)<sub>3</sub> (right) taken in the middle of the sample

Field emission scanning electron microscopy (FESEM) images were taken of different spots on samples at various magnification levels. Samples deposited in 1.5 mM KMnO<sub>4</sub>, 1.5 mM KMnO<sub>4</sub> and 0.25 mM Fe(NO<sub>3</sub>)<sub>3</sub>, and 1.5 mM KMnO<sub>4</sub> and 1.00 mM

Fe(NO<sub>3</sub>)<sub>3</sub> were used. At 50kx magnification, differences in the morphology are difficult to determine (Fig. 41 and Fig. 42).

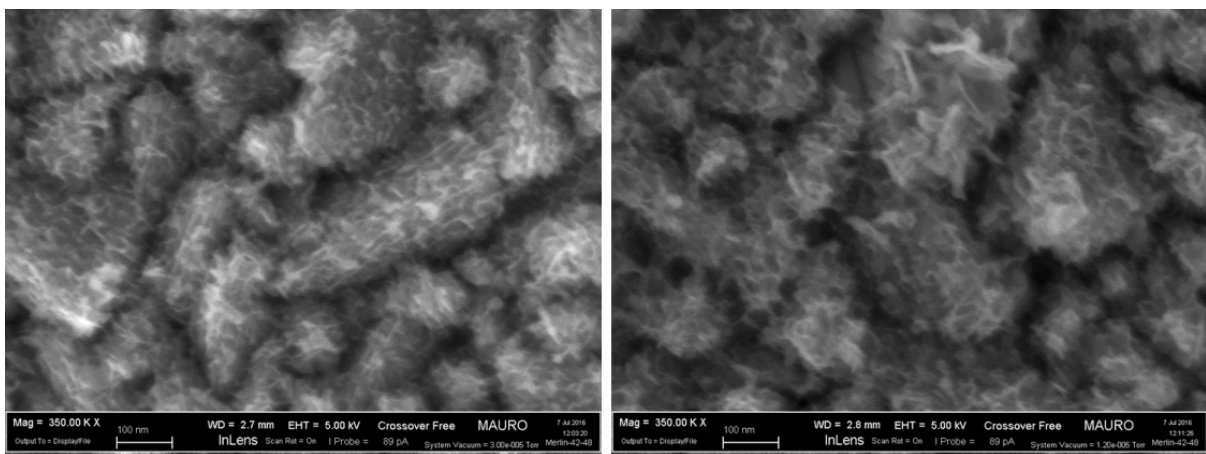


**Figure 43** FESEM images of samples of 1.5 mM KMnO<sub>4</sub> (left) and 1.5 mM KMnO<sub>4</sub> + 0.25 mM Fe(NO<sub>3</sub>)<sub>3</sub> (right) taken in the middle of the sample

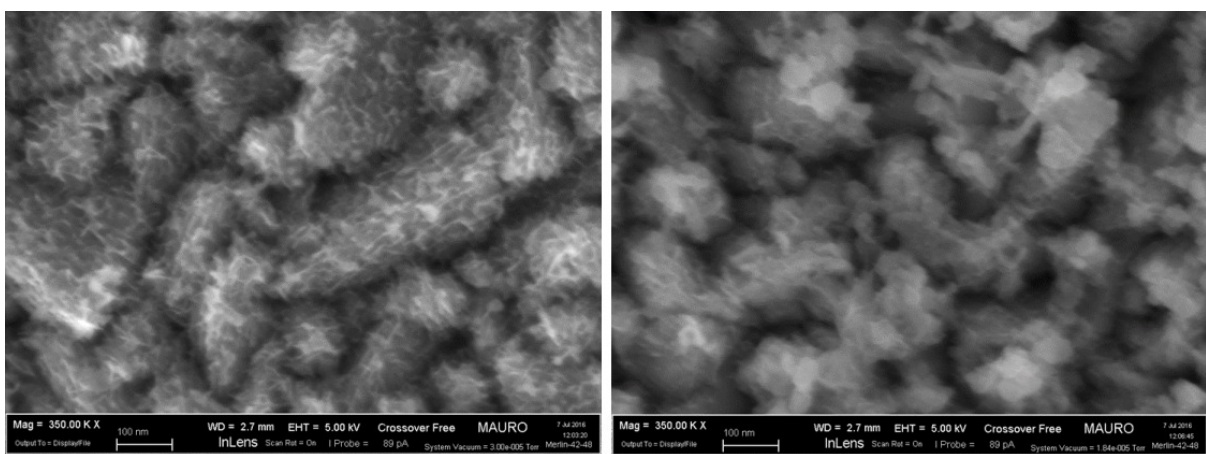


**Figure 44** FESEM images of samples of 1.5 mM KMnO<sub>4</sub> (left) and 1.5 mM KMnO<sub>4</sub> + 1.00 mM Fe(NO<sub>3</sub>)<sub>3</sub> (right) taken in the middle of the sample

Defined structures can be seen at a higher magnification, as in Fig. 43. These structures can be described as lamellar - looking like plates or flakes of material that grow in layers with different material (or space) between them. In Fig. 43 the lamellar structures have grown on FTO grains so that the shape of the FTO grains are still visible. However, in Fig. 44, the sample deposited in 1.5 mM KMnO<sub>4</sub> + 1.00 mM Fe(NO<sub>3</sub>)<sub>3</sub> (right) does not have a lamellar structure. The structure looks amorphous, not

like plates or flakes, and the shape of the FTO grains have become obscured by the deposited material.

At the edges of the samples, more material is deposited because the electrode has access to more current flow here (since the electrode is not two-dimensional). This deposited material's morphology is more defined than in the middle of the samples, where only a thin material layer is deposited on FTO grains. In Fig. 45, on the left we have an image of the edge of a sample deposited from 1.5 mM KMnO<sub>4</sub> + 0.25 mM Fe(NO<sub>3</sub>)<sub>3</sub>. Here the structure of flakes are obvious, which form from a thicker amount of the material with lamellar structure (see Fig. 40 for an example of this MnO<sub>x</sub> material structure grown at short and longer times). On the right shows the edge of sample deposited from 1.5 mM KMnO<sub>4</sub> + 1.00 mM Fe(NO<sub>3</sub>)<sub>3</sub> and the structure is clearly not lamellar (no flakes), but instead large particles of clearly different-coloured material have grown on the surface. We postulate that this is a form of iron oxide growing because of the higher concentration of Fe(III) in solution.

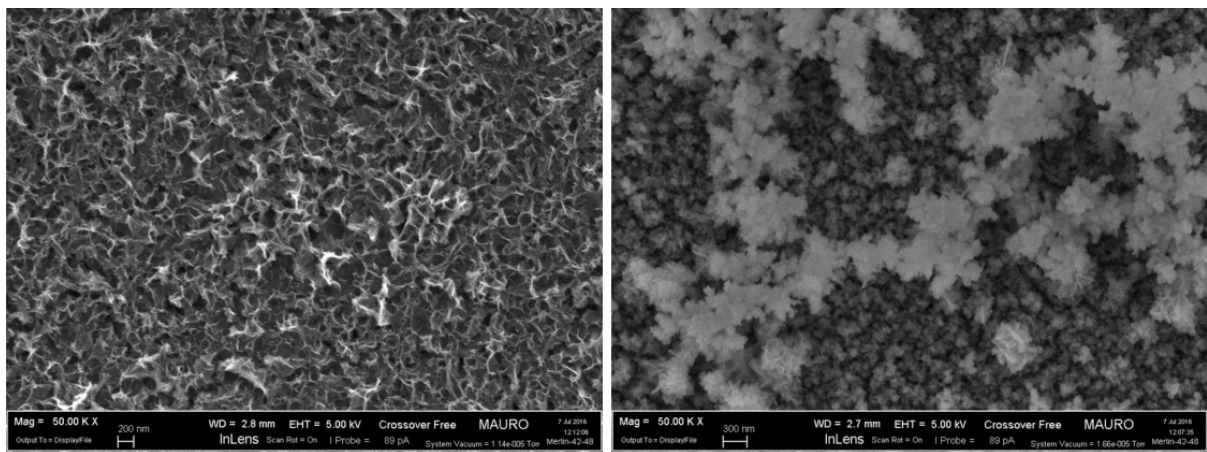


**Figure 45** FESEM images of samples of 0.25 mM Fe(NO<sub>3</sub>)<sub>3</sub> (left) and 1.00 mM Fe(NO<sub>3</sub>)<sub>3</sub> (right) taken at the edge of the samples

#### 4.2.1.1 Feature analysis

For all FESEM images presented, analysis was performed using ImageJ software. The purpose of this analysis was to develop a quantitative measure of how “different” the images are, and not to accurately measure the specific nanostructures seen in the images. That is, I wanted to extract measurements of *features* of these images to strengthen conclusions about the qualitative differences seen. In the resulting analysis seen in Table 2 and Table 3 I refer to “particles”, meaning the features I am using to quantify difference between images (not physical particles of the material).

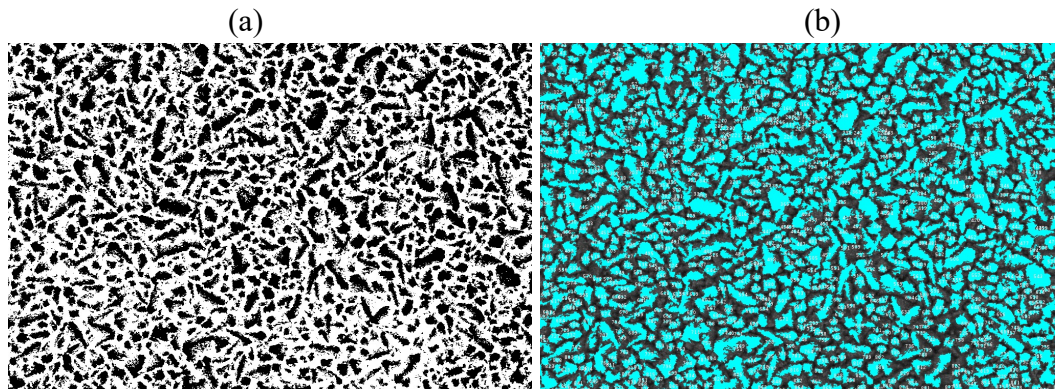


**Figure 46** FESEM image at 50kx magnification with gray intensity threshold applied (a) and structure analysis overlay (b). The threshold is used to separate particle structures, and the analysis overlay counts and takes measurements of these structures.

Using ImageJ, I applied gray intensity thresholding (Fig. 46(a)) and the "Analyze particles" function (Fig. 46(b)) to retrieve quantitative analysis of the FESEM images. The level of thresholding was optimized using high resolution images, where microstructures could be counted manually and confirmed that the threshold was identifying all structures.

In Table 2 I present the microstructure analysis for all FESEM images collected in the middle of the sample. For each sample I used magnification of 50kx and 350kx for analysis.

Middle of sample				
Fe [mM]	Mag (kx)	Count	Avg area / particle (nm <sup>2</sup> )	Area % of particles
0	50	893	16556	44.1%
0.25	50	965	15186	43.7%
1.00	50	576	26047	44.9%
0	350	25	12892	43.1%
0.25	350	20	16759	44.7%
1.00	350	16	21355	45.8%

**Table 2** FESEM microstructure analysis for images taken in the middle of the sample at 50kx and 350kx magnification.

In Table 3 I show the same analysis for images taken at the edge of the sample. An image at the edge of the sample with material from 1.5 mM KMnO<sub>4</sub> with no iron species addition was only taken at 200kx, so this is reported for completeness but not directly comparable to analysis of the 50kx and 350kx FESEM images of the other two samples from solutions with Fe(NO<sub>3</sub>)<sub>3</sub>. I was unable to gain informative analysis of the 350kx magnification image at the edge of the sample from 1.00 mM Fe(NO<sub>3</sub>)<sub>3</sub>, because of the indistinct nature of the structure. Fig. 47(b) shows this image compared to the similar 350kx magnification image of the sample from 0.25 mM Fe(NO<sub>3</sub>)<sub>3</sub> (Fig. 47(a)), where the structure is much more distinct. The image analysis of Fig. 47(b) gives the count of only one particle.

Edge of sample				
Fe [mM]	Mag (kx)	Count	Avg area / particle (nm <sup>2</sup> )	Area % of particles
0	200	47	22576	47.4%
0.25	50	548	19376	31.6%
1.00	50	271	66946	53.1%
0.25	350	8	38371	40.87%
1.00	350	N/A	N/A	N/A

**Table 3** FESEM microstructure analysis for images taken in the edge of the sample at 50kx and 350kx magnification for samples containing Fe(II) species. For the sample containing no iron, the analysis comes from an image at 200kx magnification.

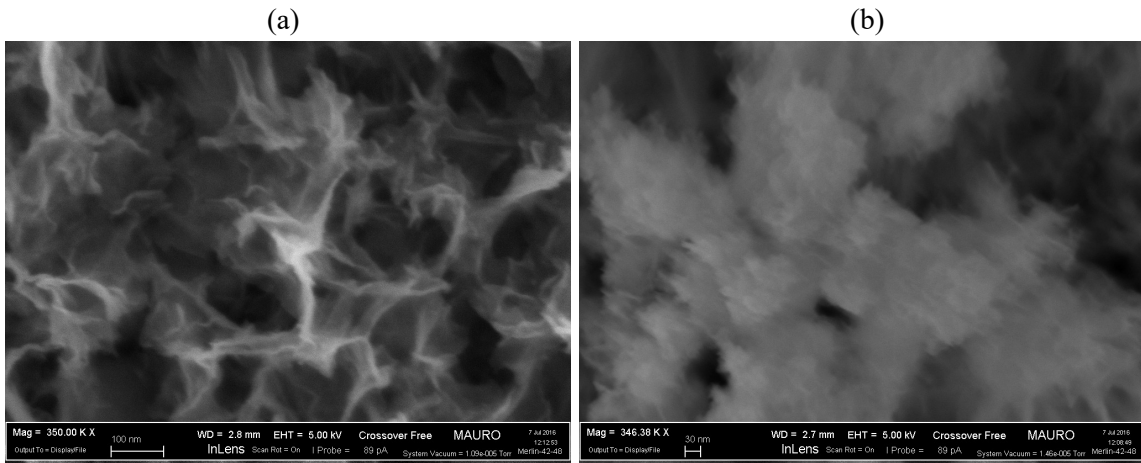


**Figure 47** FESEM images of the edge of the samples at ~350kx magnification. (a) Sample from a solution with 1.5 mM KMnO<sub>4</sub> + 0.25 mM Fe(NO<sub>3</sub>)<sub>3</sub>. (b) Sample from a solution with 1.5 mM KMnO<sub>4</sub> + 1.00 mM Fe(NO<sub>3</sub>)<sub>3</sub>. In (a) distinct structures are clearly visible, in (b) the particles are not distinct.

## 4.2.2 XPS

XPS scans were performed as outlined in the Methods chapter (3.3.1 *XPS*). In Fig. 48 I show example spectra collected from a sample from 1.5 mM KMnO<sub>4</sub> + 0.35 mM Fe(NO<sub>3</sub>)<sub>3</sub> in solution. From spectra such as this, the resulting atomic % of each species found in the XPS are reported in Table 4.

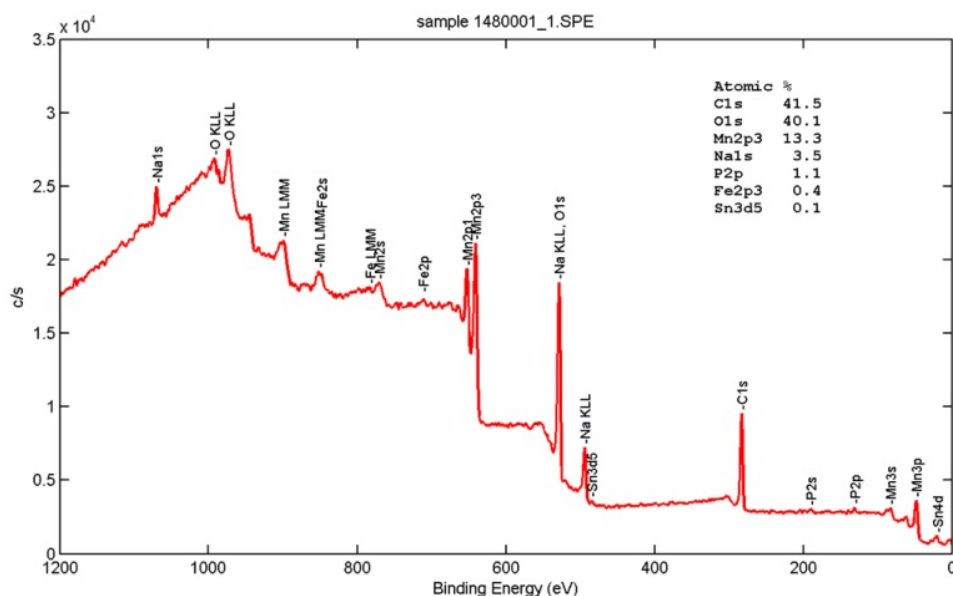


**Figure 48** XPS scan from sample deposited in 1.5 mM KMnO<sub>4</sub> + 0.35 mM Fe(NO<sub>3</sub>)<sub>3</sub>

From this table we can see that the concentration of Fe(III) in the deposition solution has a correlating trend with the Mn/Fe ratio in atomic % found on the surface of the sample. For 0.25 mM Fe(III) in solution, there is an average 74 Mn atomic % per Fe atomic %. For 0.35 mM Fe(III) in solution, this number is 33 Mn/Fe, and for 1.00 mM Fe(II) the average is 3 Mn/Fe so there is significantly more iron on this surface compared to depositions from lower concentrations of iron compound.

We also saw measurements of Na, P, and Sn on the sample surface for all samples except pure FTO and one of the measurements of a sample electrodeposited from only

KMnO<sub>4</sub> (no Fe(III) in deposition solution. This measurement (denoted with a footnote) was not electrochemically tested in the NaPi buffer, so we can be sure that Na and P are visible in small amounts on the surface only because of some of these species remaining after testing. Notice too that an Sn component is measured for all samples, meaning the film is likely thin enough that the XPS sees the FTO substrate.

[mM]	atomic %						
Fe(NO <sub>3</sub> ) <sub>3</sub>	C	O	Mn	Fe (Mn/Fe)	Na	P	Sn
0	43.2	38.4	11.2	-	4.7	1.9	0.7
0 (HT)	38.5	41.5	13.0	-	2.4	3.4	1.1
<sup>6</sup>	36.0	44.0	17.2	-	-	-	2.4
0.25	34.2	44.6	13.4	0.2 (67)	5.0	2.1	0.5
0.25 (HT)	23.6	51.4	17.4	0.2 (87)	4.7	1.9	0.8
0.35	41.5	40.1	13.3	0.4 (33)	3.5	1.1	0.1
0.35 (HT)	39.8	41.1	13.4	0.4 (33)	3.8	1.4	0.2
1.00	42.5	40.0	7.7	4.1 (1.9)	2.2	1.3	2.2
1.00	42.7	40.0	8.0	2.0 (4.0)	3.7	2.1	1.1
1.00	47.6	37.1	6.3	2.1 (3.0)	3.2	2.3	0.9
FTO	28.8	42.2	-	-	-	-	29

**Table 4** XPS elemental analysis results

Another interesting result from the XPS measurements was related to the O1s peak as seen in Fig. 49. We saw that in the case without iron in the structure (top two spectra in Fig. 49) the heat treatment shows a reduction of the first peak seen in the non-heat treated sample. However, for samples containing iron (bottom two spectra in

<sup>6</sup> As deposited, i.e. not tested with CV or CA before XPS was taken

Fig. 49) this reduction of the peak is already seen in the non-heat treated sample and does not change when the sample undergoes heat treatment.

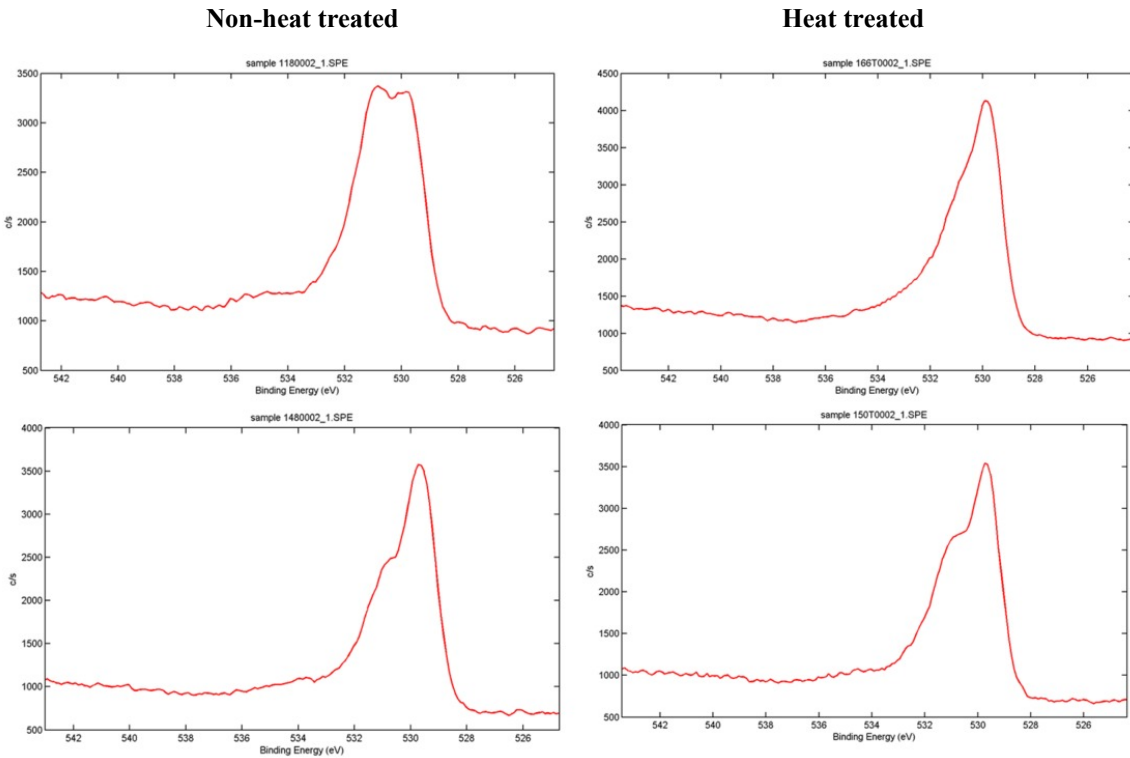


**Figure 49** XPS high resolution scans of the O1s peak from samples deposited in 1.5 mM KMnO<sub>4</sub> (top) and 1.5 mM KMnO<sub>4</sub> + 0.35 mM Fe(NO<sub>3</sub>)<sub>3</sub> (bottom). On the left are non-heat treated samples, on the right are heat treated samples

#### 4.2.3 Discussion of structural/characterization results

FESEM images in Fig. 41 and Fig. 43 show that the morphology is very similar between materials deposited in 1.5 mM KMnO<sub>4</sub> and those deposited in 1.5 mM KMnO<sub>4</sub> + 0.25 mM Fe(NO<sub>3</sub>)<sub>3</sub>. The FTO grains are clearly visible (see Fig. 40(a) for blank FTO inset to MnO<sub>x</sub> on FTO material) for samples with lower concentration of Fe(III) in their deposition solution. From this we conclude that the material covering the surface is very thin and growing evenly on top of the FTO grain morphology. We theorize that the material structure is very similar between samples from these two deposition solutions,

and that Fe species are incorporated into a consistent MnO<sub>x</sub> structure. The morphology is similar to that of other birnessite-like MnO<sub>x</sub> in previous work[30], [31], [64] so we hypothesize this crystal structure of the material.

In samples with a higher concentration of Fe(III) in the deposition solution, the FTO grain structure is less visible and the particles are much less lamellar in their formation (lamellar meaning looking like flakes grown in layers with material/space between, as previously described). With a higher amount of the Fe(III) species in solution, it seems that the iron is not being incorporated into the same MnO<sub>x</sub> structure but growing a distinct iron structure (presumably iron oxide) on the surface of the material.

Using the microstructure analysis, we can conclude that the average area per particle on these surfaces is larger in the case of samples from 1.00 mM Fe(NO<sub>3</sub>)<sub>3</sub> in solution. This is especially clear when examining the analysis of the image at the edge of the sample, where the particle average is 66946 nm<sup>2</sup> compared to 22576 nm<sup>2</sup> and 66946 nm<sup>2</sup> for the samples from Mn(VII)-only and 0.25 mM Fe(III)-containing solutions.

The XPS elemental analysis confirms for us that the amount of iron in the electrodeposited structure (total or relative to Mn species) is related to the amount of Fe(III) species in solution, so a relationship between the iron content and WOR activity for the catalyst may exist. These results also support the idea that the non-lamellar structures seen by FESEM imaging in Fig. 42(right) and Fig. 44(right) could be large iron structures, since the atomic% of Fe is so high on the samples from 1.00 mM Fe(NO<sub>3</sub>)<sub>3</sub>.

We observed in Fig. 49 that the O1s peak shows a similar change when an MnO<sub>x</sub> (no iron) sample goes through heat treatment, compared to when iron is added in the case of a deposition from 1.5 mM KMnO<sub>4</sub> + 0.35 mM Fe(NO<sub>3</sub>)<sub>3</sub>. The increase in WOR activity when a small amount of iron is found in the structure could be related to this change in the O1s peak, since an activity increase also arises when the catalyst material is dehydrated.

## 4.3 Work function results

We were motivated to investigate properties of the electronic structure of the Fe-MnO<sub>x</sub> materials, and decided to pursue this with the use of a Kelvin probe. Measurements are quick and do not have to be performed in vacuum, so we were able to do this for a number of samples.

### 4.3.1 Surface measurements

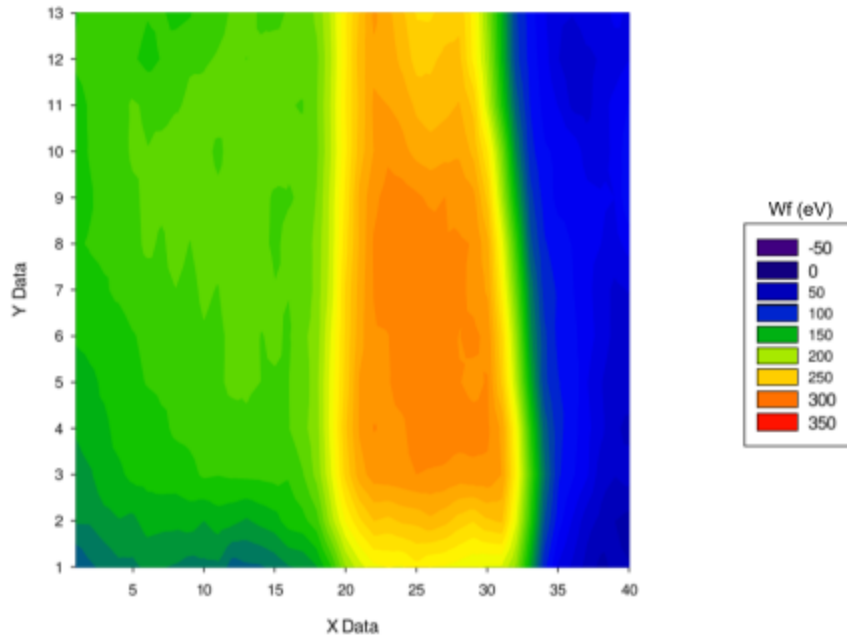


**Figure 50** An example heat map of the work function of one sample, adapted from [65]. From  $X \approx 20 - 33$  was a small band of very high work function, and to the right of this is the area where the tape had been placed. To the left is the electrodeposited Fe-MnO<sub>x</sub> material.

One type of scan a Kelvin probe can take is of the work function at many points across a surface, to give a heat map of the data as in Fig. 50. This is interesting for our

experiment because we can verify the distinction between different materials on our surface (previously confirmed visually; the deposited material is brown while FTO glass is transparent), presuming that different materials will have different values of work function. The heat map also alerted us to a high uniformity of the catalyst films we were creating, as the variation in the work function of the Fe-MnO<sub>x</sub> material is relatively small (from  $X \approx 1 - 20$  of Fig. 50).

Another point of interest regarding this type of scan was the region shown in Fig. 50 as above as  $X \approx 20 - 33$ . This area had a high work function of above 250 eV, and was a small strip of area at the interface between the deposition area and where the tape was located to designate the deposition area on the FTO glass. We measured blank FTO and the work function was found to match the rest of the area where the tape was placed (very low work function, around  $X > 33$ ).

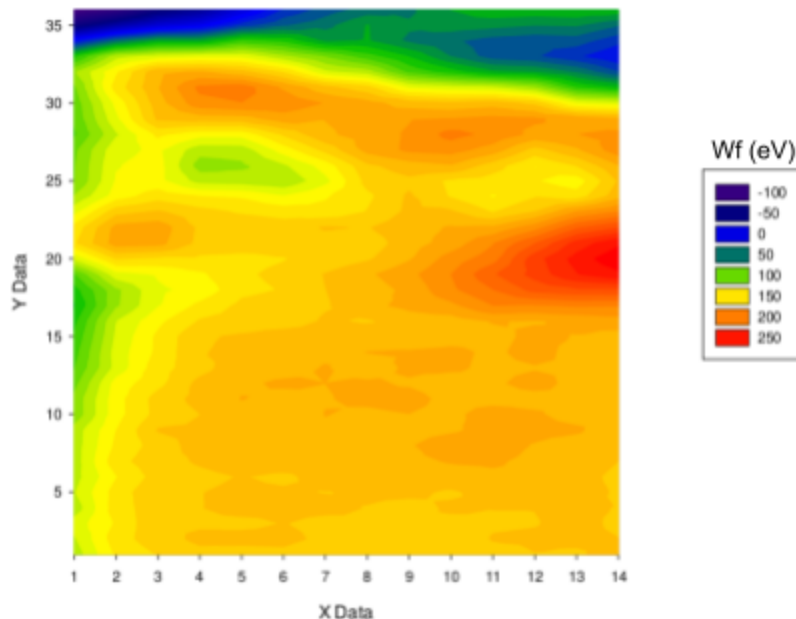


**Figure 51** Surface heat map of a sample without tape. The physical orientation of the sample is rotated 90° counterclockwise from Fig. 50 so that the region from  $Y > 33$  is the region of blank FTO. Adapted from [65].

We then used the Kelvin probe to take a surface survey of a deposited sample where no tape had been used to designate the deposition area (instead the level of deposition solution was carefully measured to match the correct area on the electrode). The result is in Fig. 51, and in this heat map there is no distinct band where the work function is above 250eV.

### 4.3.2 Average work function of the material

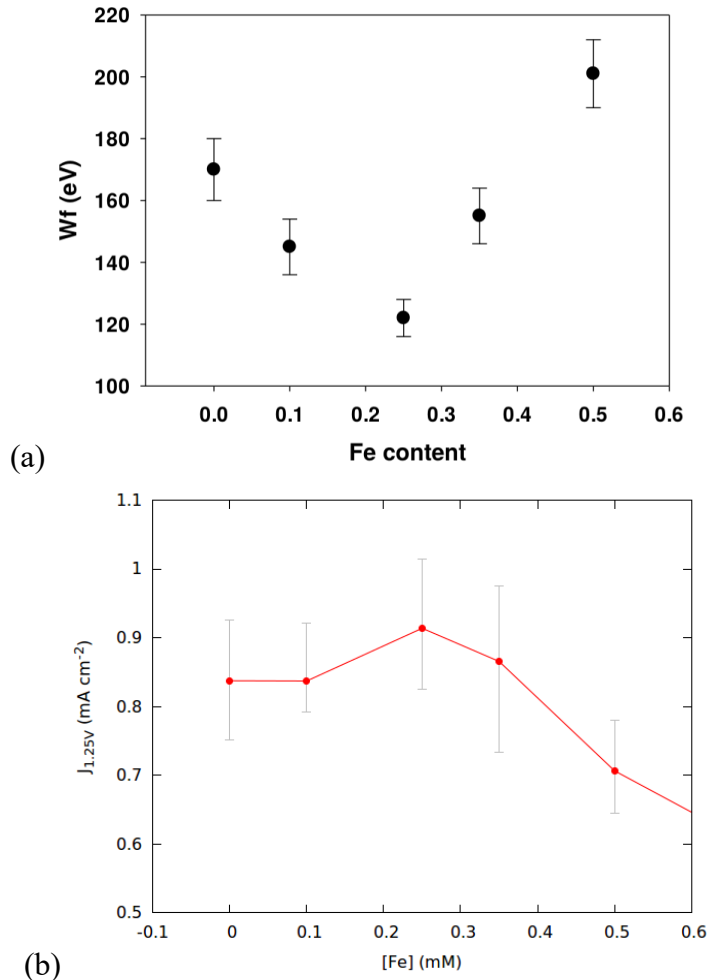


**Figure 52** Kelvin probe work function measurements (a) for samples of different concentration Fe(NO<sub>3</sub>)<sub>3</sub> deposition solutions, adapted from [65]. Compared with current density at 1.25V for the same Fe(NO<sub>3</sub>)<sub>3</sub> concentration samples (b)

While the heat maps of the work function on the surface of the sample were interesting, much more relevant was the average work function of the electrodeposited catalyst material. This was taken for multiple samples deposited from each Fe(NO<sub>3</sub>)<sub>3</sub> concentration solution, but more measurements were taken for those with closer concentrations to the 0.25 mM - 0.35 mM Fe(III) which showed a peak in the current density during WOR testing. The Kelvin probe work function and  $J_{1.25V}$  results for samples deposited from 0.0 - 0.5 mM Fe(III) are compared in Fig. 52.

### 4.3.3 Discussion of work function results

Regarding the work function maps of the surface, one observation is the relative homogeneity of the catalyst material produced (at least in terms of work function, which tends to signify a similar material). This shows an advantage of the facile and simple method we have presented to electrodeposit this catalyst material. Another area of interest for discussion is in Fig. 50 at  $X \approx 20 - 33$ . This area of high work function is unexplained. We believe it might be due to an incomplete seal of the tape on the FTO glass, thereby leaving space for the deposition solution to reach the FTO under a small portion at the edge of the tape. However, the material being deposited in this region is not similar in work function to the rest of the deposited material, so we propose that in this small band an intermediate material may have been produced. This could be due to a minimal reaction with the underside of the tape, although we think this is unlikely. Perhaps a similar MnO<sub>x</sub> material is depositing, but where at the beginning of the reaction the kinetics are mass-transfer-controlled, the material depositing slightly under the tape is not forming an oxide layer necessary for a catalytically active MnO<sub>x</sub>.

The main result in this section is that of Fig. 52. The average work function of the Fe-MnO<sub>x</sub> catalyst material tends to decrease as the current density of the material in WOR increases. This is an intriguing observation; recall that the work function of the material being lower means that it takes less thermodynamic work to move an electron

from the surface to vacuum at infinity. If this is the case, it may mean that the addition of a small amount of iron in the structure decreases the amount of energy needed to do electric work on the surface of the material.

# 5 Conclusions and future perspectives

In this thesis, I have described the synthesis process of an MnO<sub>x</sub> and Fe-MnO<sub>x</sub> electrocatalyst for water oxidation. This has involved the preparation and electrodeposition of the material on an FTO electrode, including considerations of a constant current vs. constant potential electrodeposition and the ideal length of deposition time, size of deposition area, and concentration regime. We have concluded that the optimal synthesis protocol for this material is: electrodeposition from a relatively low concentration regime (0-2 mM compared to one magnitude higher) through constant current, a specific deposition time stopped after a distinct drop in the potential (typically 130-150s), a deposition area of 1cm<sup>2</sup> or smaller, and heat treatment of the sample following the deposition. This synthesis method is simple and fast since it does not require any more complicated conditions such as voltage cycling, heating, stirring,

vacuum, or calcination. It also seems to produce a fairly homogeneous surface in terms of electronic properties, as shown by Kelvin probe work function heat maps.

I also explored the addition of foreign metals to the electrodeposited MnO<sub>x</sub> material. Deposition from a Ca-containing solution resulted in samples with very low WOR activity, and deposition failed from a solution with Ru species. However, the addition of an Fe(III) species to the deposition solution resulted in an increase in catalytic activity. From thereon the thesis focused on the catalyst material with respect to Fe(III) species in the electrodeposition solution.

In FESEM images, we saw that the MnO<sub>x</sub> material grows in a thin layer over FTO grains, leaving the shape of the grains clearly visible. The material has a lamellar morphology, looking like small plates or flakes grown in thin layers with space between them. In samples from a solution with small concentrations of Fe(NO<sub>3</sub>)<sub>3</sub> (0.25 mM) the structure looks very similar to that of the non-iron containing MnO<sub>x</sub> material. Images of samples from larger concentrations of Fe(NO<sub>3</sub>)<sub>3</sub> (1.00 mM) show particles that are much less lamellar. Especially at 350.0kx magnification, this structure is clearly more amorphous.

Due to this distinction between lamellar and non-lamellar morphology, we posit that at small concentrations of Fe(III) species in the deposition solution, iron is being incorporated into the MnO<sub>x</sub> structure and so these samples present the same morphology. However at larger concentrations of Fe(III) species in the deposition solution, an iron oxide is forming which is observed by the different-looking particles in the FESEM images. This is supported by XPS elemental analysis, which shows a difference as large as 85 Mn atomic% per Fe atomic % for the 0.25 mM Fe(NO<sub>3</sub>)<sub>3</sub>-deposited sample to the 1.00 mM Fe(NO<sub>3</sub>)<sub>3</sub>-deposited sample (87 Mn/Fe compared to 1.9 Mn/Fe, respectively).

We also observe that in the high-resolution O1s spectra, the iron-containing sample seems to exhibit a similar peak to a heat-treated MnO<sub>x</sub> (non-iron-containing) sample. Since we believe that this heat treatment is only dehydrating the structure, and not causing any electronic or chemical change, we propose that the iron could be displacing some of the water in the structure.

Finally, I considered some work function measurements of the material. The work function surface heat maps revealed a significant band of high work function level between the catalyst surface and the blank FTO, which was a result of the tape used to designate deposition area on the FTO glass. The average work function of the Fe-MnO<sub>x</sub> and MnO<sub>x</sub> samples trended inversely with the average activity of the same samples, with the work function being low if the WOR activity measurement was high. This result is promising for future investigation of this material through first principles calculations, since the work function is a simple value to obtain through quantum chemistry simulations. Some preliminary exploration of these computational methods is outlined in Appendix A.

Regarding practical application of this material for catalyzing water oxidation reactions, this synthesis method provides several advantages. The electrodeposition protocol is simple and reproducible, requiring no complex treatments of the films. The material can be easily re-deposited on a substrate in the case of a damaged or recycled sample, by running the same electrodeposition with a fresh deposition solution. A challenge in real-world application would be the scaling of this synthesis, since electrodeposition has been shown to be more stable and homogeneous on a smaller surface. This is due to the thicker material deposition on the edges proportionality to the surface area, and could potentially be overcome with an interconnected structure of low surface area substrates.

This work could be expanded in the future in many aspects. One intuitive avenue to explore would be more band structure properties of the material, i.e. energy gap as a function of iron. This would require electrochemical impedance spectroscopy (EIS) measurements with resolution of the cell vs. material resistance for the different Fe(III) content materials presented. The result would be conductivity of the materials that could lead for more discussion about the energy bands and possible conductor or semiconductor properties based on iron presence in the material.

# 6 Appendix A

## 6.1 Preliminary computational results

With some values for the work function of the material provided by the Kelvin probe, we decided to explore some preliminary computational simulations of the material. Work function is a measurement that is attainable through first principles chemistry calculations, and if these measurements resulted in a similar trend in the work function, then we could gain computational insights into the electronic structure of the material.

## 6.2 Density Functional Theory

To accurately simulate a system of atoms with the goal of gaining electronic structure information, the system must be considered from first principles, i.e. quantum mechanics. Hence, the many-body Schrödinger equation must be the starting point. Eq. 51 is the many-body Hamiltonian of a system of atoms, which considers the kinetic and electrostatic energies of electrons and ions in a system.

$$\hat{H} = -\frac{\hbar^2}{2m_e} \sum_i \nabla_i^2 - \sum_{i,I} \frac{Z_I e^2}{|\mathbf{r}_i - \mathbf{R}_I|} + \frac{1}{2} \sum_{i,j} \frac{e^2}{|\mathbf{r}_i - \mathbf{r}_j|} - \sum_I \frac{\hbar^2 \nabla_I^2}{2M_I} - \sum_{I,J} \frac{Z_I Z_J e^2}{|\mathbf{R}_I - \mathbf{R}_J|} \quad \underline{51}$$

In this equation electrons are denoted with lower-case variables and ions are denoted with upper-case variables. The first term represents the kinetic energy of electrons, second term represents the ion-electron interaction, third term is the

electron-electron interaction, fourth term is the kinetic energy of ions, and the fifth term is the ion-ion interaction.

The Born-Oppenheimer approximation is typically applied to make this Hamiltonian feasible to solve for a many-body system. This approximation represents the ion-ion interaction energy as a constant added to the final energy, and considers the kinetic energy of ions as negligible since the dependence of the large nuclear mass of ions ( $1/M_i$ ) makes this term very small. The result can be seen in Eq. 52.

$$\hat{H} = \hat{T} + \hat{V}_{ie} + \hat{V}_{ee} + E_{II} \quad \underline{\text{52}}$$

where  $\hat{T}$  is the electron kinetic energy,  $\hat{V}_{ie}$  is the ion-electron interaction energy, and  $\hat{V}_{ee}$  is the electron-electron interaction energy. Using this equation to solve the many-body Schrödinger equation (Eq. 53) there are still  $3N$  variables for an  $N$  electron system (3 spatial dimensions for each electron). This can be solved analytically for a hydrogen atom, but any system with more electrons is impossible to solve.

$$\hat{H}\Psi(\{r_i : i = 1...N\}) = E\Psi(\{r_i : i = 1...N\}) \quad \underline{\text{53}}$$

However, Hohenberg and Kohn's theorems[66] simplify this problem. They proved that all of the properties of a system of atoms can be described as functionals of electron density, which is itself a function of only  $x, y, z$ . This is the beginning of the basis for the density functional theory view of atomic simulations. The theorems of Hohenberg and Kohn and their implications are described below.

**Theorem 1.** The ground state electron density of a system  $\rho(\vec{r})$  contains all of the information about that system. Any observables of the system are functionals of  $\rho(\vec{r})$ , where functionals, by definition, take a function as input and output a value or number

(integrals are functionals). Hohenberg and Kohn proved the existence of density functionals, but the exact form of these functionals are not known.

**Theorem 2.** If we want to study a system of interacting electrons, we can model them as a system of non-interacting electrons in a certain potential, and use this to make predictions regarding the interacting system. i.e.

$$\hat{H} = \hat{T} + \hat{V}_{ie} + \hat{V}_{ee} \quad \text{interacting electrons} \quad \underline{\text{54}}$$

has solutions  $\Psi(r_1, r_2, r_3)$  which have electron density  $\rho_{\text{int}}(\vec{r})$ . If we use

$$\hat{H} = \hat{T} + \hat{V}_{ie} + \hat{V}_H + \hat{V}_{XC} \quad \text{non-interacting electrons} \quad \underline{\text{55}}$$

instead, where  $\hat{V}_H$  is the Hartree potential, describing electron-electron Coulomb repulsion in terms of the density  $\rho(\vec{r})$  of the entire system.

$\hat{V}_{XC}$  is the exchange-correlation potential, also dependant on  $\rho(\vec{r})$ . However,  $\hat{V}_{XC}$  in its exact form is not known for most systems. (If the exact  $\hat{V}_{XC}$  could be found, then  $\rho_{\text{int}}(\vec{r}) = \rho_{\text{non-int}}(\vec{r})$ ) There are well-known approximations of  $\hat{V}_{XC}$ , including the local-density approximation (LDA) which only considers the density of the coordinate where the functional is, e.g.

$$\hat{V}_{XC}^{\text{LDA}}[\rho(\vec{r})] \rightarrow \hat{V}_{XC}(\vec{r}) \quad \underline{\text{56}}$$

The first theorem tells us that in any external potential environment, the energy can be defined by a unique functional of the electron density. The second theorem states that there exists a universal functional (in terms of electron density) for the energy of a system in any external potential. The ground state energy will be the global minimum of that functional, which corresponds to the ground state electron density.

Using functionals of electron density to solve each term in the Hamiltonian, a molecular system can be evolved using Newton's equation of motion ( $\mathbf{F} = m\mathbf{a}$ ). In density functional theory calculations, we use this method to describe and make predictions about a system of atoms or molecules. The difference between different DFT methods is typically in their approximation of  $\hat{V}_{XC}$

## 6.3 DFT calculations

DFT calculations in the form of structure relaxations and single-point calculations of an MnO<sub>2</sub> surface were performed using the Vienna Ab initio Simulation Package (VASP [67]), as well as the same surface with an Fe atom placed in the middle of the material. The MnO<sub>2</sub> material structure was obtained from [68] as the lowest energy structure with a similar ratio Mn:Fe as seen in the XPS of the deposited material.

All VASP relaxations were run with a 4x4x2 kpoint grid representing the density of the integrals being taken in reciprocal space. A Perdew-Burke-Ernzerhof (PBE) functional was used for the approximation of the exchange-correlation energy. Periodic boundary conditions were applied to the structure, and there was a plane-wave energy cutoff for the basis set of 500eV.

### 6.3.1 Computational calculation of work function

The workfunction was extracted from the output electrostatic potential data from a fully relaxed structure, by subtracting the vacuum level from the highest occupied molecular orbital energy level.

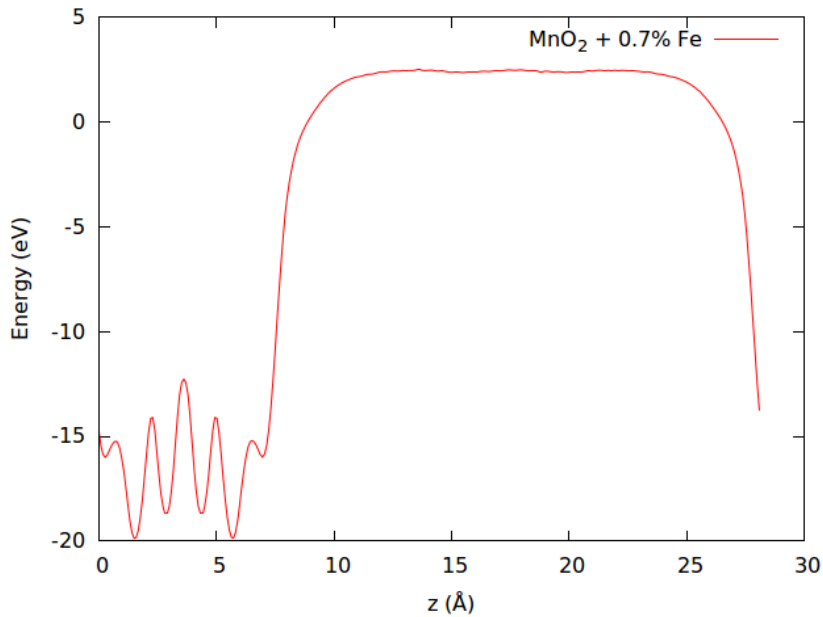


**Figure 53** An example of the electrostatic potential output from a VASP relaxation, indicating the MnO<sub>2</sub> + Fe material at z ~ 0 - 7 Å and vacuum at z > Å.

The difference in work function between the MnO<sub>2</sub> + vacuum structure and the MnO<sub>2</sub> + 0.7%<sub>atomic</sub> Fe + vacuum structure was found to be 26.9 meV. This is on the same order as the work function differences found by the Kelvin probe in 4.3 *Work function results*.

# 7 Appendix B

## 7.1 HR XPS scans of Fe

Recognizably, the confirmation of Fe speciation in the material would be substantial supporting evidence for the structural incorporation of iron or deposition of iron species on the surface. High resolution scans of only one concentration sample Fe were taken using XPS, which wouldn't allow for comparison between small and large content of Fe species. However, the scans gave indistinctive peaks that did not allow for clear analysis of Fe speciation at this time (see Fig. 54).

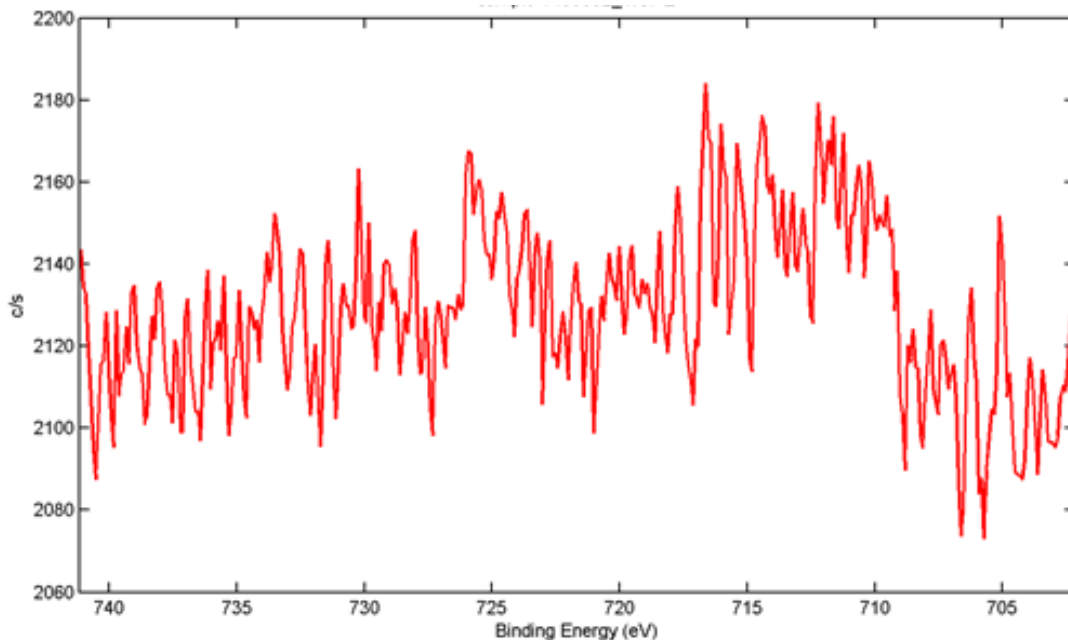


**Figure 54** High resolution XPS scan of a sample from 0.35mM Fe(III) in solution. The sample did not allow for resolution of Fe speciation due to considerable noise.

# 8 Bibliography

- [1] Intergovernmental Panel on Climate Change. Working Group III., *Carbon Dioxide Capture and Storage: Special Report of the Intergovernmental Panel on Climate Change*. Cambridge University Press, 2005.
- [2] Intergovernmental Panel on Climate Change and IPCC, *IPCC Fifth Assessment Report (AR5)*. 2013.
- [3] S. A. Rackley, *Carbon Capture and Storage*. Butterworth-Heinemann, 2017.
- [4] International Energy Agency, *Technology Roadmap: Solar Photovoltaic Energy*. 2010.
- [5] International Energy Agency (IEA) International Energy Agency (IEA) and World Bank Group World Bank Group, *Sustainable Energy for All 2013-2014: Global Tracking Framework Report*. World Bank Publications, 2014.
- [6] J. O. Bockris, “A hydrogen economy,” *Science*, vol. 176, no. 4041, p. 1323, Jun. 1972.
- [7] N.-T. Suen, S.-F. Hung, Q. Quan, N. Zhang, Y.-J. Xu, and H. M. Chen, “Electrocatalysis for the oxygen evolution reaction: recent development and future perspectives,” *Chem. Soc. Rev.*, vol. 46, no. 2, pp. 337–365, Jan. 2017.
- [8] A. Eftekhari, “Tuning the electrocatalysts for oxygen evolution reaction,” *Materials Today Energy*, vol. 5, pp. 37–57, 2017.
- [9] S. Cherevko *et al.*, “Oxygen and hydrogen evolution reactions on Ru, RuO<sub>2</sub>, Ir, and IrO<sub>2</sub> thin film electrodes in acidic and alkaline electrolytes: A comparative study on activity and stability,” *Catal. Today*, vol. 262, pp. 170–180, 2016.
- [10] M. Tahir *et al.*, “Electrocatalytic oxygen evolution reaction for energy conversion and storage: A comprehensive review,” *Nano Energy*, vol. 37, pp. 136–157, 2017.
- [11] C. C. L. McCrory, S. Jung, J. C. Peters, and T. F. Jaramillo, “Benchmarking Heterogeneous Electrocatalysts for the Oxygen Evolution Reaction,” *J. Am. Chem. Soc.*, vol. 135, no. 45, pp. 16977–16987, 2013.
- [12] T. Reier, M. Oezaslan, and P. Strasser, “Electrocatalytic Oxygen Evolution Reaction (OER) on Ru, Ir, and Pt Catalysts: A Comparative Study of Nanoparticles and Bulk

- Materials," *ACS Catal.*, vol. 2, no. 8, pp. 1765–1772, 2012.
- [13] I. C. Man *et al.*, "Universality in Oxygen Evolution Electrocatalysis on Oxide Surfaces," *ChemCatChem*, vol. 3, no. 7, pp. 1159–1165, 2011.
- [14] A. Eftekhari, "Tuning the electrocatalysts for oxygen evolution reaction," *Materials Today Energy*, vol. 5, pp. 37–57, 2017.
- [15] K. S. Egorova and V. P. Ananikov, "Toxicity of Metal Compounds: Knowledge and Myths," *Organometallics*, vol. 36, no. 21, pp. 4071–4090, 2017.
- [16] M. M. Najafpour *et al.*, "Manganese Compounds as Water-Oxidizing Catalysts: From the Natural Water-Oxidizing Complex to Nanosized Manganese Oxide Structures," *Chem. Rev.*, vol. 116, no. 5, pp. 2886–2936, Mar. 2016.
- [17] D. M. Robinson *et al.*, "Photochemical water oxidation by crystalline polymorphs of manganese oxides: structural requirements for catalysis," *J. Am. Chem. Soc.*, vol. 135, no. 9, pp. 3494–3501, Mar. 2013.
- [18] Y. Gorlin and T. F. Jaramillo, "A bifunctional nonprecious metal catalyst for oxygen reduction and water oxidation," *J. Am. Chem. Soc.*, vol. 132, no. 39, pp. 13612–13614, Oct. 2010.
- [19] A. Bergmann, I. Zaharieva, H. Dau, and P. Strasser, "Electrochemical water splitting by layered and 3D cross-linked manganese oxides: correlating structural motifs and catalytic activity," *Energy Environ. Sci.*, vol. 6, no. 9, p. 2745, 2013.
- [20] Y. Gorlin and T. F. Jaramillo, "A bifunctional nonprecious metal catalyst for oxygen reduction and water oxidation," *J. Am. Chem. Soc.*, vol. 132, no. 39, pp. 13612–13614, Oct. 2010.
- [21] D. Tench, "Electrodeposition of Conducting Transition Metal Oxide/Hydroxide Films from Aqueous Solution," *J. Electrochem. Soc.*, vol. 130, no. 4, p. 869, 1983.
- [22] S. Mukhopadhyay, S. K. Mandal, S. Bhaduri, and W. H. Armstrong, "Manganese clusters with relevance to photosystem II," *Chem. Rev.*, vol. 104, no. 9, pp. 3981–4026, Sep. 2004.
- [23] M. Huynh, C. Shi, S. J. L. Billinge, and D. G. Nocera, "Nature of Activated Manganese Oxide for Oxygen Evolution," *J. Am. Chem. Soc.*, vol. 137, no. 47, pp. 14887–14904, Dec. 2015.
- [24] B. J. Deibert *et al.*, "Surface and Structural Investigation of a MnO<sub>x</sub> Birnessite-Type Water Oxidation Catalyst Formed under Photocatalytic Conditions," *Chemistry - A European Journal*, vol. 21, no. 40, pp. 14218–14228, 2015.
- [25] E. S. Ilton, J. E. Post, P. J. Heaney, F. T. Ling, and S. N. Kerisit, "XPS determination of Mn oxidation states in Mn (hydr)oxides," *Appl. Surf. Sci.*, vol. 366, pp. 475–485,

2016.

- [26] A. Indra *et al.*, “Active mixed-valent MnO(x) water oxidation catalysts through partial oxidation (corrosion) of nanostructured MnO particles,” *Angew. Chem. Int. Ed Engl.*, vol. 52, no. 50, pp. 13206–13210, Dec. 2013.
- [27] F. Jiao and H. Frei, “Nanostructured cobalt and manganese oxide clusters as efficient water oxidation catalysts,” *Energy Environ. Sci.*, vol. 3, no. 8, p. 1018, 2010.
- [28] I. Zaharieva, M. Mahdi Najafpour, M. Wiechen, M. Haumann, P. Kurz, and H. Dau, “Synthetic manganese–calcium oxides mimic the water-oxidizing complex of photosynthesis functionally and structurally,” *Energy Environ. Sci.*, vol. 4, no. 7, p. 2400, 2011.
- [29] A. Iyer *et al.*, “Water Oxidation Catalysis using Amorphous Manganese Oxides, Octahedral Molecular Sieves (OMS-2), and Octahedral Layered (OL-1) Manganese Oxide Structures,” *J. Phys. Chem. C*, vol. 116, no. 10, pp. 6474–6483, 2012.
- [30] I. Zaharieva *et al.*, “Electrosynthesis, functional, and structural characterization of a water-oxidizing manganese oxide,” *Energy Environ. Sci.*, vol. 5, no. 5, p. 7081, 2012.
- [31] Y.-K. Hsu, Y.-C. Chen, Y.-G. Lin, L.-C. Chen, and K.-H. Chen, “Birnessite-type manganese oxides nanosheets with hole acceptor assisted photoelectrochemical activity in response to visible light,” *J. Mater. Chem.*, vol. 22, no. 6, pp. 2733–2739, 2012.
- [32] F. Zhou, A. Izgorodin, R. K. Hocking, V. Armel, L. Spiccia, and D. R. Macfarlane, “Improvement of catalytic water oxidation on MnO<sub>x</sub> films by heat treatment,” *ChemSusChem*, vol. 6, no. 4, pp. 643–651, Apr. 2013.
- [33] W. T. Osowiecki, S. W. Sheehan, K. J. Young, A. C. Durrell, B. Q. Mercado, and G. W. Brudvig, “Surfactant-mediated electrodeposition of a water-oxidizing manganese oxide,” *Dalton Trans.*, vol. 44, no. 38, pp. 16873–16881, Oct. 2015.
- [34] Y. Cheng and S. P. Jiang, “Advances in electrocatalysts for oxygen evolution reaction of water electrolysis—from metal oxides to carbon nanotubes,” *Progress in Natural Science: Materials International*, vol. 25, no. 6, pp. 545–553, 2015.
- [35] E. A. Johnson and J. E. Post, “Water in the interlayer region of birnessite: Importance in cation exchange and structural stability,” *Am. Mineral.*, vol. 91, no. 4, pp. 609–618, 2006.
- [36] H. Matsui, J. Ju, T. Odaira, and N. Toyota, “Two-Dimensionally Confined Water in between MnO<sub>2</sub> Layers of Na-Birnessite,” *J. Phys. Soc. Jpn.*, vol. 78, no. 7, p. 074801, 2009.
- [37] R. Jothiramalingam, B. Viswanathan, and T. K. Varadarajan, “Synthesis and

- structural characterization of copper incorporated manganese oxide OMS-2 materials synthesized via potassium birnessite,” *Mater. Chem. Phys.*, vol. 100, no. 2–3, pp. 257–261, 2006.
- [38] A. Ramírez, P. Hillebrand, D. Stellmach, M. M. May, P. Bogdanoff, and S. Fiechter, “Evaluation of MnO<sub>x</sub>, Mn<sub>2</sub>O<sub>3</sub>, and Mn<sub>3</sub>O<sub>4</sub> Electrodeposited Films for the Oxygen Evolution Reaction of Water,” *J. Phys. Chem. C*, vol. 118, no. 26, pp. 14073–14081, 2014.
- [39] J.-K. Chang, Y.-L. Chen, and W.-T. Tsai, “Effect of heat treatment on material characteristics and pseudo-capacitive properties of manganese oxide prepared by anodic deposition,” *J. Power Sources*, vol. 135, no. 1–2, pp. 344–353, 2004.
- [40] M. Augustin *et al.*, “Manganese oxide phases and morphologies: A study on calcination temperature and atmospheric dependence,” *Beilstein J. Nanotechnol.*, vol. 6, pp. 47–59, Jan. 2015.
- [41] M. S. Burke, L. J. Enman, A. S. Batchellor, S. Zou, and S. W. Boettcher, “Oxygen Evolution Reaction Electrocatalysis on Transition Metal Oxides and (Oxy)hydroxides: Activity Trends and Design Principles,” *Chem. Mater.*, vol. 27, no. 22, pp. 7549–7558, 2015.
- [42] K. Fominykh *et al.*, “Iron-doped nickel oxide nanocrystals as highly efficient electrocatalysts for alkaline water splitting,” *ACS Nano*, vol. 9, no. 5, pp. 5180–5188, May 2015.
- [43] D. H. Youn, Y. B. Park, J. Y. Kim, G. Magesh, Y. J. Jang, and J. S. Lee, “One-pot synthesis of NiFe layered double hydroxide/reduced graphene oxide composite as an efficient electrocatalyst for electrochemical and photoelectrochemical water oxidation,” *J. Power Sources*, vol. 294, pp. 437–443, 2015.
- [44] M. W. Louie and A. T. Bell, “An investigation of thin-film Ni–Fe oxide catalysts for the electrochemical evolution of oxygen,” *J. Am. Chem. Soc.*, vol. 135, no. 33, pp. 12329–12337, Aug. 2013.
- [45] Y. Ullal and A. Chitharanjan Hegde, “Electrodeposition and electro-catalytic study of nanocrystalline Ni–Fe alloy,” *Int. J. Hydrogen Energy*, vol. 39, no. 20, pp. 10485–10492, 2014.
- [46] “Electrolytic Cells,” *Chemistry LibreTexts*, 02-Oct-2013. [Online]. Available: [https://chem.libretexts.org/Core/Analytical\\_Chemistry/Electrochemistry/Electrolytic\\_Cells](https://chem.libretexts.org/Core/Analytical_Chemistry/Electrochemistry/Electrolytic_Cells). [Accessed: 03-Mar-2018].
- [47] P. T. Kissinger and W. R. Heineman, “Cyclic voltammetry,” *J. Chem. Educ.*, vol. 60, no. 9, p. 702, 1983.
- [48] J. Wang, *Analytical Electrochemistry*. 2006.

- [49] J. O. Bockris and A. K. N. Reddy, *Volume 1: Modern Electrochemistry: Ionics*. Springer Science & Business Media, 1998.
- [50] J. Tafel, “Über die Polarisation bei kathodischer Wasserstoffentwicklung,” *Zeitschrift für Physikalische Chemie*, vol. 50U, no. 1, 1905.
- [51] N.-T. Suen, S.-F. Hung, Q. Quan, N. Zhang, Y.-J. Xu, and H. M. Chen, “Electrocatalysis for the oxygen evolution reaction: recent development and future perspectives,” *Chem. Soc. Rev.*, vol. 46, no. 2, pp. 337–365, Jan. 2017.
- [52] R. Guidelli *et al.*, “Definition of the transfer coefficient in electrochemistry (IUPAC Recommendations 2014),” *J. Macromol. Sci. Part A Pure Appl. Chem.*, vol. 86, no. 2, 2014.
- [53] S. Giménez and J. Bisquert, *Photoelectrochemical Solar Fuel Production: From Basic Principles to Advanced Devices*. Springer, 2016.
- [54] V. S. Bagotsky, *Fundamentals of Electrochemistry*. 2005.
- [55] M. A. White, *Physical Properties of Materials, Second Edition*. CRC Press, 2011.
- [56] “D. Potentiostats,” *Chemistry LibreTexts*, 22-Sep-2016. [Online]. Available: [https://chem.libretexts.org/Core/Analytical\\_Chemistry/Analytical\\_Sciences\\_Digital\\_Library/JASDL/Courseware/Analytical\\_Electrochemistry%3A\\_The\\_Basic\\_Concepts/05\\_Experimental\\_Hardware/D.\\_Potentiostats](https://chem.libretexts.org/Core/Analytical_Chemistry/Analytical_Sciences_Digital_Library/JASDL/Courseware/Analytical_Electrochemistry%3A_The_Basic_Concepts/05_Experimental_Hardware/D._Potentiostats). [Accessed: 04-Mar-2018].
- [57] *Surface Analysis— The Principal Techniques*. 2009.
- [58] M. P. Seah, I. S. Gilmore, and S. J. Spencer, “Quantitative XPS,” *J. Electron Spectrosc. Relat. Phenom.*, vol. 120, no. 1–3, pp. 93–111, 2001.
- [59] “NPTEL :: Biotechnology - Bioanalytical Techniques and Bioinformatics.” [Online]. Available: <http://nptel.ac.in/courses/102103044/18>. [Accessed: 09-Mar-2018].
- [60] S. D. Škapin, V. Čadež, D. Suvorov, and I. Sondi, “Formation and properties of nanostructured colloidal manganese oxide particles obtained through the thermally controlled transformation of manganese carbonate precursor phase,” *J. Colloid Interface Sci.*, vol. 457, pp. 35–42, 2015.
- [61] “KP Technology Ltd.” [Online]. Available: <http://www.kelvinprobe.info/technique-theory.htm>. [Accessed: 04-Mar-2018].
- [62] “KP Technology Ltd.” [Online]. Available: <http://www.kelvinprobe.info/technique-principles.htm>. [Accessed: 12-Mar-2018].
- [63] M. E. C. Pascuzzi, “Personal communication,” 09-May-2016.
- [64] A. C. Thenuwara *et al.*, “Nickel Confined in the Interlayer Region of Birnessite: an Active Electrocatalyst for Water Oxidation,” *Angew. Chem. Int. Ed Engl.*, vol. 55,

- no. 35, pp. 10381–10385, Aug. 2016.
- [65] G. P. Lopinski, “Personal communication,” 28-Sep-2016.
- [66] P. Hohenberg and W. Kohn, “Inhomogeneous Electron Gas,” *Physical Review*, vol. 136, no. 3B, pp. B864–B871, 1964.
- [67] J. Hafner and G. Kresse, “The Vienna AB-Initio Simulation Program VASP: An Efficient and Versatile Tool for Studying the Structural, Dynamic, and Electronic Properties of Materials,” in *Properties of Complex Inorganic Solids*, 1997, pp. 69–82.
- [68] “mp-19395: MnO<sub>2</sub> (tetragonal, I4/m, 87).” [Online]. Available: <https://materialsproject.org/materials/mp-19395/>. [Accessed: 12-Mar-2018].